

A molecular dynamics investigation of ice nucleation induced by electric fields

by

Jingyi Yan

B.Sc., Shanghai Jiao Tong University, 2008
Ph.D., The University of British Columbia, 2014

A THESIS SUBMITTED IN PARTIAL FULFILLMENT OF
THE REQUIREMENTS FOR THE DEGREE OF
DOCTOR OF PHILOSOPHY

in

The Faculty of Graduate and Postdoctoral Studies
(Chemistry)

THE UNIVERSITY OF BRITISH COLUMBIA
(Vancouver)

July 2014

© Jingyi Yan 2014

Abstract

This thesis aims to understand the influence of electric fields on ice nucleation. Molecular dynamics simulations are employed to investigate heterogeneous ice nucleation induced by electric fields, and why external electric fields promote freezing in liquid water models.

The first project considers heterogeneous ice nucleation in systems, where water molecules experience an electric field in a narrow region over an entire surface. The specific focus is ice nucleation and growth processes. Different water models are considered, and the influences of temperature and field parameters are examined. We find no qualitative difference between the two water models. By analyzing structure, we show that a ferroelectric cubic ice layer freezes inside the field region, and unpolarized ice grows beyond the field region, at temperatures not far below the melting point.

We explore ice nucleation by electric field bands, which act only over a portion of a surface. Field bands of different geometry nucleate ice, provided that the band is sufficiently large. Analysis of different systems reveals that ice strongly prefers to grow at the (111) crystal plane of cubic ice, and that ice nucleated by field bands usually grows as a mixture of cubic and hexagonal ice. Our results suggest that local electric fields could play a major role in heterogeneous ice nucleation, particularly for rough particles with many surface structural variations, that serve as ice nuclei in the environment.

We also investigate the electrofreezing of water subject to a uniform field. The aim is to obtain an understanding of why electric fields facilitate ice nucleation. It is shown that the melting point of water increases significantly when water is polarized by a field. The increased melting point is mainly due to the favourable interaction of near perfectly polarized cubic ice with

Abstract

the applied field. Relevant to the mechanism of heterogeneous ice nucleation by local surface fields, our results suggest that local fields effectively increase the degree of supercooling of locally polarized liquid. This decreases the size of the critical nucleus in the region influenced by the field, facilitating ice nucleation.

Preface

Chapter 3 and Chapter 4 are co-authored, peer-reviewed journal articles. Chapter 5 has been submitted to a peer-reviewed journal as a co-authored journal article. The details of my contributions to each chapter mentioned above are listed below.

A version of Chapter 3 has been published by J. Y. Yan and G. N. Patey, Heterogeneous Ice Nucleation Induced by Electric Fields, *J. Phys. Chem. Lett.* **2(20)**, 2555, (2011); Molecular Dynamics Simulations of Ice Nucleation by Electric Fields, *J. Phys. Chem. A.* **116(26)**, 7057, (2012). My contributions are as follows:

- Designed the research project with my supervisor.
- Formulated the research questions and wrote the computation programs.
- Performed all of the simulations.
- Performed all of the data analysis.
- Prepared all of the figures in the publications.
- Wrote the first draft of the publications.
- Writing of the text for the publications was shared with my supervisor.

A version of Chapter 4 has been published by J. Y. Yan and G. N. Patey, Ice nucleation by electric surface fields of varying range and geometry, *J. Chem. Phys.* **139**, 144501, (2013). My contributions are as follows:

- Designed the research project with my supervisor.

- Performed all of the simulations.
- Performed all of the data analysis.
- Prepared all of the figures in the publication.
- Wrote the first draft of the publication.
- Writing of the text for the publication was shared with my supervisor.

A version of Chapter 5 has been submitted by J. Y. Yan, S. D. Overduin, and G. N. Patey, Understanding electrofreezing in water simulations, *J. Chem. Phys.* (submitted, May, 2014). My contributions are as follows:

- Designed the research project with my supervisor.
- Performed all the simulations with Dr. S. D. Overduin.
- Performed all of the data analysis with Dr. S. D. Overduin.
- Prepared the tables and figures in the publication.
- Wrote the first draft of the publication.
- Shared writing of the text for the publication with Dr. S. D. Overduin and my supervisor.
- Additional contributions from co-authors:
 - Dr. S. D. Overduin did the data analysis for the tetrahedral order parameter distributions, structure factors, and partial radial distribution functions.
 - Dr. S. D. Overduin performed the simulations in Table 5.3, and contributed to the discussion on the influence of electric field.

Table of Contents

Abstract	ii
Preface	iv
Table of Contents	vi
List of Tables	ix
List of Figures	xii
Acknowledgements	xvii
1 Introduction	1
1.1 Nucleation in the Atmosphere and in Biological Systems	1
1.2 Nucleation Theory	3
1.3 Field Induced Ice Nucleation	6
1.4 Thesis Motivation and Objectives	10
1.5 Thesis Overview	15
2 Models and Simulation Methods	16
2.1 Molecular Models	16
2.2 Interaction Potentials	20
2.3 Models of Electric Fields	24
2.4 System Evolution	29
2.4.1 The Gear Predictor-Corrector Method for Translational Motion	29
2.4.2 Quaternions and Rotational Motion	32

Table of Contents

2.4.3	Simulation Constraints	35
2.5	Comparison with Open Source Packages	37
2.6	Data Analysis	39
2.6.1	Radial Distribution Function	39
2.6.2	The CHILL Ice Detector	40
2.6.3	Orientalional Order Parameter	41
3	Heterogeneous Ice Nucleation Induced by Surface Electric Fields	44
3.1	Introduction	44
3.2	The Model and Simulation Method	46
3.3	Results and Discussion	49
3.3.1	Ice Nucleation Induced by a Surface field	49
3.3.2	Ice Nucleation in Systems of Varying Size and Dimension	54
3.3.3	Influence of Temperature	61
3.3.4	Influence of Field Strength and Extent	66
3.4	Summary and Conclusions	70
4	Ice Nucleation by Electric Surface Fields of Varying Range and Geometry	74
4.1	Introduction	74
4.2	Models and Methods	78
4.3	Results and Discussion	81
4.3.1	Full Surface Field	81
4.3.2	Partial Surface Fields	85
4.4	Summary and Conclusions	92
5	Understanding Electrofreezing in Water Simulations	94
5.1	Introduction	94
5.2	Simulation and Analysis Method	96
5.3	Results	100
5.3.1	Melting Temperature	100
5.3.2	Ice Clusters and Nucleation	104

Table of Contents

5.3.3	Thermodynamic Functions	111
5.3.4	Structural Changes with Field	116
5.4	Summary and Conclusions	119
6	Conclusions and Perspective	123
6.1	Simulation Results on Ice Nucleation and Electrofreezing . .	123
6.2	Future Work	126
	Bibliography	128

List of Tables

2.1	Water model and surface parameters used in the simulations. Note that ε and σ are the energy and distance parameters for the interaction calculation, r_1 is the oxygen-hydrogen bond distance, r_2 is the distance between the oxygen and the negative charges (OM or OL), q is the charge on each site, and θ and ϕ are angles associated with different sites in water molecules. The subscripts HOH, MOH and LOL indicate the angles between two hydrogen atoms, between the negative charge M and the hydrogen atom, and between the two lone pair charge sites. Note that L is short for lone pair (LP). . . .	18
3.1	The systems considered in tests of possible finite size effects. In the third column, the first and second pairs of integers give the number of trials and the run times for the six-site and TIP4P/Ice models, respectively. The number of trials for which ice nucleation was observed in the given simulation time is given in brackets.	55
3.2	Temperatures considered for the six-site and TIP4P/Ice models. Yes and No indicate whether ice nucleation and growth was observed or not at the particular temperature.	63
3.3	The dependence of ice nucleation on the parameters E_{\max} and c in Equation (3.1). The simulations were at 270 K for the six-site model, and at 260 K for TIP4P/Ice. Yes and No indicate whether ice nucleation and growth was observed or not for the given field parameters.	67

List of Tables

- 4.1 Summary of simulations carried out with partial surface fields. For simulations 1-10, L_x , L_y , and L_z are 2.67, 10, and 5 nm, respectively, for simulation 11, 2.68, 10, and 7 nm, respectively. In all simulations the density is ~ 0.96 g/cm³. The numbers given in brackets in column one are the (y, z) dimensions (in nm) of the field bands (Fig. 2.3). The times given in this table are the lengths of the simulations. For rectangles these are the length and width, for triangles the base and height, and for semicircles the radius. The numbers of cubic, hexagonal, and liquid water molecules in the configuration at the final timestep are given in the last three columns. . . . 86
- 5.1 Melting temperature estimates for different fields obtained from simulations with 8000 molecules. Estimates of ΔS_{fus} are obtained from *NPT* simulations with 1000 molecules. The last two columns are the average polarization for liquid and solid systems. L and S stand for liquid and solid respectively. 101
- 5.2 Summary of ice-like molecules and ice clusters observed in different systems; configurations from each simulation were saved at 10 ps intervals. For some systems, multiple independent simulations were performed as indicated. At 270 K, freezing occurred within 40 ns for each of the ten simulations performed with a field of 1 V/nm; the tabulated data were taken from pre-freezing configurations. For all systems, the largest cluster reported is the largest ice cluster (see text for definition of cluster) observed that subsequently melted. . . . 105

List of Tables

5.3	Summary of ice-like molecules in starting configurations used to estimate the critical ice nucleus size. The starting configurations were taken from simulations performed with 32000 water molecules interacting with a field of 1 V/nm at 270 K, where freezing eventually occurred. The number of molecules meeting the condition for interfacial ice (N_I), as identified by the CHILL algorithm, are recorded in the table, but only cubic (N_C) and hexagonal (N_H) ice-like molecules were included in determining the size of ice clusters. These four starting configurations were used in simulations to estimate the highest temperature at which the initial ice cluster nucleates ice, both with and without a field.	110
5.4	Densities in polarized and unpolarized water from simulations with 8000 molecules at 1 bar.	118

List of Figures

2.1	Schematics of the TIP4P/Ice (left) and six-site (right) water models. The water oxygen atoms (O) are red and hydrogen atoms (H) are black, the sites of negative charge on oxygen (M) are cyan, and the lone pair charge sites (LP) are yellow.	17
2.2	Schematic of the confined water systems. The surfaces are denoted as two vertical lines, and the water molecules are placed between them.	19
2.3	A sketch of the simulation cell showing the electric field geometries considered. The surfaces are placed at both the left and right side of the box, and the field is directed along the y axis (perpendicular to the page).	26
2.4	A plot showing the trend of the electric field magnitude, where $a = 10 \text{ \AA}$, $c = 10 \text{ \AA}$, and $f(y, z) = z$ in Equation (2.15). The surfaces are placed at $z = 0 \text{ \AA}$ and $z = 40 \text{ \AA}$	27
3.1	Configurational snapshots of one particular simulation with 1200 water molecules. The field (directed upwards along the y axis) was applied at $t = 0$ (upper panel), the middle ($t = 2.4$ ns) and bottom ($t = 4$ ns) panels show the nucleation and growth of ice. The oxygen atoms of the water molecules that experience the field ($z \lesssim 10 \text{ \AA}$) are green, those outside the field region are red, and all hydrogen atoms are black.	51
3.2	The dipole order parameter profile along the z axis for the field-nucleated, frozen sample. The red, green, and blue lines are the x , y , and z components, respectively. Note that the y component shows field-induced polarization for $z \lesssim 10 \text{ \AA}$	52

List of Figures

3.3	Oxygen-oxygen and hydrogen-hydrogen radial distribution functions. The black, red, and dark blue lines are the zero field, constant field, and field-nucleated results, respectively. The light blue lines represent ferroelectric bulk cubic ice frozen under a constant field.	54
3.4	Configurational snapshots after 18 ns of two selected trial runs that show ice nucleation and growth. In one system (top), $L_z = 60 \text{ \AA}$ (648 particles) and in the other (bottom) $L_z = 80 \text{ \AA}$ (900 particles). The oxygen atoms of water molecules that experience the field are blue, those outside the field region are red, and all hydrogen atoms are black. The top and bottom projections can be recognized as the (101) and (001) crystallographic planes of cubic ice, respectively.	57
3.5	The water-water contribution to the configurational energy for the six-site model at 270 K. Results for eight trial runs of the 432 particle system are shown. The field was applied at 2 ns. Note that all eight trials show clear nucleation and freezing, as signalled by a rapid drop in the water-water interaction energy.	58
3.6	Oxygen-oxygen radial distribution functions for the six-site (top panel) and TIP4P/Ice (bottom panel) models. Curves for different system sizes are shown, and compared with the bulk cubic ice result.	60
3.7	Density (top panel) and dipole order parameter (bottom panel) profiles for two trial runs of the six-site model with 432 particles.	61
3.8	Configurational snapshots of the two trial runs for which density profiles are shown in Fig. 3.7. Both snapshots are of the configuration at the 32nd nanosecond, and both are from the same perspective. The oxygen atoms of the water molecules that experience the field are blue, those outside the field region are red, and all hydrogen atoms are black. The ice crystals clearly have different orientations in the simulation cell.	62

List of Figures

3.9	Oxygen-oxygen radial distribution functions and mean square displacement (MSD) curves for the six-site model at different temperatures.	64
3.10	Dipole order parameter profiles and oxygen-oxygen radial distribution functions at different values of E_{\max} and c for both the six-site and TIP4P/Ice models. The values of $E_{\max} \times 10^{-9}$ V/m and of c are indicated in the figure.	68
4.1	Configurational snapshots showing ice nucleation and growth for a 2400 molecule system with a full surface field. The snapshots show the (110) plane of cubic ice at 20 ns (stage 1), 50 ns (stage 2), 60 ns (stage 3), and 70 ns (stage 4). The water oxygen atoms in the field region are dark blue, those associated with cubic ice or liquid are red, and those in hexagonal ice layers are light blue. All hydrogen atoms are black. The rectangles outline the central cell. The dashed green lines shown in stage 1 indicate growth at (111) planes of cubic ice.	83
4.2	Configurational snapshots showing ice nucleation and growth for a rectangular field band (simulation 2 of Table 4.1). From left to right the snapshots correspond to 15, and 90 ns. The atoms are coloured as in Fig. 4.1. The dashed green lines in the snapshot at 15 ns indicate ice growth at (111) faces of cubic ice. Note that the hexagonal ice layers meet the surface outside the field region.	88
4.3	Configurational snapshot (at 85 ns) showing ice nucleated by a rectangular field band in a larger system (simulation 11 of Table 4.1). The atoms are coloured as in Fig. 4.1. Note that in the larger system hexagonal ice layers can form parallel to the surface.	89

List of Figures

4.4	Configurational snapshots (at 90 ns) of ice nucleated with a semicircular field band (simulation 10 of Table 4.1). The (001) (left panel) and (110) (right panel) planes of cubic ice are shown. The atoms are coloured as in Fig. 4.1. Note that the hexagonal ice layers meet the surface outside the field region.	91
5.1	Example starting configuration containing ~ 4000 ice-like molecules. The oxygen atoms of cubic ice-like molecules are shown in dark blue, hexagonal ice-like molecules in light blue, and liquid molecules in red. All hydrogen atoms are white. . . .	102
5.2	Average number of clusters (per configuration) of a given size observed in <i>NPT</i> (1 bar) simulations with 8000 molecules. Results are shown for: 0 V/nm, 260 K (red); 1 V/nm, 280 K (blue); 1 V/nm, 290K (black). Standard errors estimated from ten independent simulations of 40 ns (260 K) or 50 ns (280 and 290 K) are also shown.	106
5.3	Oxygen-oxygen radial distribution functions for ice-like molecules obtained from simulations ($N = 8000$, $P = 1$ bar) for three systems, as indicated in the legend.	107
5.4	Example starting configuration with an ice “nucleus” of ~ 500 molecules. Only cubic (blue) and hexagonal (red) ice-like molecules are shown.	108
5.5	Changes in thermodynamic properties (top) and the dipole order parameter (bottom) as functions of field strength. . . .	112
5.6	Entropy change as a function of polarization ($\langle m_x \rangle$) at 300 K. The red circles are from Equation (5.13), and the blue triangles denote the simulation results. The lines are to guide the eye.	115
5.7	Comparison of tetrahedral order parameter distributions at constant pressure for different temperatures and external fields, as indicated in the legend.	116

List of Figures

5.8	Total (bottom) and partial (as labeled) pair correlation functions at the temperatures and fields indicated in the legend. Multiplication by r^2 magnifies the structural features.	117
5.9	Structure factors for the temperatures and electric fields indicated in the legend.	120

Acknowledgements

Foremost, I would like to express my sincere gratitude to my supervisor, Prof. Gren Patey, for all his patient help, enthusiastic discussion, and kind encouragement in my research throughout these years. I also benefit much more from his positive and energetic attitude in daily life. Working and talking with him is very interesting and comfortable, and our conversation is always valuable when I encountered difficulties. I would not have accomplished my thesis without his guidance, and could not imagine a better supervisor for my Ph.D study. I would like to thank all my colleagues for their help and advice. When I started my new life and research in Canada, I received lots of support and help from our group members. I always appreciate the kindness and warm heart of Dr. Heidrun Spohr, Erin Lindenberg and Dr. Timothe Croteau. I would like to thank Dr. Sarah Overduin and Dr. Debashree Chakraborty for their knowledge and experiences in simulations and thermodynamics. They were great mentors in my courses and research, and also good friends for drinking, hiking, and doing yoga together. Last but not least, I would like to thank my committee members and Westgrid facilitators for their help.

Finally, I would like to thank all my dear friends for sharing so many precious memories with me. I would like to thank my husband Dr. Zheng Yang and my parents. I owe a great debt to my family. I would never be here without their love.

Chapter 1

Introduction

Water is one of the most important substances on Earth. It is the vital solvent in living cells, the most widely used medium in industry, and an integral part of the hydrologic cycle. Also, water exists as three basic phases on Earth: solid, liquid, and gas, and there are more than 10 phases of ice. How liquid water turns into ice is crucial in climate change as well as industrial applications. Why and how ice forms, and what conditions promote ice nucleation, are significant questions that remain poorly understood. The objective of this thesis is to understand one possible microscopic nucleation mechanism, and the associated thermodynamic properties of the nucleation process. As an ideal tool for investigating nucleation, Molecular Dynamics (MD) simulations can provide a direct microscopic picture of ice nucleation and growth.

1.1 Nucleation in the Atmosphere and in Biological Systems

In the hydrologic cycle, water vapour in the air rises mostly by convection into the atmosphere, where cooler temperatures cause it to condense into clouds. Composed of liquid droplets or frozen crystals with water and various

1.1. Nucleation in the Atmosphere and in Biological Systems

chemicals, clouds have a major effect both short term on the weather, and long term on the absorption and scattering of solar radiation [1–7].

There are two ways for ice to nucleate. Homogeneous ice nucleation proceeds from liquid water in the absence of a foreign substance. In contrast, heterogeneous nucleation occurs when water is in contact with certain foreign substances, which act as a so-called ice nuclei (IN) [7, 8]. Both nucleation mechanisms take place in clouds, where ice formation can strongly impact the atmospheric conditions and play a major role in precipitation [9].

Heterogeneous ice nucleation happens readily in the atmosphere, triggered by aerosol particles [3, 10]. The formation of ice clouds is thought to be influenced by agents of ice nucleation present in atmospheric aerosols [11]. Atmospheric aerosols are a complex mixture of solid particles and liquid drops, with mineral dust particles being among the most important ice nuclei in the atmosphere [12–14]. Large quantities of mineral dust particles are aerosolized into the atmosphere from various sources, most from arid regions in Africa, the Middle East and Asia [15]. Mica and quartz are major contributors to mineral dust, while kaolinite, chlorite, and other clay minerals are found in lower concentrations [16]. These particles provide sites for surface reactions and condensed-phase chemistry to take place in the atmosphere, and act as cloud condensation nuclei [6, 13, 17–19]. Kaolinite particles are known to be effective ice nuclei and facilitate ice nucleation and cloud formation processes [6, 20, 21]. This could lead to more precipitation and less solar radiation reaching the surface of Earth. Understanding the interaction of water with mineral dust particles is important for research on the mechanism of ice nucleation, and indirectly on climate change.

Apart from its importance for atmospheric phenomena, the relevance of ice nucleation is widespread. In astrophysics, abundant subsurface ice is found on many planets in the Solar System [22, 23]. Moreover, ice nucleation plays a key role in ecosystems [24] and biological systems [25, 26]. Intracellular ice is lethal to cells and in cryobiology it is crucial to control ice formation [27]. Certain epiphytic bacteria capable of living on leaf surfaces are able to catalyse ice formation at temperatures close to 0 °C, which results in frost injury in plants [28, 29]. Ice accumulation on surfaces is also a key factor contributing to energy efficiency in aircraft de-icing, powerline maintenance, and building construction [30, 31]. The applications of ice nucleation extend from physiology [32, 33] to food science [34, 35], and from snow production [36] to nano-techniques [37].

1.2 Nucleation Theory

Classical Nucleation Theory (CNT) [38–41] is a good starting point from which to consider the ice nucleation process. CNT uses macroscopic thermodynamic quantities to describe the emergence of a new phase. It can be used to describe both homogeneous and heterogeneous nucleation processes. Homogeneous nucleation refers to the creation of a new phase in the absence of any foreign substance, while heterogeneous nucleation is facilitated by the action of foreign agents or surfaces.

Near the equilibrium transition point, the original phase remains metastable, and the formation of a new phase depends on the height of the Gibbs free energy barrier. At temperatures below 0 °C, supercooled liquid water is

1.2. Nucleation Theory

metastable with respect to natural crystalline ice, and can form new solid clusters. The assumption is made that the solid cluster is spherical and has a radius r , thus the free energy difference between the two phases can be written as [1–3, 42]

$$\Delta G_p = \frac{4\pi r^3}{3v}(\mu_2 - \mu_1), \quad (1.1)$$

where the subscript p indicates the free energy change due to the phase change, v is the molecular volume of ice, and μ_i is the chemical potential of phase i . This term is always negative and favourable, but creating an interface between the two phases is associated with an increase in free energy

$$\Delta G_s = 4\pi r^2 \sigma, \quad (1.2)$$

where the subscript s indicates the free energy change due to surface tension, σ is the surface tension between the new and parent phases. The nucleation process is controlled by the overall Gibbs free energy change, which is the sum of the volume free energy change of Equation (1.1) plus the surface free energy of Equation (1.2)

$$\Delta G_{homo} = \frac{4\pi r^3}{3v}(\mu_2 - \mu_1) + 4\pi r^2 \sigma, \quad (1.3)$$

where the subscript *homo* indicates the free energy change for a homogeneous nucleation process.

As the cluster size becomes larger, the overall free energy change will increase and reach a maximum, which is called the free energy barrier to nucleation. At larger sizes, the free energy will drop and lead to ice growth.

1.2. Nucleation Theory

The position of the free energy maximum determines the critical radius r^* , which can be obtained by taking a derivative [1, 42] of Equation (1.3)

$$\left. \frac{\partial \Delta G_{hom}}{\partial r} \right|_{r=r^*} = 0. \quad (1.4)$$

The critical radius r^* and the critical free energy ΔG_{hom}^* are

$$r^* = \frac{-2\sigma v}{(\mu_2 - \mu_1)}, \quad (1.5)$$

$$\Delta G_{hom}^* = \frac{16\pi\sigma^3 v^2}{3(\mu_2 - \mu_1)}. \quad (1.6)$$

When new born clusters are smaller than the critical size r^* , a molecule leaving the clusters is preferable to a molecule being added. Therefore, ice nucleation will not be favoured and clusters may decompose back to liquid. However, for clusters larger than r^* , growth will be spontaneous by condensation of further molecules, and the free energy decreases continuously.

Usually, the critical conditions required for homogeneous nucleation can be quite difficult to achieve in real systems. However, the concepts and principles of homogeneous nucleation are simple and helpful for analysing other types of nucleation. The equation of critical free energy [Equation (1.6)] highlights the strong dependence on interfacial tension, and it is easy to speculate that a suitable foreign substances in contact with liquid water can reduce the free energy barrier and catalyze ice nucleation.

Let us assume that heterogeneous nucleation is taking place on an insoluble foreign flat surface, and the newly formed ice cluster is hemispherical on the planar surface. In this case, the classical expression for the critical

1.3. Field Induced Ice Nucleation

free energy ΔG_{het}^* of cluster formation on the surface will be [1, 2]

$$\Delta G_{het}^* = \Delta G_{homo}^* f(\theta), \quad (1.7)$$

where θ is the contact angle between the spherical cluster and the flat substrate, and $f(\theta)$ is a geometric factor with values between 0 and 1. By the presence of a surface, the height of the free energy barrier relative to homogeneous nucleation is reduced by the factor $f(\theta)$. Although $f(\theta)$ can be established empirically, its physical significance is unclear since the ice nucleus may not adopt a hemispherical form [1, 3]. In some cases $f(\theta)$ may correspond to adaptations in a single molecular layer at the interface between the surface and the new cluster, whereas in other cases the reduction of the free energy barrier by a substrate may be due to density fluctuations caused by the impact of the substrate. Since pure bulk water is rare in daily life, and heterogeneous nucleation is effective at warmer temperatures [43], the formation of water droplets and ice in nature is usually by heterogeneous nucleation.

Classical nucleation theory assumes a spherical nucleus, and oversimplifies the properties of clusters and surfaces in ice nucleation, therefore one must be aware of its limitations [42].

1.3 Field Induced Ice Nucleation

What promotes ice nucleation has been an interesting topic for researchers for years, and both experimental and theoretical methods are employed to

1.3. Field Induced Ice Nucleation

reveal the nature of the ice nucleation process. Although scientists have noticed connections between electric fields and ice formation, electrofreezing of bulk water has not been firmly established experimentally [44, 45], but electrically induced or assisted freezing in particular environments has been reported. Bulk water undergoes dielectric breakdown under uniform fields at magnitudes of $6.5 - 7.0 \times 10^7$ V/m [46]. As pointed out in Ref. [44], the electric fields achievable on macroscopic length scales are orders of magnitude smaller than the field strength ($\sim 10^9$ V/m) required to electrofreeze model water in computer simulations [47]. For computational simulations, the high magnitude of the field needed to nucleate ice is perhaps due to the time limitation of simulations, and a lower field might work on much longer time scales. However, fields of comparable strength to theoretical prediction ($\sim 10^9$ V/m) do exist on microscopic length scales, leaving open the possibility of field-induced ice nucleation.

There have been a number of experimental reports of ice nucleation in the presence of strong electric fields. The results are in general positive concerning the influence of field on ice nucleation, but remain conflicting. In the 1960s, it was reported that highly charged silver iodide particles prohibited ice nucleation on the surface [48]. Later Dawson and Cardell [49] observed that an electric field did not increase the freezing possibility of water at temperatures between -8° and -15°C . Doolittle and Vali [50] applied an electric field of up to 6×10^5 V/m over sets of super-cooled drops supported on a flat solid surface, and found that there was no significant difference in the heterogeneous nucleation rate due to an electric field. On the other hand, Gabarashvili and Gliki [51] found that

1.3. Field Induced Ice Nucleation

supercooled water drops containing impurities with charged surfaces were nucleated to ice at significantly warmer temperatures when the particles carried a net negative charge than when they were neutral or carried a net positive charge. It was also found by Abbas and Latham [52] that the probability of supercooled drops to freeze was greater if the surface of the drop was disrupted by electrical forces to produce a filament of liquid from the localized area of rupture. Later, Pruppacher [53] found that the freezing temperature of supercooled water was raised considerably when in contact with predominantly negatively charged amorphous sulfur particles, and concluded that electrostatically charged surfaces and local electric fields significantly enhance ice nucleation. The decadal data from 1953 to 1985 on high-energy cosmic ray fluxes indicates that the atmospheric ionization affects ice nucleation in high-level clouds, and the electrofreezing increases the flux of ice crystals [54].

The work of Garvish *et al.* [55] represents a new milestone in the research of ice nucleation under local electric fields. Their authors reported that polar amino acid crystals induced a freezing point higher by 4 - 5 °C than non-polar crystals. These results were interpreted in terms of an electric field mechanism that helps align the water molecules into a proton ordered ice nucleus. Braslavsky and Lipson [56] have reported that a high-voltage electric pulse applied to bulk supercooled water induces ice nucleation. Also, Ehre and coworkers [57] have reported that water freezes differently on positively and negatively charged surfaces. A surface with positive charge promoted ice nucleation, whereas the same surface when negatively charged reduced the freezing temperature. This fact may be related to the orientation of

1.3. Field Induced Ice Nucleation

water molecules with respect to the surface, but the details of how this effect occurs are not yet understood.

The situation for computer simulations of water subjected to electric fields is clearer. Svishchev and Kusalik [47, 58] were the first to show, employing MD simulations, that bulk water freezes readily to form ferroelectric cubic ice Ic when polarized by a strong uniform external field (5×10^9 V/m). The models used were the TIP4P [59] and the SPC/E [60] water models, and the former appeared to be more susceptible to ice nucleation than the latter. Other authors have demonstrated electrofreezing of water confined between plates. Xia and Berkowitz [61] found that when the charge density on Pt surfaces reaches a threshold value, water between these surfaces can freeze into cubic ice. Zangi and Mark [62] reported that water confined between two plates freezes into ice when an electric field is applied parallel to the plates. While these studies suggest that electric fields might be important for ice nucleation, they do not directly address the role of electric field in the electrofreezing process.

Although the field strength necessary to cause freezing in simulations ($\sim 10^9$ Vm⁻¹) [47, 62] is much larger than fields that can be established in macroscopic samples [44], they may exist on smaller length scales. For example, a large electric field can occur along the axis of a polar amino acid crystal [55]. Also, for trench-like structures in model kaolinite, there is an electric field due to surface charge arrangements, which can strongly polarize and order water [63]. Local electric fields can exist in nature, and could possibly be a key factor in ice nucleation. There are, however, important questions to be solved, such as how an ice nucleation process is triggered by

the field, and the initial structure and growth of ice nuclei.

1.4 Thesis Motivation and Objectives

Despite the importance of ice nucleation discussed above, the simple question: What makes a good IN? has proved difficult to answer. One often cited explanation invokes a good crystallographic match between an IN surface and hexagonal ice [7]. Kaolinite is sometimes cited as an example, because kaolinite particles are good IN, and one of its basal planes (the Al-surface) has a potential crystallographic match with hexagonal ice. However, this idea is not supported by recent model calculations [64–67]. A classical model [64] shows that water adsorbed on this surface does not take on an ice-like structure, and coverage beyond a bilayer is not found. Therefore, the crystallographic match argument does not appear to explain kaolinite’s ice nucleating abilities. A similar conclusion was reached for model hexagonal surfaces specifically selected to provide a good match with hexagonal ice Ih [65]. Moreover, an extensive density-functional theory (DFT) study [67] shows that water can wet kaolinite’s basal surface, but multilayer ice growth is not favoured. Hu and Michaelides [66] suggest that the stable overlayer of water on a kaolinite surface is not a consequence of the lattice match with Ih, but rather because the substrate is amphoteric with the ability to form both acceptor and donor hydrogen bonds. A recent MD simulation of ice nucleation near a kaolinite slab [21] shows that on the basal face of kaolinite, growth along the prism face of ice is observed, which contradicts the expectation of the lattice match between ice and the kaolinite surface.

Experiments [68] tend to support the idea that ice nucleation occurs at “active sites”, but the nature of such sites remains an open question.

Studies on kaolinite reveal that the effectiveness of kaolinite for ice nucleation is likely more interesting and complex than a simple lattice match. A quantum mechanical calculation [69] has demonstrated that the kaolinite basal surface is polar. Croteau *et al.* have shown [63] that for particular, trench-like structures in kaolinite, the field due to surface charge arrangements can strongly polarize and order water over distances corresponding to a few molecular layers. An interesting MD study of homogeneous ice nucleation reported by Vrbka and Jungwirth [70] suggested that the electric field associated with water ordering at the surface might partially explain the observation that ice preferred to nucleate in subsurface layers. Note that this work could not be repeated for large systems perhaps due to computational limitations [70]. Inspired by these works, we consider a model of confined water experiencing a surface electric field, which polarizes a thin layer of water molecules near the surface. Note that in this model, the surface field only exists near the surface, and decays to insignificance very rapidly with distance from the surface.

As noted above, it has long been suggested [53] that electric fields could possibly promote freezing, and electrically induced freezing has been confirmed by simulations [47, 62]. However, computational simulation studies have usually focused on electrofreezing, which refers to the process where a uniform electric field is applied to the whole system, and can change thermodynamic properties, such as the melting point itself. Although electrofreezing has been established, there are no previous simulation studies showing

ice nucleation induced by a partial field, where the field only impacts a small part of the system. In this thesis, we demonstrate a different mechanism for heterogeneous ice nucleation when water interacts with a surface field. Our simulation results confirm the speculation that a microscopic surface field can have a positive influence on ice nucleation. We show that water freezes into a thin polarized layer of ice with the help of the surface field, and then grows further beyond the range of the field to form bulk ice.

The overall goal of this thesis is to use computer simulations to investigate the microscopic mechanism of ice nucleation induced by an electric field, and to understand the pattern of ice growth. Firstly, a simple setup is considered, where water molecules located very near a surface (within $\sim 10 \text{ \AA}$) experience an electric field parallel to that surface. The surfaces considered are more or less “neutral”, and do not induce any significant order in the water. In supercooled water, we show how water molecules interact with the surface field, and how ice nucleation can occur. The structure of the system, evolving in time, is analyzed. To ensure that our observations are not an artifact of a particular water model or choice of system parameters, simulations are carried out for a range of system sizes and dimensions. Both the TIP4P/Ice [71] and the six-site [72] water models are considered and the results are compared. We also examine the important influences of temperature and electric field parameters (strength and extent) on ice nucleation and growth. Density and polarization profiles, as well as mean square displacement profiles are analyzed in the process of ice nucleation and growth. This study provides insight into some possible characteristics of good IN.

We further explore ice nucleation by modifying the surface field. We consider surface fields which act only over surface “bands” of different size and geometry. The same two plates are used, and the electric field is applied over a particular geometry near one plate, and decays outside the designated area. By varying the field geometry, we learn more about the mechanism of ice nucleation. In systems with an electric field band, ice freezes inside the field region, and eventually grows further beyond the range of the field. The size of the ice nuclei induced by the electric field is crucial for ice nucleation. We also look into the pattern of ice growth on different crystallographic planes. The water-ice structure is followed in time, and the results show a pattern of layer-by-layer ice growth on the (111) crystal plane. Comparisons of ice growth are made between infinite surface fields and surface field bands. Structures of hexagonal ice are very rare in the former system, which is due to the infinite layer of ice Ic on the surface.

Both hexagonal ice and cubic ice can be constructed by stacking bilayers of water molecules formed of hexagonal rings. But how the bilayers are stacked is different in the two ice phases. In the basal planes of ice Ih, two hexagonal layers are stacked following the ABABAB... sequence, while the (111) planes of ice Ic consist of a stack of the same hexagonal double layers but following the ABCABC... sequence. Then the basal planes of ice Ih and the (111) planes of ice Ic are identical and can be perfectly joined along their hexagonal double layers with very small interfacial energy [73, 74]. Thus it is possible to form either structure when ice is growing on the hexagonal planes.

Ice structures are analyzed using the CHILL algorithm originally devel-

oped by Moore *et al.* [75], and home-written code. As hexagonal and cubic ice are both made of similar layers of water molecules and differ in their stacking pattern, a mixture of ice Ih and Ic is possible when ice grows layer by layer. The question as to whether or not the formation of a subsequent layer on a current (111) crystal layer is random or biased is interesting, and decides the ratio of these two ice structures. The ratio of the two ice structures is reviewed and compared with other work.

In addition to studying the phenomenon of heterogeneous ice nucleation induced by varying fields, we perform simulations on homogeneous ice nucleation in the presence of a uniform electric field. The isothermal isobaric (NPT) ensemble is employed. The goal here is to find the intrinsic reason why electric fields can catalyze ice nucleation, and how water structure is influenced by the field. We investigate the structural and thermodynamic changes that promote freezing when model liquid water interacts with a uniform, external field. It is found that the melting temperature increases significantly when electric fields of $\sim 1 \times 10^9$ V/m are applied; however, liquid water maintains its spatial structure and tetrahedral order, both above and below the melting temperature. Although the melting temperature increases, water interacting with a field remains liquid until it is ~ 40 K below the field-dependent melting temperature. The degree of supercooling determines the size of the critical nucleus, regardless of field. Our results suggest that electric fields produced by surface charges promote freezing by locally “supercooling” water molecules, allowing ice clusters to form and grow.

1.5 Thesis Overview

This thesis is presented in six chapters. The current chapter reviewed background information relevant to ice nucleation applications, classical nucleation theory, as well as the current knowledge of electrofreezing and ice nucleation. Chapter 2 describes in detail the water models used, simulation methods employed, and the methods of analysis. Chapter 3 discusses heterogeneous ice nucleation induced by varying surface fields in confined systems. Chapter 4 deals with ice nucleation induced by field “bands” of different geometries. Chapter 5 considers the mechanism of electrofreezing, and finally, a summary of the results and future directions are presented in Chapter 6.

Chapter 2

Models and Simulation

Methods

In the process of a molecular dynamics (MD) simulation, potential energy and kinetic energy are calculated by knowing the configuration at each time step, and the system propagates by solving the equations of motion. This chapter describes models of the system with water and surfaces, and the methods used in MD simulations. The code that I wrote is compared with open source packages, and the data analysis is discussed.

2.1 Molecular Models

This thesis uses rigid water models to investigate field induced ice nucleation processes. We consider the six-site [72] and the TIP4P/Ice [71] water models. As shown in Fig. 2.1, both water models have an oxygen atom (labeled O) at the center, hydrogen atoms (labeled H) with positive charges on both sides, and also a “dummy” atom (labeled M) with negative charge sitting near the oxygen, on the bisector of the HOH angle. Differing from the TIP4P/Ice model, the six-site model places negative charges on two additional dummy atoms (labeled LP) representing the “lone pairs” electrons of the oxygen

atom. Parameters of both water models are given in Table 2.1.

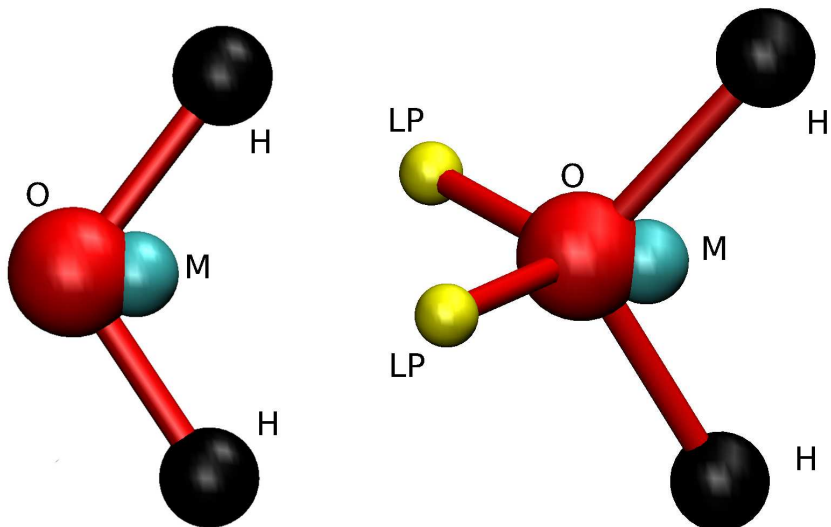


Figure 2.1: Schematics of the TIP4P/Ice (left) and six-site (right) water models. The water oxygen atoms (O) are red and hydrogen atoms (H) are black, the sites of negative charge on oxygen (M) are cyan, and the lone pair charge sites (LP) are yellow.

For confined water systems, stationary surfaces (labeled S) are placed as shown in Fig 2.2. The surfaces are considered as smooth and solid, and interact with the oxygen atom of each molecule through the potential

$$u(z) = \frac{3\sqrt{3}\varepsilon}{2} \left[\left(\frac{\sigma}{z}\right)^9 - \left(\frac{\sigma}{z}\right)^3 \right], \quad (2.1)$$

where z is the perpendicular distance of the oxygen atom from the surface, and ε and σ (given in Table 2.1) are the energy and distance parameters of the surface. This potential has been previously used to model smooth surfaces that interact weakly with water and impose little order in the liquid

2.1. Molecular Models

Parameter	Six-site	TIP4P/Ice	Surface
σ (Å)	3.115 _{OO} 0.673 _{HH}	3.1668 _{OO}	2.473 _{OS}
ε (KJ/mol)	0.715 _{OO} 0.115 _{HH}	0.8822 _{OO}	1.932 _{OS}
r_1 (Å)	0.980	0.9572	
r_2 (Å)	0.230 _{OM} 0.8892 _{OL}	0.1577 _{OM}	
q^+ (e)	+0.477	+0.5897	
q^- (e)	-0.866 _M -0.044 _L	-1.1794 _M	
θ (deg)	108.00 _{HOH}	104.52 _{HOH}	
ϕ (deg)	54.00 _{MOH} 111.00 _{LOL}	52.26 _{MOH}	

Table 2.1: Water model and surface parameters used in the simulations. Note that ε and σ are the energy and distance parameters for the interaction calculation, r_1 is the oxygen-hydrogen bond distance, r_2 is the distance between the oxygen and the negative charges (OM or OL), q is the charge on each site, and θ and ϕ are angles associated with different sites in water molecules. The subscripts HOH, MOH and LOL indicate the angles between two hydrogen atoms, between the negative charge M and the hydrogen atom, and between the two lone pair charge sites. Note that L is short for lone pair (LP).

[76].

For all systems considered, periodic boundary conditions are implemented in order to eliminate surface effects. The original simulation box is replicated throughout space to form an infinite lattice. The periodicity retains a central

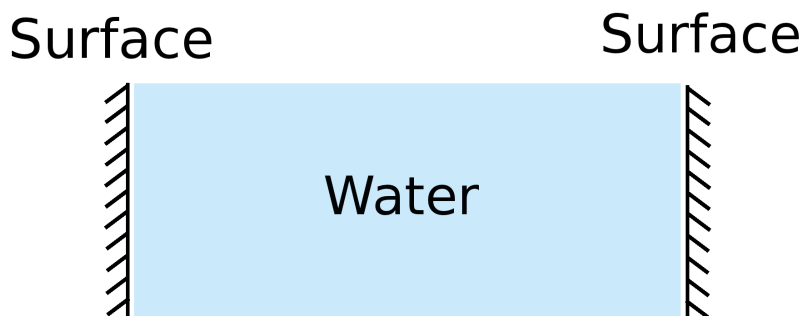


Figure 2.2: Schematic of the confined water systems. The surfaces are denoted as two vertical lines, and the water molecules are placed between them.

simulation cell with a constant number of molecules, and also allows water molecules to interact with each other and with periodic images. Bulk systems are periodic in x, y and z directions, and for confined systems, we adopt a simulation cell consisting of two parallel walls and two empty regions outside of the walls, which is replicated in the x, y and z directions. The empty area should be large enough to get extremely small interactions between water confined in the original box and the periodic boxes in the z direction.

Water molecules interact with each other through Lennard-Jones (LJ) potentials between atoms and electrostatic (Coulombic) interactions between charges [77]. In the TIP4P/Ice water model, the LJ potential between different molecules is only located on the oxygen atoms, while in the six-site model, both oxygen and hydrogen atoms interact with each other through LJ potentials. In both models, charged sites account for the electrostatic potential. The configurational energy of water is calculated by summing up

the Lennard-Jones and Coulombic interactions over all sites in all water molecules. There is an additional water-wall potential for the confined systems when surfaces are present. Details of potential calculations are discussed in the next section.

2.2 Interaction Potentials

As noted above, the intermolecular interactions are modelled through Lennard-Jones potentials between pairs of atoms, and Coulombic potentials acting between pairs of charges such that

$$u(r_{ij}) = 4\varepsilon \left[\left(\frac{\sigma_{ij}}{r_{ij}} \right)^{12} - \left(\frac{\sigma_{ij}}{r_{ij}} \right)^6 \right] + u_{ij,Coul}, \quad (2.2)$$

where r_{ij} is the distance between two atoms, ε_{ij} and σ_{ij} are the energy and distance parameters. Note that the second term in Equation (2.2) only accounts for sites with charges. The LJ potential is truncated spherically at a reasonable cutoff distance ($\sim 10 \text{ \AA}$) to improve the efficiency of calculation, which may vary a little in different systems. For interactions between different types of atoms, LJ parameters are calculated according to the Lorentz-Berthelot mixing rules [78, 79]

$$\sigma_{ij} = (\sigma_i + \sigma_j)/2, \quad (2.3)$$

$$\varepsilon_{ij} = \sqrt{\varepsilon_i \varepsilon_j}, \quad (2.4)$$

2.2. Interaction Potentials

where σ_i and ε_i are listed for the different models in Table 2.1. The total LJ contribution to the configurational energy is a summation of pairwise LJ interactions over all pairs of atoms.

In our model, there are Coulombic interactions between electrically charged atoms or sites in different molecules. The Coulombic potential is given by

$$u_{ij,Coul} = \frac{1}{4\pi\varepsilon_0} \frac{q_i q_j}{r_{ij}} \quad (2.5)$$

where ε_0 is the permittivity of free space, q_i and q_j are a pair of charges i and j , and r_{ij} is the distance between the charges.

The Coulombic potential is a long-range interaction. The long-range interaction falls off slowly as $1/r_{ij}$, and its significant range is usually greater than half the simulation box length. The charges on each molecule will not only interact with molecules in the central simulation cell, but also with all images in the periodic cells. The total Coulombic potential energy of the system can be expressed as

$$U_{Coul} = \frac{1}{8\pi\varepsilon_0} \sum_{\mathbf{n}} \sum_{i=1}^N \sum_{j=1}^N \prime \frac{q_i q_j}{|\mathbf{r}_{ij} + \mathbf{n}L|}, \quad (2.6)$$

where L is the original box length, N is the total number of charges, \mathbf{r}_{ij} is a vector joining site i and j , and \mathbf{n} is an integer vector denoting either the original simulation box or periodic image. The prime indicates that we omit $i = j$ for $\mathbf{n} = 0$. Further periodic images are constructed and a sphere of simulation boxes is generated, such that interactions with ions in the original box can be explicitly calculated [77].

2.2. Interaction Potentials

In practice, Equation (2.6) is slowly converging and conditionally convergent. The Ewald method can be used to tackle the long-range forces with efficiency, and was developed to sum the interactions between charges and all of their periodic images [77, 80, 81]. The charge density distribution of each point charge in the system is split into two terms by adding and subtracting a Gaussian distribution. It is assumed that each point charge is surrounded by a Gaussian charge distribution of different sign, with the functional form

$$\rho_i(r) = q_i \kappa^3 \exp(-\kappa^2 r^2) / \pi^{3/2}, \quad (2.7)$$

where the parameter κ determines the width of the Gaussian distribution, and r is the position relative to the center of the distribution. This extra distribution serves to screen the interaction between point charges, such that the screened interactions are now short-ranged and will converge more rapidly. A cancelling Gaussian distribution with the opposite sign of Equation (2.7) is considered. This cancelling distribution recovers the overall potential of the original set of charges. By taking a Fourier transform, the cancelling distribution can be summed in reciprocal space.

In other words, Equation (2.6) is split into two terms, which are called real space (U_r) and reciprocal space (U_k) terms. However, all charges are treated equally in the Ewald summation technique, and the interactions between charges from the same molecule are included. In order to eliminate the unwanted interactions between charges within the same molecule, two additional terms must be subtracted. Thus, the total Coulombic potential

2.2. Interaction Potentials

energy is

$$U_{Coul} = U_r + U_k - U_s - U_d, \quad (2.8)$$

where U_r, U_k, U_s, U_d are the real space term, the reciprocal space term, the Gaussian term, and the self-energy correction, respectively. Each term is described in detail as follows.

In the Ewald method, the real space energy calculation is truncated by the $\text{erfc}(x)$ function as

$$U_r = \frac{1}{8\pi\epsilon_0} \sum_i^N \sum_j^N \sum_{\mathbf{n}} \frac{q_i q_j \text{erfc}(\kappa|\mathbf{r}_{ij} + \mathbf{n}|)}{|\mathbf{r}_{ij} + \mathbf{n}|}, \quad (2.9)$$

where $\text{erfc}(x)$ is the complementary error function. κ is usually chosen such that only ($\mathbf{n} = 0$) contributes to U_r

The summation calculated in reciprocal space is

$$U_k = \frac{1}{2\epsilon_0 L^3} \sum_{\mathbf{k} \neq 0} \sum_i^N \sum_j^N \frac{q_i q_j}{k^2} \exp(-\mathbf{k}^2/4\kappa^2) \cos(\mathbf{k} \cdot \mathbf{r}_{ij}), \quad (2.10)$$

where $\mathbf{k} = 2\pi\mathbf{n}/L^2$ is a reciprocal space vector. For systems with hundreds of water molecules, we typically choose $\kappa = 6/L$ for the real space calculation, and 1200 \mathbf{k} -vectors in reciprocal space. The real space contribution will be negligible beyond some cutoff, and is confined to the central simulation box ($\mathbf{n} = 0$), and the reciprocal term can be easily calculated with 1200 reciprocal lattice vectors.

In addition, a self-energy term, U_s , for interactions of the cancelling Gaussian distribution with itself should be subtracted. For molecular sys-

2.3. Models of Electric Fields

tems, another self-energy term, U_d , accounting for intra-molecular interactions should also be taken out of the total potential energy [77]. The Gaussian term U_s is

$$U_s = \frac{\kappa}{4\pi^{3/2}\epsilon_0} \sum_i^N q_i^2, \quad (2.11)$$

where the summation is over all charges q_i . The self-energy term for a molecular system is

$$U_d = \frac{1}{4\pi\epsilon_0} \sum_i \left(\sum_a q_a \sum_b q_b \frac{\text{erf}(\kappa|\mathbf{d}|)}{|\mathbf{d}|} \right), \quad (2.12)$$

where a and b are different charges in the same molecule i and \mathbf{d} is the vector between a and b [77]. Note that Equation (2.8) allows for the calculation of the Coulombic potential energy of a simulation cell surrounded by a conductor with a dielectric constant $\epsilon' = \infty$.

Forces due to Coulombic interactions are calculated for each term in Equation (2.8).

2.3 Models of Electric Fields

A polar liquid, such as water, will undergo reorientation when exposed to an external electric field. The field interacts with the molecule by exerting a force on each charge. A uniform field will not influence the translational motion of the molecule, but rotate the dipole to the field direction. The water-field interaction energy is calculated through a summation over all

2.3. Models of Electric Fields

charges in the system

$$U_{ef} = - \sum_{i=1}^N q_i (\mathbf{r}_i \cdot \mathbf{E}), \quad (2.13)$$

where q_i and \mathbf{r}_i is the magnitude and the position vector of the i th charge, N is the total number of charges in the system, and \mathbf{E} is the electric field vector. The force on the i -th charge q_i due to the external field is calculated by

$$\mathbf{F}_{ef}^i = q_i \cdot \mathbf{E}. \quad (2.14)$$

In this thesis, confined water systems are investigated, where molecules near one surface experience an external electric field parallel to that surface. The simple model we first consider is a decaying field which extends some distance from the surface, and dies off very quickly. The half value of the field is marked as a yellow line in Fig. 2.3. Also, we consider field bands (infinite in x , and finite in y and z) with cross sectional areas that are rectangular, triangular, and semicircular in shape, as shown in Fig. 2.3. This electric field retains its maximum magnitude inside the field bands, and then decreases rapidly to zero.

The functional form selected for the field model is rather arbitrary. The field $\mathbf{E}(z)$ is given by the function

$$\mathbf{E}(z) = E_{\max} \left(\frac{1}{1 + e^{a(f(y,z)-c)}} \right) \hat{\mathbf{y}}, \quad (2.15)$$

where E_{\max} is the maximum magnitude of the field, $f(y, z)$ is a function of the molecular position relative to the surface, $\hat{\mathbf{y}}$ is a unit vector along the y axis, and a and c are parameters determining the extent and decay

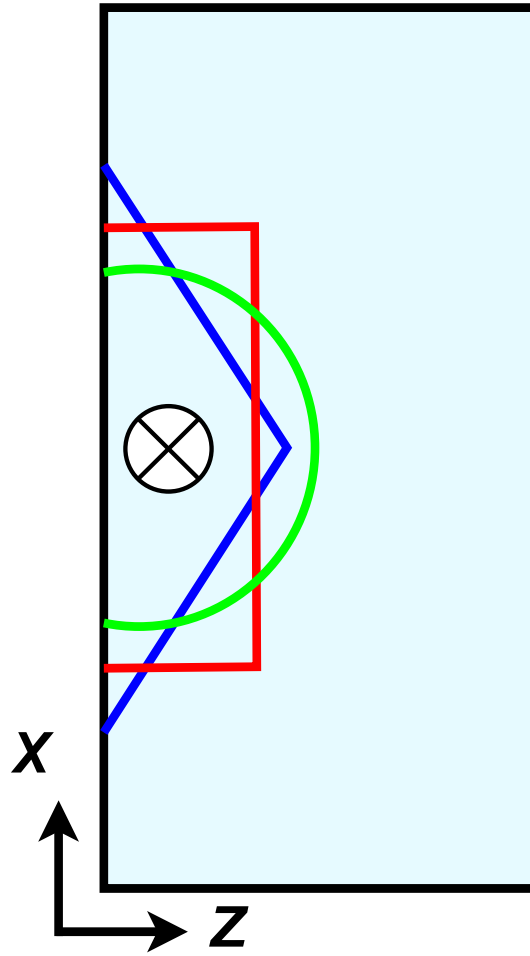


Figure 2.3: A sketch of the simulation cell showing the electric field geometries considered. The surfaces are placed at both the left and right side of the box, and the field is directed along the y axis (perpendicular to the page).

2.3. Models of Electric Fields

rate of the field as a function of z . In our model, the field is infinite in x direction, and determined by the y, z coordinates of water. Appropriate choices of $f(y, z)$ control the shape and extent of the field bands. Note that the exponential form ensures a rapid decay as indicated in Fig. 2.3.

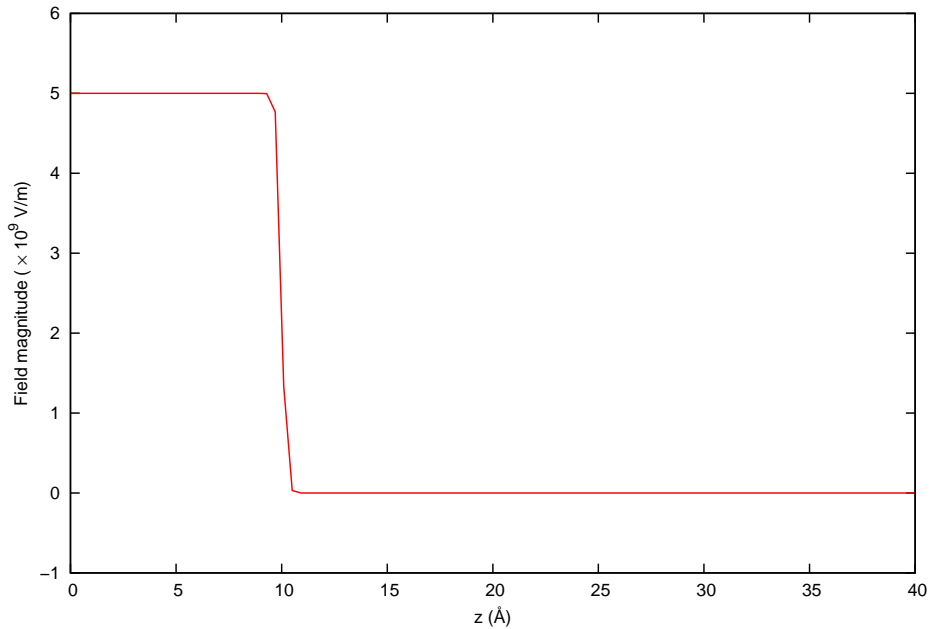


Figure 2.4: A plot showing the trend of the electric field magnitude, where $a = 10 \text{ \AA}$, $c = 10 \text{ \AA}$, and $f(y, z) = z$ in Equation (2.15). The surfaces are placed at $z = 0 \text{ \AA}$ and $z = 40 \text{ \AA}$.

For a surface field decaying only in the z direction, we choose $a = 10 \text{ \AA}$, $c = 10 \text{ \AA}$, and $f(y, z) = z$, which makes the field fall very rapidly and become insignificant beyond $\sim 10 \text{ \AA}$. The magnitude of the field is plotted as the red line in Fig. 2.4. We emphasize that Equation (2.15) is simply a convenient functional form for a field that decays with distance from a surface, it is

2.3. Models of Electric Fields

not meant to accurately represent any particular physical situation. In physical systems, the field near a surface might decay for various reasons, such as screening by mobile charges, or simply from the particular geometry and charge distribution associated with electrically neutral surfaces, as in kaolinite trenches [63]. In this thesis, E_{max} is usually set around $5 \times 10^9 \text{ Vm}^{-1}$, which is similar to the value used in earlier constant field simulations [47, 58, 62]. This field is too large to be realistic for macroscopic systems, but is not inconsistent with fields that can exist on microscopic length scales (note that the field 6 Å from an elementary point charge is $4 \times 10^9 \text{ Vm}^{-1}$).

Generally, the field is kept constant for all point charges located in the same water molecule. Thus the field exerts a torque but no translational force on a water molecule. In real physical situations, we would expect a spatially varying field to exert some force that could influence the density and packing of water molecules near a surface, and this could vary widely depending on the local features of a rough surface. However, since the details of the surface variation implied by Equation (2.15) are arbitrary, here we include only the polarizing aspects of the field, which we would expect to be always present and less sensitive to details of the field gradient. Note there are some exceptions with the field model with open source packages, which will be discussed later.

2.4 System Evolution

In molecular simulations, the system configurations are evolved in time by calculating the forces on each molecule and then integrating the equations of motion. Evaluation of the forces is the most time consuming step in a molecular dynamics simulation. Forces on each object are calculated from the interaction potential $u(r_{ij})$ described in Section 2.2,

$$\mathbf{F} = -\nabla u(r_{ij}), \quad (2.16)$$

where the ∇ is the gradient operator. For each simulation loop, forces on each molecule are updated to generate the time trajectory of the system evolution. In the following sections, how we deal with translational and rotational motion will be described separately in detail.

2.4.1 The Gear Predictor-Corrector Method for Translational Motion

For our rigid models, the molecular motion is divided into two parts; the translational motion of the center of mass and the rotational motion about the center of mass. Both depend on forces exerted on each molecule.

The force experienced by a molecule is the sum of the forces on each site within the molecule. From Newton's equation of motion, the actual acceleration \mathbf{a}^C of the center of mass is given by

$$\mathbf{a}^C = \frac{\mathbf{F}}{m}, \quad (2.17)$$

2.4. System Evolution

where \mathbf{F} and m are the total force on and the mass of the particle, respectively, and the superscript C refer to the actual value of the acceleration.

For translation, the molecule is treated as a whole, and the coordinates and motional properties are for the center of mass. To begin a simulation loop, the molecular position vector \mathbf{r} is estimated from the velocity, acceleration, and higher derivatives [84].

$$\mathbf{r}^P(t + \Delta t) = \mathbf{r}(t) + \frac{d\mathbf{r}}{dt}\Delta t + \frac{1}{2!}\frac{d^2\mathbf{r}}{dt^2}\Delta t^2 + \frac{1}{3!}\frac{d^3\mathbf{r}}{dt^3}\Delta t^3 + \frac{1}{4!}\frac{d^4\mathbf{r}}{dt^4}\Delta t^4 + \dots, \quad (2.18)$$

where the the superscript P refer to the predicted value of the position vectors. Similarly, the particle velocities \mathbf{v} and accelerations \mathbf{a} can be predicted as

$$\begin{cases} \mathbf{v}^P(t + \Delta t) &= \mathbf{v}(t) + \frac{d\mathbf{v}}{dt}\Delta t + \frac{1}{2!}\frac{d^2\mathbf{v}}{dt^2}\Delta t^2 + \dots \\ \mathbf{a}^P(t + \Delta t) &= \mathbf{a}(t) + \frac{d\mathbf{a}}{dt}\Delta t + \dots, \end{cases} \quad (2.19)$$

as well as higher derivatives. Predicted values from Equation (2.18) and Equation (2.19) can be used for energy and force calculations, and the actual acceleration \mathbf{a}^C can be obtained by Equation (2.17). Due to truncation errors, the predicted values of position vectors and their higher derivatives must be corrected to yield the right trajectory. The acceleration difference between the predicted value \mathbf{a}^P and the actual \mathbf{a}^C is

$$\Delta\mathbf{a}(t + \Delta t) = \mathbf{a}^C(t + \Delta t) - \mathbf{a}^P(t + \Delta t), \quad (2.20)$$

and this is used to correct all predicted values by

$$\begin{cases} \mathbf{r}^C(t + \Delta t) = \mathbf{r}^P(t + \Delta t) - k_0 \Delta \mathbf{a}(t + \Delta t) \\ \mathbf{v}^C(t + \Delta t) = \mathbf{v}^P(t + \Delta t) - k_1 \Delta \mathbf{a}(t + \Delta t), \end{cases} \quad (2.21)$$

where k_0 and k_1 are Gear corrector coefficients associated with position, velocity, and other derivatives, as listed in Ref. [77]. We calculated up to the 4th derivatives of coordinates in our program. Equation (2.17) is a second order equation, so the Gear corrector coefficients are 19/120, 3/4, 1, 1/2, 1/12 for coordinates, velocities, accelerations, and 3rd and 4th derivatives of coordinates, respectively. Coordinates and their higher derivatives are corrected as in Equation (2.21) and the proper configuration of the system is obtained. The Gear predictor-corrector method can be viewed as a three-stage procedure. Initially the coordinates and other time derivatives are predicted from the Taylor expansion with a truncation. Then actual accelerations are determined by new forces for the new configuration. Subsequently, all predicted values are corrected by the acceleration difference $\Delta \mathbf{a}(t + \Delta t)$, and saved for calculation in the next step [84].

The Gear predictor-corrector method is not only suitable for translational motion of molecules, but is also a good tool for rotational motion. How the rigid water models are treated for rotation is discussed in the next section.

2.4.2 Quaternions and Rotational Motion

In simulations, a molecule is moved and rotates around its own center of mass. In other words, its center of mass is tracked in a global space-fixed coordinate system, while in each molecule, positions of off-center sites are defined with respect to its own body-fixed coordinate system. For small, rigid, non-linear models, quaternions are introduced to represent the orientation of the body-fixed frame with respect to the global space of the simulation box [77, 82, 83]. A quaternion parameter \mathbf{Q} of a molecule is a set of four scalar quantities [77, 84],

$$\mathbf{Q} = (q_w, q_x, q_y, q_z). \quad (2.22)$$

The quaternions are not independent but satisfy the relation

$$q_w^2 + q_x^2 + q_y^2 + q_z^2 = 1. \quad (2.23)$$

Quaternions, associated with each molecule, are randomly assigned at the beginning of a simulation, and the values of (q_w, q_x, q_y, q_z) should be rescaled according to the magnitude $\sqrt{q_w^2 + q_x^2 + q_y^2 + q_z^2}$ to satisfy Equation (2.23).

For each molecule, it is requisite to know its position and orientation in order to evaluate all interactions with other molecules. To make the force calculations easier, global space-fixed positions of all molecular sites are crucial. With the help of a rotation matrix A , the space-fixed coordinates \mathbf{r} and body-fixed coordinates \mathbf{d} are connected. The space-fixed positions of

2.4. System Evolution

each site a in a molecule i can be obtained by [77, 82, 84, 85]

$$\mathbf{r}_{ia} = \mathbf{r}_i + A^{-1} \mathbf{d}_{ia}, \quad (2.24)$$

where the rotation matrix A is defined as [77, 84]

$$A = \begin{pmatrix} q_w^2 + q_x^2 - q_y^2 - q_z^2 & 2(q_x q_y + q_w q_z) & 2(q_x q_z - q_w q_y) \\ 2(q_x q_y - q_w q_z) & q_w^2 - q_x^2 + q_y^2 - q_z^2 & 2(q_x q_y + q_w q_x) \\ 2(q_x q_z + q_w q_y) & 2(q_x q_y + q_w q_x) & q_w^2 - q_x^2 - q_y^2 + q_z^2 \end{pmatrix}. \quad (2.25)$$

The quaternions also satisfy the equations of motion [77, 82]

$$\begin{pmatrix} \dot{q}_w \\ \dot{q}_x \\ \dot{q}_y \\ \dot{q}_z \end{pmatrix} = \frac{1}{2} \begin{pmatrix} q_w & -q_x & -q_y & -q_z \\ q_x & q_w & -q_z & q_y \\ q_y & q_z & q_w & -q_x \\ q_z & -q_y & q_x & q_w \end{pmatrix} \begin{pmatrix} 0 \\ \omega_x^b \\ \omega_y^b \\ \omega_z^b \end{pmatrix}, \quad (2.26)$$

where ω^b represents the angular velocity for each molecule in the body-fixed frame.

The rotational motion is governed by the torque $\boldsymbol{\tau}$. The torque for each molecule can be calculated as the cross product of the forces on each site and the distance to the center [77, 82],

$$\boldsymbol{\tau}_i = \sum_a \mathbf{d}_{ia} \times \mathbf{f}_{ia}, \quad (2.27)$$

where \mathbf{d}_{ia} is the position vector of atom a relative to the center of the molecule i . With the help of the rotation matrix, the torque in the body-

2.4. System Evolution

fixed system is

$$\boldsymbol{\tau}_i^b = A\boldsymbol{\tau}_i = A \sum_a \mathbf{d}_{ia} \times \mathbf{f}_{ia}, \quad (2.28)$$

and is used to calculate the first derivatives of the rotational velocities

$$\begin{aligned} \dot{\omega}_x^b &= \frac{\tau_x^b}{I_{xx}} + \left(\frac{I_{yy} - I_{zz}}{I_{xx}} \right) \omega_y^b \omega_z^b, \\ \dot{\omega}_y^b &= \frac{\tau_y^b}{I_{yy}} + \left(\frac{I_{zz} - I_{xx}}{I_{yy}} \right) \omega_z^b \omega_x^b, \\ \dot{\omega}_z^b &= \frac{\tau_z^b}{I_{zz}} + \left(\frac{I_{xx} - I_{yy}}{I_{zz}} \right) \omega_x^b \omega_y^b, \end{aligned} \quad (2.29)$$

where I_{xx} , I_{yy} and I_{zz} are the three principal moments of inertia for each model. Note that I_{xx} , I_{yy} and I_{zz} are calculated for each water model, and differ from the values of real water because of the positions of the atoms.

As for the translational motion in Section. 2.4.1, both the quaternions and angular velocities can be handled by the Gear predictor-corrector method. Similarly, up to 4th order derivatives are tracked, but the quaternions and angular velocities follow first-order differential equations, so the Gear corrector coefficients [77] for quaternions or angular velocities and their higher derivatives are 251/720, 11/12, 1, 1/3, 1/24, respectively.

At the beginning of a step in a simulation, the quaternions and angular velocities are predicted, as are their higher derivatives. Predicted quaternions associated with positions of the centres of mass are used to obtain the space-fixed coordinates, and then to calculate interactions and forces acting on the sites. From the force calculations, the torques are obtained by Equation (2.27), and then the first derivatives of angular velocities can be evaluated according to Equation (2.29). The difference between predicted values and values from Equation (2.29) are used to correct angular velocities

and their higher derivatives. Quaternions are treated in the same way as angular velocities. Note that the magnitude of a quaternion must be checked and rescaled to 1 at every time step.

For both translation and rotation, the Gear predictor-corrector method is fast and tolerant of relatively large time steps, for example, 2 femtoseconds. It is one of the most widely used predictor-corrector algorithms for molecular dynamics. The prediction part is applied at the beginning of every time step, and the correction part is applied after the force evaluation. This method is usually implemented to generate long time simulation trajectories.

2.4.3 Simulation Constraints

Most simulations carried out in this work are in the canonical ensemble, which has a constant number of particles (N), volume (V) and temperature (T). A variety of thermostating methods are available to add or remove energy from the MD system, approximating a constant temperature.

The simplest method to control temperature involves velocity scaling [84] as

$$\mathbf{v}^{new} = \mathbf{v}^C \sqrt{\frac{T_{target}}{T_{actual}}}, \quad (2.30)$$

where the actual temperature is calculated as

$$T_{actual} = \frac{1}{3Nk} \sum_i m_i |\mathbf{v}_i^C|^2, \quad (2.31)$$

where k is the Boltzmann constant. Periodic temperature scaling is essential in a simulation, but simply rescaling the velocities of molecules is too

“severe”.

A weaker coupling method can introduce energy fluctuations in order to simulate a canonical ensemble. A constraint thermostat, also referred to as a Gaussian thermostat [84, 86], is widely used for MD simulations. It introduces a temperature constraint into the equation of motion. The basic idea of this thermostat is to use a friction factor ξ to rescale velocities to adjust the kinetic energy of the system to the target temperature. The equations of motion can be modified by subtracting a scaled velocity term using the friction factor [84]

$$\mathbf{a}_i^C = \mathbf{F}_i/m_i - \xi(\mathbf{r}, \mathbf{v})\mathbf{v}_i^C, \quad (2.32)$$

and ξ is determined as

$$\xi(\mathbf{r}, \mathbf{v}) = \frac{\sum_i \mathbf{p}_i \cdot \mathbf{F}_i}{\sum_i |\mathbf{p}_i|^2}, \quad (2.33)$$

where \mathbf{p}_i is the momentum of particle i , and \mathbf{F}_i is the force acting on particle i . The friction factor ξ is initially assigned to 0 and then evaluated as in Equation (2.33) at every time step. The accelerations are tuned according to Equation (2.32) instead of Newton’s equation of motion (Equation 2.17), and used for corrections of other properties. Note that this thermostat also gives correct dynamical properties to linear order [86]. These calculations are performed conveniently during the correction step of the Gear predictor-corrector algorithm.

To reach the target temperature and equilibrate the system, a combination of velocity scaling and Gaussian thermostat are applied during the simulations. Usually the former method is applied every thousand steps and

the latter one implemented in integrating the equations of motion at every time step.

2.5 Comparison with Open Source Packages

Some calculations in this work were carried out using open source packages, such as GROMACS [87] and LAMMPS [88]. As they are designed to run parallel, their performances are especially good for large system with thousands of molecules, and simulation runs longer than hundreds of nanoseconds. The results agree well with those obtained with our own programs.

LAMMPS is widely used for MD simulations, and it allows us to apply varying electric fields in the system. Our model of confined water can be set up in the LAMMPS program, and the results obtained with our own code can be reproduced. The LJ potentials between molecular sites are calculated straightforwardly with a cut-off at some distance, which is the same in LAMMPS as in our program. Whereas for Coulombic interactions, the Particle-Particle Particle-Mesh method (PPPM) is used in LAMMPS instead of the standard Ewald summation [89, 90]. In common with Ewald summation, the PPPM method handles the short-range and long-range interactions separately. The basic idea of the PPPM algorithm is to calculate the short-range interactions through a direct sum, and the long-range interactions from mesh points. The short-range interactions are counted the same as the real space term in the Ewald calculation in Equation (2.9). The long-range interactions are handled by a particle-mesh technique, which converts charges of particles into a mesh of density values. The electrostatic

2.5. Comparison with Open Source Packages

potential due to the charge distribution on the mesh is determined by solving Poisson's equation using Fourier transform techniques, and then the force on a charge is calculated from the mesh field by interpolation. This method is faster than Ewald by introducing fewer mesh points than particles, and gives results as accurate as Ewald. Water-surface potentials are also identical in all programs, where the oxygen of water molecules interact with the surface.

For six-site and TIP4P/Ice water models, the LAMMPS package uses quaternions for rigid molecules [91] by computing body forces and torques from atomic forces. Differing from the Gear predictor-corrector algorithm in our code, LAMMPS uses the velocity-verlet algorithm [92] for rigid molecules. LAMMPS adopts the Nosé-Hoover thermostat to probe a correct canonical ensemble efficiently. Similar to the constraint thermostat used in our program, the Nosé-Hoover method [93, 94] introduces a thermal reservoir and a friction term in the equations of motion.

The results of our program are reproducible with the LAMMPS package for the same system. For example, the simulations in Chapter 3 were performed and compared for both LAMMPS and our programs. We get the same structure of ice, the same density profile, and the same dynamical properties. Nucleation rates may vary for different trials of the same system even in the same program, so it is hard to compare quantitatively.

For bulk water with uniform electric fields considered in Chapter 5, we use the programs of GROMACS. It is suitable for MD simulations of large system with a uniform electric field. In GROMACS, a truncated LJ potential is used for interactions between atoms and PPPM for electrostatic interactions amongst charges. In contrast with the LAMMPS package,

GROMACS uses the LINCS (linear constraint solver) algorithm for rigid water models [95]. Differing from the Gear predictor-corrector algorithm in our code, GROMACS uses the leap-frog integrator [96]. For simulations with constant temperature and constant pressure, the GROMACS package uses the Nosé-Hoover thermostat for constant temperature, and the Parrinello-Rahman barostat for constant pressure. [97, 98].

By comparing the water and ice structures, we confirmed that GROMACS and our own program are consistent with each other.

2.6 Data Analysis

During the production simulation runs, trajectories and velocities are recorded for selected time steps. These data are read and studied through analysis programs to obtain structural and dynamical properties. In this section, how we analyze the simulation data is discussed.

2.6.1 Radial Distribution Function

The radial distribution function $[g(r)]$ is a measure of the probability of finding a particle at a distance r from a reference particle, and is widely used to describe the average structure of a system. To calculate an atom-atom $g(r)$, a histogram $Hist(r)$ is constructed by counting every pair of particles at the displacement r , and then normalized to get $g(r)$ through [77]

$$g(r) = \frac{Hist(r)/N}{4\pi\rho/3[(r + \delta r)^3 - r^3]}, \quad (2.34)$$

where N is the total number of atoms considered, ρ is the bulk number density of the species, and δr is the radial shell thickness of 0.01 Å. In this thesis, the radial distribution function is usually obtained as a statistical average over 1000 “independent” configurations of a production run of more than 2 nanoseconds.

As a system evolves, $g(r)$ provides clear evidence of the structural change between fluid and crystal. Since liquid water and ice have different peaks, $g(r)$ is a useful tool to track ice nucleation, but is not sensitive enough to reflect the subtle differences between cubic and hexagonal ice structures. Another algorithm for distinguish these two ice structures is introduced in the next section.

2.6.2 The CHILL Ice Detector

The CHILL algorithm was developed by Moore *et al*, [75] to analyse ice structure and identify cubic and hexagonal ice. It uses the correlation of orientations among the first shell of water neighbours to classify molecules as cubic ice, hexagonal ice, intermediate ice, or liquid water molecules. To analyse a specified configuration, we calculate the orientational alignments for each water molecule i and its four closest neighbours j

$$a(i, j) = \frac{\sum_{m=-l}^l q_{lm}(i)q_{lm}^*(j)}{\left(\sum_{m=-l}^l q_{lm}(i)q_{lm}^*(i)\right)^{1/2} \left(\sum_{m=-l}^l q_{lm}(j)q_{lm}^*(j)\right)^{1/2}}, \quad (2.35)$$

where q_{lm}^* is the complex conjugate of q_{lm} . q_{lm} is defined as an instantaneous local order parameter, and for a particular value of l it can be calculated

through $m(= 2l + 1)$ spherical harmonics $Y_{lm}(\hat{r}_{ij})$

$$q_{lm}(i) = \frac{1}{4} \sum_{j=1}^4 Y_{lm}(\hat{r}_{ij}), \quad (2.36)$$

where \hat{r}_{ij} is the unit vector connecting water molecule i with one of its four closest neighbours j . It is arbitrarily chosen that $l = 3$, which provides the best resolution of ice structures and involves the least calculations [75].

Water molecules can be classified according to the local structure with respect to $a(i, j)$ of its four neighbours. Both cubic and hexagonal ice have four tetrahedrally coordinated neighbours in the first coordination shell and each of the four neighbours also has a tetrahedral shell. But there is a small difference in symmetry properties. Molecules classified as cubic ice contain only staggered or “chair” configurations ($a(i, j) < -0.8$), while hexagonal ice has three staggered forms and one eclipsed, or “boat” configuration ($-0.2 < a(i, j) < -0.05$) [75, 99]. In this thesis, we regard both intermediate ice and liquid as liquid water instead of distinguishing them, and pay particular attention to the two ice structures.

2.6.3 Orientational Order Parameter

An orientational order parameter is used to describe the orientational alignment of the system [64]. For a given configuration, it is defined by the vector

$$\mathbf{m}(z) = \frac{1}{N(z)\mu_w} \sum_{i=1}^{N(z)} \boldsymbol{\mu}_i, \quad (2.37)$$

where $N(z)$ is the number of water molecules in a rectangular volume element centred at z , μ_w is the dipole moment of the particular water model employed, and the vector sum is over all water dipoles in the volume element. In the present calculations, the x and y dimensions of the volume element are those of the simulation cell, and the thickness is 0.01 \AA . This order parameter is convenient to show how dipole orientation is impacted by an electric field. For an isotropic sample of random orientations, the mean value of the order parameter $\langle \mathbf{m}(z) \rangle = 0$; whereas for a perfectly aligned sample, $\langle \mathbf{m}(z) \rangle = 1$. As with $g(r)$, the orientational order parameter profiles shown here are averaged over 1000 configurations.

In addition to the structural properties discussed above, mass density profiles are calculated by dividing the system into rectangular volume elements, and counting the number of water molecules in each rectangular element. Plots of density profiles show the extension of ice growth. Molecular dynamics simulation also allows us to determine the time dependent properties of fluids, such as the diffusion coefficient. For fluid systems, the mean square displacement $\langle |\mathbf{r}(t) - \mathbf{r}(0)|^2 \rangle$ is a common measure of diffusion and is plotted as a function of time t [77]. The mean square displacement (MSD) contains information on the molecular diffusivity. For liquid system, MSD grows linearly with time, and the slope is the diffusion coefficient D

$$D = \lim_{t \rightarrow \infty} \frac{1}{6t} \langle |\mathbf{r}(t) - \mathbf{r}(0)|^2 \rangle, \quad (2.38)$$

where t is the time interval, the $\mathbf{r}(t)$ is displacement of a molecule from the beginning to t , and $\langle \dots \rangle$ denote the average over all molecules

2.6. *Data Analysis*

and configurations. The mean square displacement as well as the diffusion coefficient are useful to characterize the motional behaviour of the system.

Chapter 3

Heterogeneous Ice Nucleation Induced by Surface Electric Fields

3.1 Introduction

As discussed in Chapter 1, heterogeneous ice nucleation is an important phenomenon influencing many aspects of our physical environment, ranging from atmospheric processes to biological systems [1–3, 11, 24–26, 100]. Despite its obvious importance and interest, heterogeneous ice nucleation is poorly understood, and remains a subject of very active research. A major advance would be to gain an understanding of the microscopic feature(s) that create a good ice nucleation catalyst. The present study is a contribution toward this objective.

One argument that is often put forward [7] invokes a good crystallographic match with hexagonal ice (ice Ih) as a possible explanation of effective ice nuclei (IN). However, based on recent computer simulation studies [21, 64–67], this explanation does not appear to hold when closely

examined at a microscopic level. It appears that, at least in simulation models, atomistically smooth, defect-free surfaces are not effective IN, even if their crystallographic parameters do match those of ice. It is also worth noting that a recent experimental study [68] of kaolinite particles is more consistent with an “active site” nucleation mechanism, than with other possible explanations.

Another explanation that has been put forward for ice nucleation is the possible importance of electric fields [44, 45, 47, 53, 55–58]. Computer simulations have demonstrated [47, 58, 61] that model bulk water readily freezes on nanosecond time scales if the sample is polarized by a strong electric field. This is also true of confined water [62]. However, one should keep in mind that in previous electrofreezing simulations all water molecules interact directly with the field. Thus, the field is not acting merely to catalyze ice nucleation, but it can also influence the freezing point and the ice structure obtained. Note that the ice obtained in bulk electrofreezing simulations is ferroelectric and has the cubic ice structure (ice Ic).

In previous investigations of water on kaolinite, it was observed that for some kaolinite structures, the water near particular surfaces can be highly polarized by strong local fields [63]. Motivated by this observation, and by the earlier work on electrofreezing [47, 58, 61, 62], we examine field-induced ice nucleation for a simple model where water molecules experience a strong external field only if they are very near a surface. For a particular set of conditions, we demonstrate that such a surface field is indeed sufficient to induce ice nucleation.

This chapter reports the results of field-induced ice nucleation, and

significantly extends the work on parameters affecting the ice nucleation process. We examine the important influences of temperature and electric field parameters (strength and extent) on ice nucleation and growth. To ensure that our observations are not an artifact of a particular water model or choice of system parameters, results are reported for two different water models, and for a range of system sizes and dimensions.

The remainder of this chapter is divided into three parts. The models and simulation method are described in Section 3.2, the results are given and discussed in Section 3.3, and our conclusions are summarized in Section 3.4.

3.2 The Model and Simulation Method

We consider water confined between two infinite parallel plates that are perpendicular to the z axis, and separated by a distance L_z . The water sample occupies a simulation cell of dimensions (L_x, L_y, L_z) , that is assumed to be periodically infinite in the x and y directions. The surfaces are assumed to be smooth and interact with the water through the potential given by Equation (2.1) in Chapter 2. The water-wall interaction is relatively weak and imposes little order on water near the surface [76]. This is a desirable feature for the present work, because insofar as possible we wish to isolate the influence of electric fields from other possible surface effects.

In order to check that our results are not strongly dependent on a particular water model, simulations were performed for two models, specifically, the so-called six-site model introduced by Nada *et al.* [72], and

the TIP4P/Ice model developed by Abascal *et al.* [71], as described in Chapter 2. Both of these water models were developed with the aim of obtaining a better description of ice and melting. In these rigid models the water molecules interact via site-site potentials described by combinations of Lennard-Jones (LJ) and Coulombic interactions. The TIP4P/Ice model is a re-parameterization of the earlier TIP4P model [59], and the six-site model is a recent water model [72]. Parameters for the six-site and TIP4P/Ice models are given in Section 2.1 in Chapter 2.

For the present work, it is important to know the melting points of the models employed. For the six-site and TIP4P/Ice models the melting points of ice Ih at 1 atm have been estimated to be ~ 289 K (Ref. [101]) and ~ 270 K (Refs. [71] and [102]), respectively.

Mineral particles such as kaolinite that serve as IN in the physical environment tend to have very rough surfaces, and one might expect local fields that vary greatly both in magnitude and direction. We consider a particular situation where a field acts over a narrow region near a surface, and is directed parallel to that surface. This choice of geometry was initially motivated by our earlier observation [63] that in kaolinite trenches (particular structures associated with partially cleaving basal planes of kaolinite) there tends to be a strong electric field component acting parallel to the trench walls.

In the model of field used in this chapter, the field $\mathbf{E}(z)$ is given the functional form

$$\mathbf{E}(z) = E_{\max} \left(\frac{1}{1 + e^{a(z-c)}} \right) \hat{\mathbf{y}}, \quad (3.1)$$

where E_{\max} is the maximum magnitude of the field, z is the distance from a water oxygen atom to the surface, $\hat{\mathbf{y}}$ is a unit vector along the y axis, and a and c are parameters determining the extent and decay rate of the field as a function of z . In our model, the field is determined by the position of the oxygen atom, and is constant at that value for all point charges located in the same water molecule. Thus the field exerts a torque but no translational force on a water molecule. In real physical situations, we would expect a spatially varying field to exert some force that could influence the density and packing of water molecules near a surface, and this could vary widely depending on the local features of a rough surface. However, since the details of the surface variation implied by Equation (2.15) are arbitrary, here we include only the polarizing aspects of the field, which we would expect to be always present and less sensitive to details of the field gradient.

All simulations are carried out under NVT conditions. In the simulations reported in this chapter the temperature was kept constant employing a Gaussian isokinetic thermostat [77, 86]. However, some simulations were also carried out with a Nosé-Hoover thermostat [77], and no significant differences were observed. Specifically, ice nucleation and growth occurred in a similar fashion for both thermostats. A rectangular simulation cell with $L_x = L_y$ is used in all cases, and, as noted above, periodic boundary conditions are applied in the x and y directions. The system is finite in z , and to account for this the water densities reported are estimated

taking the cell volume to be $L_x L_y (L_z - 2\sigma)$. The equations of motion are integrated employing a fifth-order Gear predictor-corrector algorithm with a time step of 2 fs. The LJ interactions were cut and shifted at $L_x/2$ to avoid discontinuities. The Coulombic interactions in the slab geometry were treated using Ewald sums as described in Chapter 2. In the Ewald calculations, the parameter $\kappa = 6.0/L_x$, 1200 reciprocal lattice vectors were included, and the real space terms were truncated at $L_x/2$. Test runs performed with larger numbers of reciprocal lattice vectors did not show any significant differences.

In all cases the sample is first equilibrated in the liquid state well above the melting point. The system is then cooled to the target temperature and re-equilibrated as a metastable liquid before the field is applied. We note that even with many trials and runs of many nanoseconds, we never once observed ice nucleation in the absence of a field.

3.3 Results and Discussion

In this section, we demonstrate that an electric field, which acts very near a surface, can create an effective ice nucleus in models of supercooled liquid water. We also examine the influences of the system size and cell dimensions, temperature, field strength, and field extent on ice nucleation.

3.3.1 Ice Nucleation Induced by a Surface field

In this section, we present a particular simulation of heterogeneous ice nucleation induced by a surface field, in a system that has 1200 water

3.3. Results and Discussion

molecules. The density of this system is 0.96 g/cm^3 , and the simulation is performed at 270 K. Here we use $a = 10$ and $c = 10 \text{ \AA}$ in Equation (3.1), which gives a field that falls very rapidly becoming insignificant beyond $\sim 10 \text{ \AA}$. This field is plotted in Fig. 2.4 in Chapter 2. Larger values of c give results similar to those obtained with $c = 10 \text{ \AA}$, whereas smaller values did not function as IN under the conditions considered here. We emphasize that Equation (3.1) is simply a convenient functional form for a field that decays with distance from a surface, it is not meant to accurately represent any particular physical situation.

Configurational snapshots that illustrate ice nucleation and growth are shown in Fig. 3.1. At $t = 0$ (top panel), just before the field is applied, the system is a supercooled liquid and no order is discernible. At 2.4 ns (middle panel) after the field is applied to molecules within $\sim 10 \text{ \AA}$ of the surface, ice nucleation near the surface and some growth into the bulk can be clearly seen. At 4 ns (bottom panel), the ice has reached the vicinity of the opposite wall. Identical systems started from different initial conditions showed different time-dependent nucleation and growth behaviour, but ice did nucleate and grow in all examples (six with 1200 particles) considered. In order to understand the nature of the ice formed in our system, it is useful to examine the dipole order parameter profile along the z axis, and the water-water radial distribution functions.

For a specific configuration, the dipole order parameter $\mathbf{m}(z)$ is defined in Section 2.6.3 in Chapter 2. The average components of $\mathbf{m}(z)$ ($\langle m_i(z) \rangle$, $i = x, y, z$) are plotted in Fig. 3.2. We see that in the field region, the sample is highly polarized in the y direction, as we would expect, but beyond this

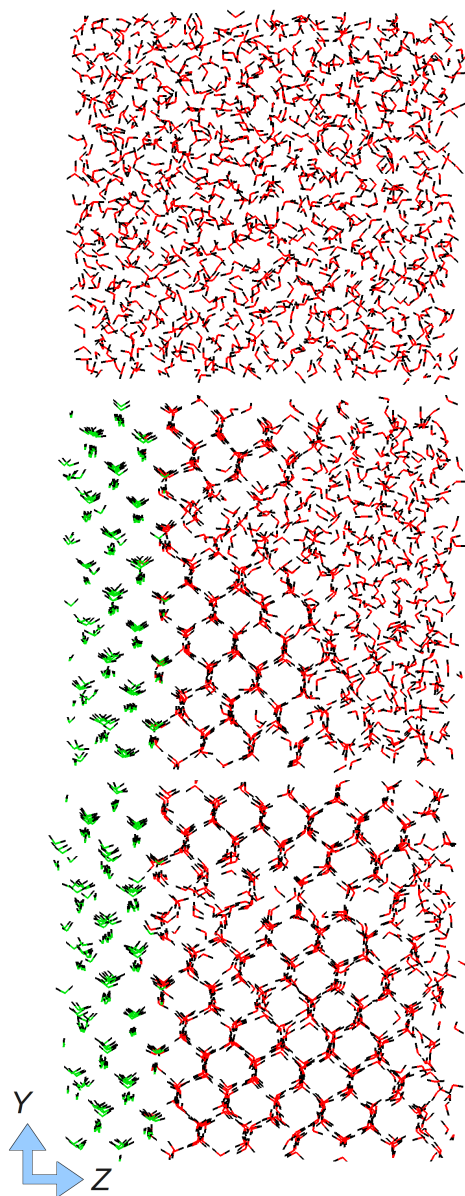


Figure 3.1: Configurational snapshots of one particular simulation with 1200 water molecules. The field (directed upwards along the y axis) was applied at $t = 0$ (upper panel), the middle ($t = 2.4$ ns) and bottom ($t = 4$ ns) panels show the nucleation and growth of ice. The oxygen atoms of the water molecules that experience the field ($z \lesssim 10$ Å) are green, those outside the field region are red, and all hydrogen atoms are black.

region the polarization rapidly dies. Thus, the narrow ice layer directly nucleated by the field is ferroelectric, but the subsequent layers are not. This is also evident in the configurational snapshots shown in Fig. 3.1. Looking closely, one can see that the protons in the surface-field region are predominately directed upwards, whereas beyond this region the protons show no orientational preference.

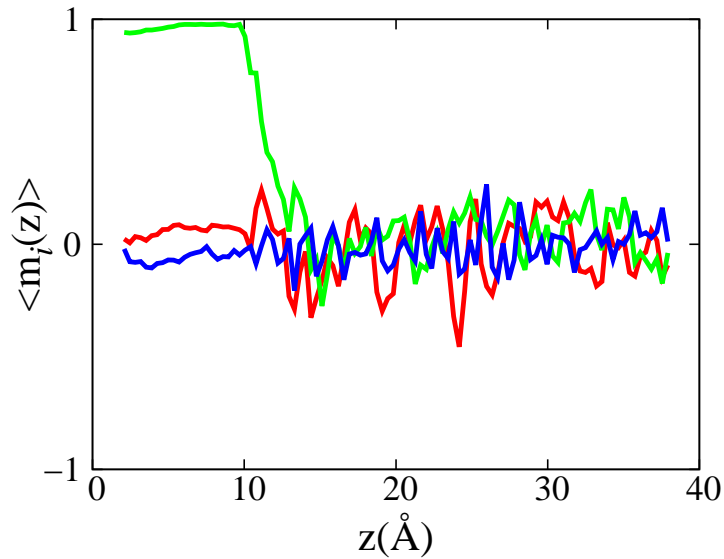


Figure 3.2: The dipole order parameter profile along the z axis for the field-nucleated, frozen sample. The red, green, and blue lines are the x , y , and z components, respectively. Note that the y component shows field-induced polarization for $z \lesssim 10 \text{ \AA}$.

Oxygen-oxygen and hydrogen-hydrogen radial distribution functions are shown in Fig. 3.3. Results are plotted for the same sample converged under field-nucleated, constant field (the field is uniform throughout the sample) and zero field conditions. The corresponding functions for bulk water frozen

3.3. Results and Discussion

into ferroelectric cubic ice under a constant field are included for comparison. The zero field curves resemble those typically obtained for liquid water. For the constant field and field-nucleated systems, the oxygen-oxygen curves are very similar, and, moreover, they closely resemble the corresponding radial distribution function of bulk cubic ice. This strongly suggests that the ice formed in our samples is also cubic, and we have confirmed this by inspecting configurational snapshots along different crystal axis. The hydrogen-hydrogen radial distribution functions for the constant field and field-nucleated systems differ significantly, reflecting the fact that the field-nucleated ice is not ferroelectric (proton ordered) beyond the field-polarized region. Our observations indicate that proton disordered cubic ice, grows onto the proton ordered, ferroelectric layer, in a near seamless manner.

Finally, it must be noted that in bulk water cubic ice is less thermodynamically stable than the usual hexagonal form, ice Ih. At first sight, our simulation results would appear to be at odds with this fact. However, cubic ice, that under certain conditions can anneal to form hexagonal ice, has been experimentally observed [103]. Also, it has been argued [104] that cubic ice is actually the preferred crystal structure for water confined to pores or to thin films ($\lesssim 100$ Å thick). Thus, our simulations suggest a plausible scenario for heterogeneous ice nucleation. The very rough particles that act as IN in the physical environment might have some surface structures where the local fields are strong enough to polarize water near the surface. Indeed, given the structural variations in most real particles that serve as IN, this possibility does not appear unlikely. Such features would serve as “active sites” for cubic ice nucleation, which could eventually convert to the more

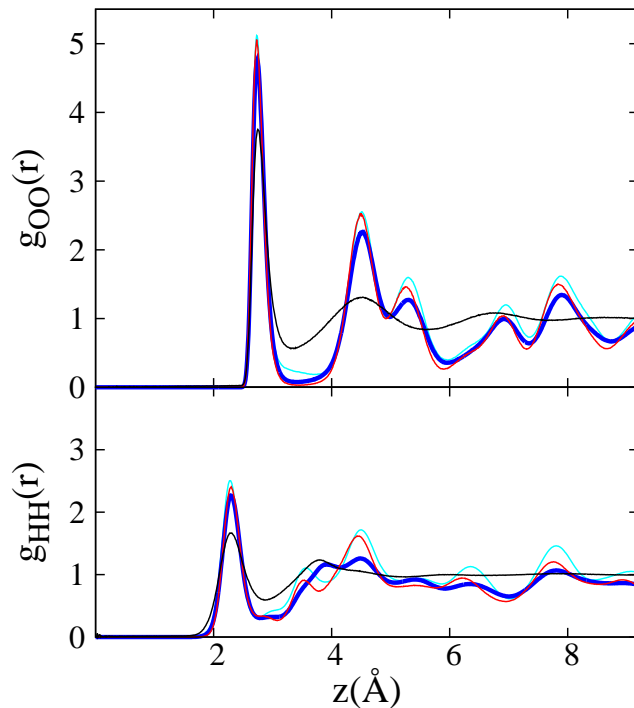


Figure 3.3: Oxygen-oxygen and hydrogen-hydrogen radial distribution functions. The black, red, and dark blue lines are the zero field, constant field, and field-nucleated results, respectively. The light blue lines represent ferroelectric bulk cubic ice frozen under a constant field.

stable hexagonal form as it grows into the bulk.

3.3.2 Ice Nucleation in Systems of Varying Size and Dimension

It is important to verify that any observation of field-induced ice nucleation and growth is not unduly influenced by finite system size. Therefore, we carried out a number of simulations for both the six-site and TIP4P/Ice

3.3. Results and Discussion

models varying the cell dimensions and the number of water molecules involved. Additionally, for each system several trial runs (not less than four) beginning with different initial conditions were performed. The parameters of the systems considered, together with the number of trials, and the total length of the runs, are summarized in Table 3.1. The number of trials that resulted in ice nucleation for a given run length is also indicated in Table 3.1. Given that we are observing ice nucleation and growth along the z axis, the surface-surface separation L_z is an important variable, and is varied between 40 Å and 80 Å in our simulations. It is important to test that our qualitative observations are independent of the surface separation, because if L_z is too small the field could influence the freezing point itself, in which case we could be observing something more closely akin to electrofreezing than to simple nucleation. The $L_x = L_y$ dimension is also varied, and the number of particles in the central cell ranges from 432 to 1800. In all cases, the density is held fixed at 0.96 g/cm³.

$L_x = L_y, L_z$ (Å)	Number of Molecules	Trials, Time (ns)
19.6, 40	432	12(12), 32 ; 8(7), 32
32.68, 40	1200	6(6), 16 ; 4(3), 16
19.16, 60	648	6(6), 16 ; 4(3), 15
31.9, 60	1800	4(2), 8 ; 4(4), 8
19.33, 80	900	9(9), 22 ; 9(9), 26

Table 3.1: The systems considered in tests of possible finite size effects. In the third column, the first and second pairs of integers give the number of trials and the run times for the six-site and TIP4P/Ice models, respectively. The number of trials for which ice nucleation was observed in the given simulation time is given in brackets.

In the simulations included in Table 3.1, the parameters used in Equation

3.3. Results and Discussion

(3.1) are $a = 10 \text{ \AA}^{-1}$, $c = 10 \text{ \AA}$, and $E_{\text{max}} = 5.0 \times 10^9 \text{ V/m}$. As noted above, these parameters produce a field that falls rapidly to insignificance at $\sim 10 \text{ \AA}$ from the wall, but is sufficiently strong to readily induce electrofreezing in bulk systems [47, 58], and ice nucleation in our geometry. The simulations summarized in Table 3.1 were carried out at 270 K for the six-site model and at 260 K for TIP4P/Ice. Given the different melting points of these models, these temperatures correspond to undercoolings of $\sim 20 \text{ K}$ and $\sim 10 \text{ K}$ for the six-site and TIP4P/Ice models, respectively. The density, estimated taking the cell volume to be $L_x L_y (L_z - 2\sigma)$ as discussed above, was fixed at 0.96 g/cm^3 , a value where bulk water has been shown [47, 58] to readily form cubic ice for the field strength given above. This density was used for all results reported in this Chapter. An analysis of the influences of varying the temperature, and the field parameters is given below.

For both water models, ice nucleation and growth was observed for all system sizes. The qualitative behaviour pattern was similar for all system sizes and dimensions, providing evidence that finite size effects are not a significant issue. Configurational snapshots for two examples with $L_z = 60 \text{ \AA}$ (648 particles) and 80 \AA (900 particles) are shown in Fig. 3.4, exhibiting two different crystallographic planes of cubic ice. We note that in these selected runs of 18 ns, the ice layer has grown to approximately the same thickness in both systems. However, as one would expect, the time required to observe ice nucleation and growth varies considerably for different trials of the same system. The number of trials for which ice nucleation and growth was observed for a given run length is reported in Table 3.1. Once nucleation has occurred the ice grows through the bulk toward the opposite surface, as

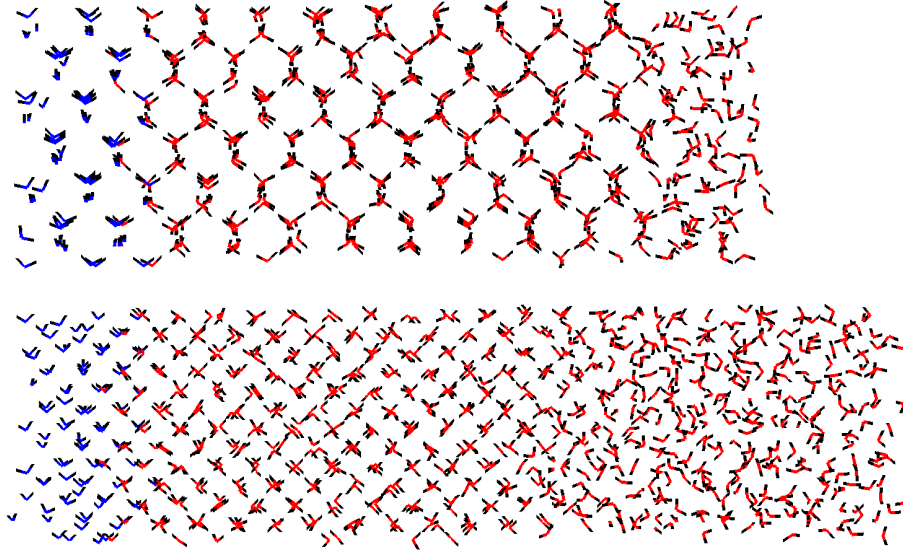


Figure 3.4: Configurational snapshots after 18 ns of two selected trial runs that show ice nucleation and growth. In one system (top), $L_z = 60 \text{ \AA}$ (648 particles) and in the other (bottom) $L_z = 80 \text{ \AA}$ (900 particles). The oxygen atoms of water molecules that experience the field are blue, those outside the field region are red, and all hydrogen atoms are black. The top and bottom projections can be recognized as the (101) and (001) crystallographic planes of cubic ice, respectively.

can be seen in Fig. 3.4.

Ice nucleation and growth can be detected and followed by plotting the water-water interaction energy as a function of time. Example plots for eight trial runs of the six-site model with 432 particles are shown in Fig. 3.5. We observe that the interaction energy decreases a little when the field is turned on at 2 ns. It then oscillates about a near constant value until ice nucleation occurs, at which point the energy decreases and continues to decrease until essentially the entire sample is frozen. Note that for the eight

3.3. Results and Discussion

trials shown in Fig. 3.5, the time required to observe ice nucleation varies from ~ 2.5 ns to ~ 22.5 ns.

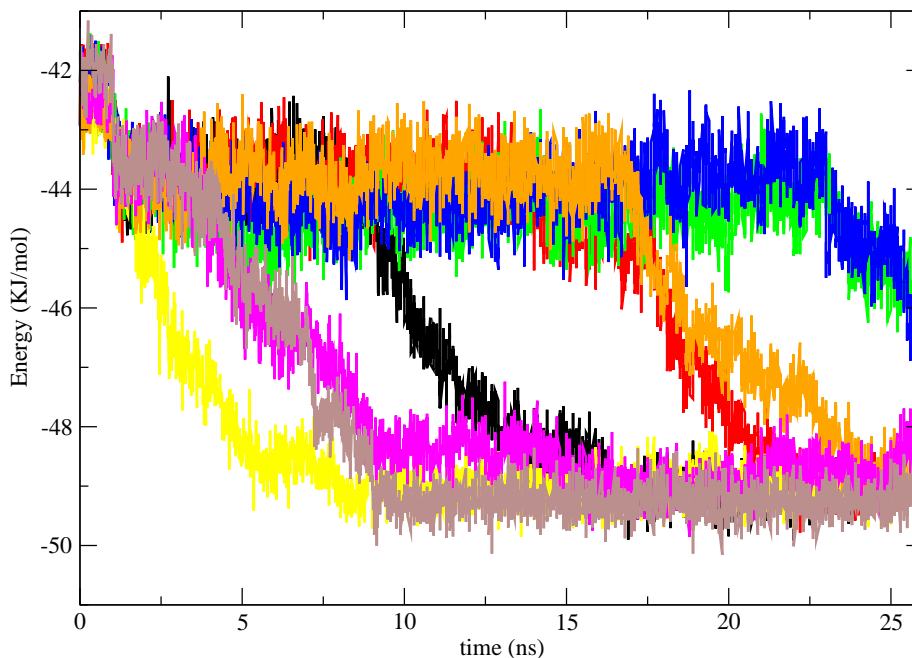


Figure 3.5: The water-water contribution to the configurational energy for the six-site model at 270 K. Results for eight trial runs of the 432 particle system are shown. The field was applied at 2 ns. Note that all eight trials show clear nucleation and freezing, as signalled by a rapid drop in the water-water interaction energy.

The field-nucleated ice formed in our model systems is cubic, as is the case for electrofrozen bulk ice [47, 58]. The oxygen-oxygen radial distribution functions, examples of which are plotted in Fig. 3.6 and compared with the result obtained for bulk cubic ice electrofrozen under similar conditions, provide some evidence for this structure. The cubic ice structure can also

3.3. Results and Discussion

be seen by inspection of configurational snapshots, as was previously done for electrofrozen bulk samples [47, 58]. Note in particular that the (001) crystallographic plane shown in Fig. 3.4 is a clear indication of cubic ice. Additionally, we examined a number of configurations for different system sizes employing the so-called CHILL algorithm, previously used by Moore *et al.* [75] to distinguish between cubic and hexagonal ice. This confirmed that the ice nucleated and grown in our model systems is cubic. A further discussion of cubic versus hexagonal ice is given in section 3.4, below.

Although we obtain the same cubic structure, the ice obtained in the present field-nucleated systems differs from the bulk electrofrozen case (where all water molecules experience the field), in that only the narrow region that directly experiences the field is ferroelectric. The ice grown beyond this region is not polarized. This can be seen by calculating the dipole order parameter profile. In our model, the field has no x or z component, and the corresponding components of $\mathbf{m}(z)$ average to ~ 0 . The average y component, $\langle m_y(z) \rangle$, is shown in Fig. 3.7 for two trials of the 432 particle system, and we see that the order parameter is ~ 1 in the field region, but falls rapidly to ~ 0 , as the field decays at $\sim 10 \text{ \AA}$ from the surface. Thus, non-polarized ice nucleates and grows outward from the ferroelectric layer.

For both frozen samples, density profiles along the z direction are also included in Fig. 3.7. These are obtained using the same rectangular volume elements described above for the polarization profiles. Interestingly, the density profiles obtained for the different trials are not the same. Both show regular density oscillations, but the interlayer spacings are different. This demonstrates that fixing the field direction and the cell geometry does not

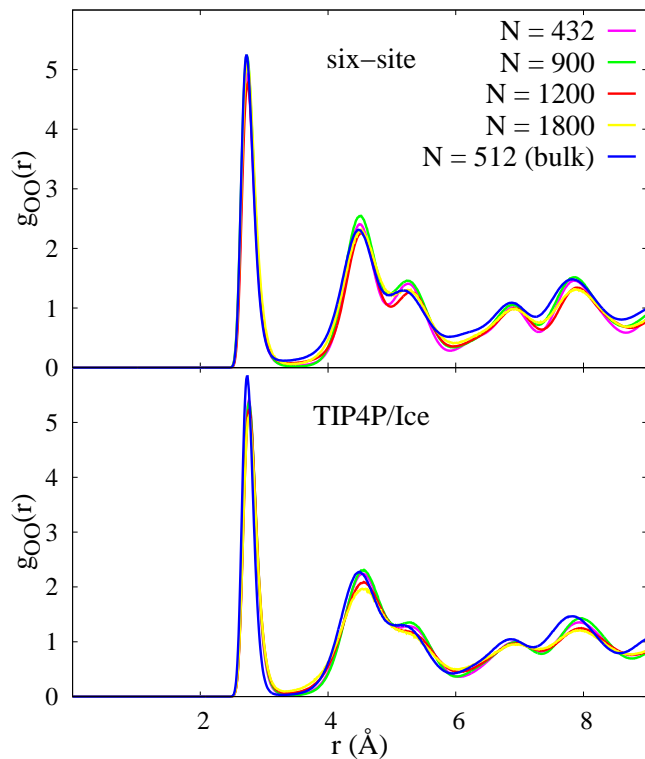


Figure 3.6: Oxygen-oxygen radial distribution functions for the six-site (top panel) and TIP4P/Ice (bottom panel) models. Curves for different system sizes are shown, and compared with the bulk cubic ice result.

fix the crystal axes of the ice formed, different orientations with respect to the surface remain possible. This is further illustrated in Fig. 3.8, where configurational snapshots “taken” from the same perspective are shown for both ice structures. Clearly the crystal axes have different orientations within the simulation cell. Other orientations are possible, and in some cases regular oscillations are not seen in the density profile along z . In such cases, the density profiles cannot be used to track ice nucleation and growth,

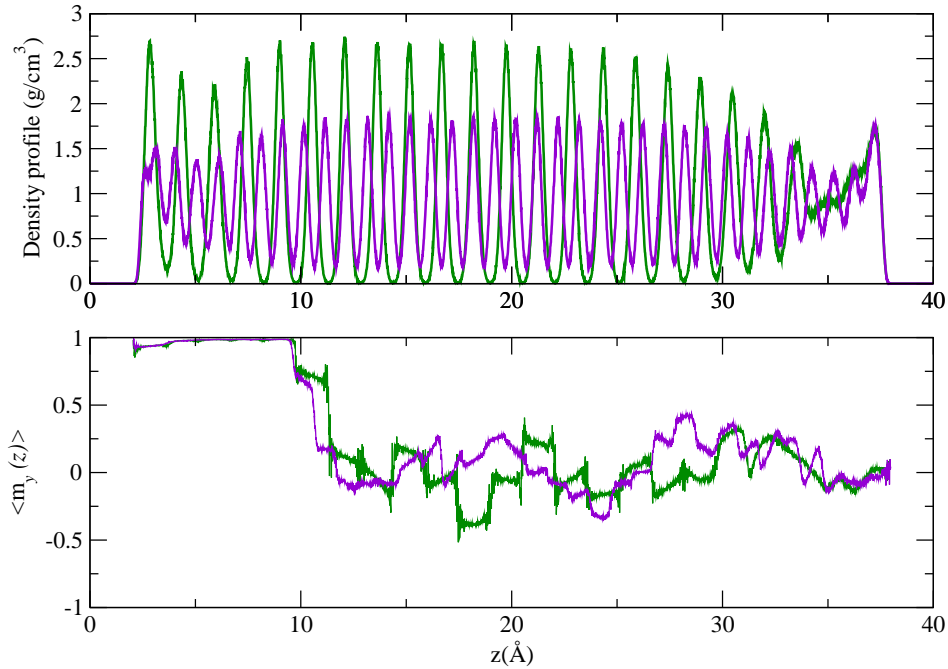


Figure 3.7: Density (top panel) and dipole order parameter (bottom panel) profiles for two trial runs of the six-site model with 432 particles.

and one must rely on that energy and/or configurational snapshots.

3.3.3 Influence of Temperature

It is interesting to establish the temperature range over which ice nucleation and growth can be observed in simulations. Therefore, calculations were carried out over a range of temperatures for both models. In these calculations, the parameters in Equation (3.1) were again held fixed at $a = 10 \text{ \AA}^{-1}$, $c = 10 \text{ \AA}$, and $E_{\text{max}} = 5.0 \times 10^9 \text{ V/m}$. All simulation runs were equilibrated above the freezing point, and cooled to the target temperature before the

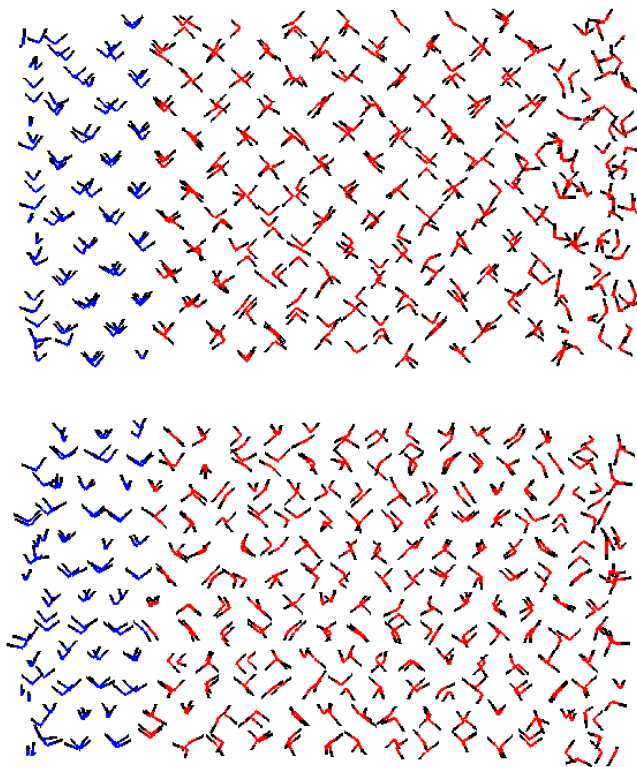


Figure 3.8: Configurational snapshots of the two trial runs for which density profiles are shown in Fig. 3.7. Both snapshots are of the configuration at the 32nd nanosecond, and both are from the same perspective. The oxygen atoms of the water molecules that experience the field are blue, those outside the field region are red, and all hydrogen atoms are black. The ice crystals clearly have different orientations in the simulation cell.

field was turned on. In the six-site case, simulations were carried out with both 432 and 1200 particles (see Table 3.1 for details) for all temperatures, and our observations were consistent for both system sizes. This is also true for the TIP4P/Ice model for 260 K and higher temperatures. At lower

3.3. Results and Discussion

temperatures only 432 particle systems were considered for the TIP4P/Ice model, but given that no significant system size dependence was observed at other temperatures, or for the six-site model which was tested everywhere, we would not expect any in the TIP4P/Ice systems at low temperatures. The number of trials and the run lengths varied depending to some extent on how readily (or not) ice nucleation and growth could be seen.

six-site		TIP4P/Ice	
Temp. (K)	Ice Nuc.	Temp. (K)	Ice Nuc.
230	No	230	No
240	No	240	No
250	Yes	245	Yes
260	Yes	250	Yes
270	Yes	260	Yes
280	Yes	265	Yes
285	No	270	Yes
290	No	275	No

Table 3.2: Temperatures considered for the six-site and TIP4P/Ice models. Yes and No indicate whether ice nucleation and growth was observed or not at the particular temperature.

The temperatures considered and our qualitative observations are summarized in Table 3.2. If “Yes” is entered in the ice nucleation (Ice Nuc.) column, then ice nucleation and growth was observed for at least one trial at that temperature. If two system sizes were considered, as was usually the case (see above), then this is true of both. If “No” is entered, then ice nucleation and growth was not at all observed at the temperature in question. Of course, it is always possible that with more and/or longer simulation runs ice nucleation might occur, but one can at least conclude that ice nucleation is much less likely outside of the temperature ranges

3.3. Results and Discussion

indicated in Table 3.2.

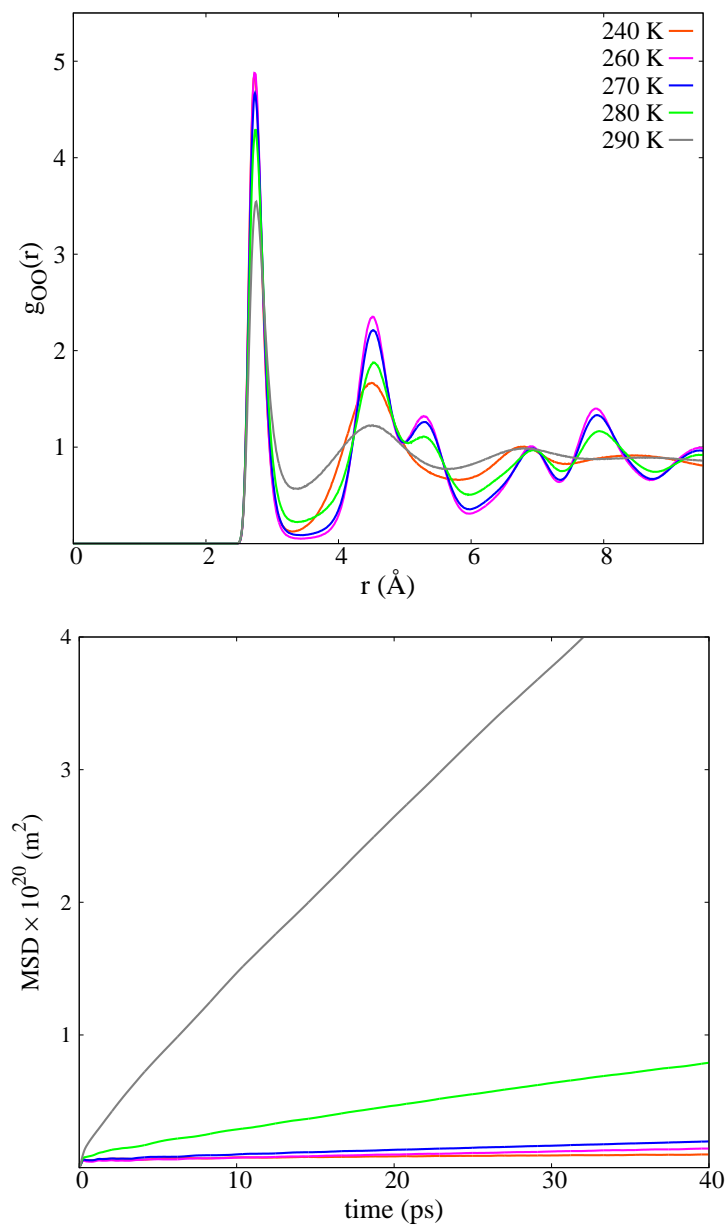


Figure 3.9: Oxygen-oxygen radial distribution functions and mean square displacement (MSD) curves for the six-site model at different temperatures.

3.3. Results and Discussion

From Table 3.2, we see that ice nucleation and growth was observed from 250 - 280 K for the six-site model, and from 245 - 270 K for TIP4P/Ice. Noting again that the normal melting points of hexagonal ice (ice Ih) have been estimated to be ~ 289 K for the six-site model [101] and ~ 270 K for TIP4P/Ice [71, 102], we would not expect to see ice nucleation above these temperatures, and in fact we do not. However, it should be noted that our model system forms cubic ice (ice Ic) rather than the hexagonal form. The melting points of cubic ice for the six-site and TIP4P/Ice models are not known, but they are expected to be lower than those of hexagonal ice. In fact for the six-site model, cubic ice has been shown [72] to be less stable than the hexagonal form, consistent with real water. This obviously raises questions as to why cubic ice prefers to grow in our model, and a further discussion of this issue is given below (Section 3.4).

The fact that we did not observe ice nucleation and growth at 240 K and lower temperatures might be puzzling at first sight, but it is in all likelihood an artifact of the finite time (32 ns) of our simulation runs. At low temperatures, our model liquids become very glass-like and remain in amorphous disordered states on simulation time scales. It is possible that much longer simulation runs would extend our ice observation to slightly lower temperatures, but we haven't pursued this possibility, since it is unlikely that anything new would be learnt from such efforts. Suffice to say, that on convenient simulation times scales ice nucleation and growth can be readily observed over the range 250-280 K for the six-site model, and 245-270 K for TIP4P/Ice.

Oxygen-oxygen radial distribution functions obtained for the six-site

model at different temperatures are plotted in Fig. 3.9. We note that at 290 K and 240 K, the radial distribution functions do not show any ice-like structure. At 290 K, the model is above the freezing point and remains a stable liquid, and at 240 K we obtain a “frozen” amorphous state, as discussed above. Further evidence for this is provided by Fig. 3.9, where the molecular mean square displacements ($\langle |\mathbf{r}(t) - \mathbf{r}(0)|^2 \rangle$) for different temperatures are plotted as functions of time t . We note that diffusion in the amorphous system at 240 K is very low, less in fact than that found in the ice formed at higher temperatures. The radial distribution functions and mean square displacement plots for the TIP4P/Ice model exhibit similar temperature dependences.

3.3.4 Influence of Field Strength and Extent

An electric field near a surface can create an effective ice nucleus in models of supercooled liquid water. To serve as an ice nucleus, the field must polarize only a very thin water layer ($\sim 10 \text{ \AA}$), and the field strength required is realistic on the relevant length scale. Our results support the idea that local electric fields could play a major role in heterogeneous ice nucleation, particularly for the very rough particles with many surface structure variations, that serve as ice nuclei in environmentally realistic situations.

Clearly, an electric field is a very effective agent of ice nucleation, and it is of interest to ask how this effectiveness varies with field strength and extent. Note that by field extent we mean the distance from the surface where the field maintains significant strength. In our simulations, the field is modelled by Equation (3.1), with E_{\max} and c effectively determining the

3.3. Results and Discussion

field strength and extent, respectively. With the parameter a fixed at 10 \AA^{-1} , the field remains nearly constant up to a distance c , and then decays, rapidly becoming insignificant. The rapid drop in field is mirrored by a rapid drop in the dipole order parameter, as discussed above (Fig. 3.7).

A number of calculations were carried out with field strengths below $5 \times 10^9 \text{ V/m}$, and with c values of 10 and 20 \AA . These calculations were performed at 270 K for the six-site model and at 260 K for TIP4P/Ice. Most simulations were done with 432 particles, but runs with systems of 648 and 1200 particles (see Table 3.1 for details) were performed for some cases, and again our qualitative observations proved to be independent of system size. If ice nucleation was not observed, trial runs were continued up to 32 ns.

c (\AA)	$E_{\text{max}} \times 10^{-9}$ (V/m)	Ice Nuc.	
		six-site	TIP4P/Ice
10	1.5	No	No
10	2.5	No	Yes
10	3.5	Yes	Yes
20	1.5	Yes	Yes
20	2.5	Yes	Yes

Table 3.3: The dependence of ice nucleation on the parameters E_{max} and c in Equation (3.1). The simulations were at 270 K for the six-site model, and at 260 K for TIP4P/Ice. Yes and No indicate whether ice nucleation and growth was observed or not for the given field parameters.

Our observations are summarized in Table 3.3. For $c = 10 \text{ \AA}$, ice nucleation was observed for $E_{\text{max}} = 3.5 \times 10^9 \text{ V/m}$ and higher values for the six-site model, and at $E_{\text{max}} = 2.5 \times 10^9 \text{ V/m}$ and higher values for TIP4P/Ice. For $c = 20 \text{ \AA}$, ice nucleation occurred for $E_{\text{max}} = 1.5 \times 10^9$

3.3. Results and Discussion

V/m and higher values for both water models. Note that we have not fine tuned the nucleation thresholds by examining a finer grid in E_{\max} , so the limiting values might be a little lower than those quoted above. Also, the low field limits obtained for $c = 20 \text{ \AA}$ are very close to those we find for the electrofreezing of bulk water, where all molecules experience the field. Thus, we would not expect the field strength threshold for ice nucleation to be significantly reduced by allowing the field to act further than 20 \AA from the surface.

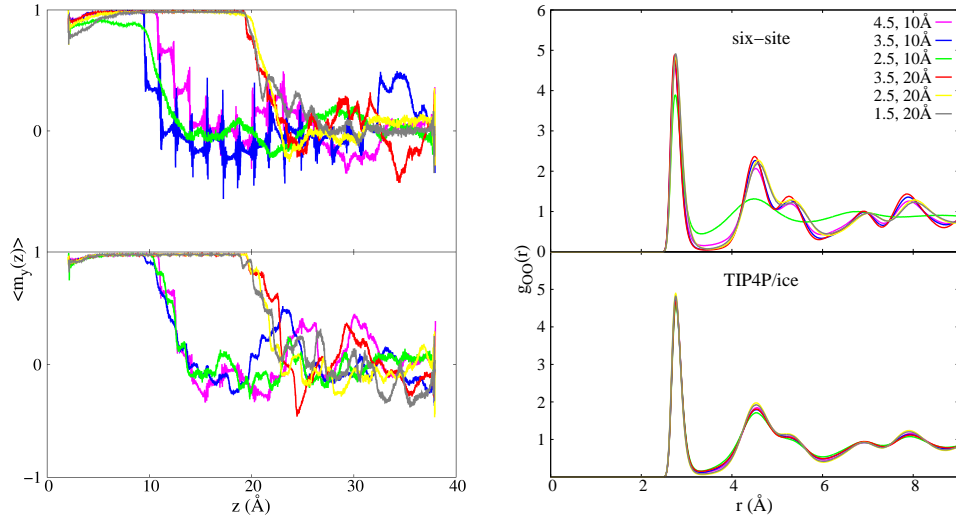


Figure 3.10: Dipole order parameter profiles and oxygen-oxygen radial distribution functions at different values of E_{\max} and c for both the six-site and TIP4P/Ice models. The values of $E_{\max} \times 10^{-9} \text{ V/m}$ and of c are indicated in the figure.

Radial distribution functions and corresponding polarization plots for different fields are shown in Fig. 3.10. From the radial distribution functions

3.3. Results and Discussion

we see that the ice structures are practically identical for the different fields. This is not surprising, but it does serve to emphasize that the field acts to nucleate ice, and does not appear to strongly influence the structure obtained. The polarization plots show that in systems where ice nucleation occurs, the dipole order parameter in the field region is near one. Consider for example the $c = 10 \text{ \AA}$, $E_{\text{max}} = 2.5 \times 10^9 \text{ V/m}$ case. For these parameters the dipole order parameter is ~ 0.9 for the six-site model where ice nucleation is not observed, and is much closer to 1 for the TIP4P/Ice system, where nucleation does occur. The reason for the increased dipolar order found for TIP4P/Ice is likely due to the fact that this model has a larger dipole moment (2.43 D) than the six-site model (1.89 D), and hence interacts more strongly with the field. Given this observation, a properly polarizable water model, which is expected [105] to have a mean liquid-state dipole moment in the range 2.6 - 3.0 D, could be expected to show ice nucleation at fields lower than those we find to be effective for TIP4P/Ice. This is also likely to be true for real water.

We see from Fig. 3.10, that for the same E_{max} , the dipole order can be stronger for $c = 20 \text{ \AA}$ than for $c = 10 \text{ \AA}$. This is particularly evident for the six-site model with $E_{\text{max}} = 2.5 \times 10^9 \text{ V/m}$. The reason for this is that for $c = 20 \text{ \AA}$ more water molecules experience the field, and their collective interactions enhance the field's influence increasing the polarization. Collective interactions also explain why the dipole order parameter shows a drop very near the surface, where the water molecules have fewer adjacent neighbours with which to interact.

3.4 Summary and Conclusions

We have examined field-induced ice nucleation for a model system where only water molecules very near a surface experience an external field. Two water models, several sets of field parameters, and a range of temperatures are considered. Additionally, we carefully check that system size and/or cell dimensions do not have a significant influence on the simulation results. Our main findings are as follows.

Field-induced ice nucleation and growth readily occurs for both the six-site and TIP4P/Ice water models. Although there are some quantitative differences due to differing model parameters and physical properties, the qualitative behaviour of both models is very similar. Also, our qualitative observations do not exhibit any significant dependence on the system size, or on the dimensions of the cell employed. The time required for ice to nucleate after application of the field varies from a few nanoseconds to a few tens of nanoseconds for trial runs that differ only in their initial conditions. We demonstrate that although cubic ice is nucleated and grows in all cases, fixing the cell geometry and the field direction does not fix the crystal axes of the ice formed. The axes of the ice crystals formed in different trial runs can take on different orientations in identical simulation cells.

Simulations were carried out for a range of temperatures with fixed field parameters, and ice nucleation and growth was observed over the temperature range 250-280 K for the six-site model, and over 245-270 K for TIP4P/Ice. Recalling that the normal freezing points are estimated to be ~ 289 for the six-site model, and ~ 270 for TIP4P/Ice, these temperature

3.4. Summary and Conclusions

ranges are physically reasonable. The TIP4P/Ice model does appear to experience ice nucleation closer to its freezing point than the six-site case, but given the uncertainties in the freezing point estimates, and our five degree temperature grid, too much significance should not be attached to this apparent difference. On the low temperature side, both models become very glassy and ice nucleation is not observed on simulation time scales.

In our model, the electric field is governed by two, physically important parameters. These are the field strength E_{\max} and the parameter c , which is essentially the distance from the surface where the field strength remains significant. We find that if $c = 10 \text{ \AA}$, then the six-site and TIP4P/Ice models show ice nucleation for $E_{\max} \gtrsim 3.5 \times 10^9 \text{ V/m}$, and $E_{\max} \gtrsim 2.5 \times 10^9 \text{ V/m}$, respectively. If $c = 20 \text{ \AA}$, both models shows ice nucleation if $E_{\max} \gtrsim 1.5 \times 10^9 \text{ V/m}$. Ice nucleation is only observed if the dipole order parameter in the surface region is very nearly one. The dipole moment of TIP4P/Ice (2.43 D) is significantly larger than that of the six-site model (1.89 D), and hence the TIP4P/Ice molecules interact more strongly with the field. This likely explains the stronger polarization that allows ice to nucleate at a lower field strength for TIP4P/Ice when $c = 10 \text{ \AA}$. With $c = 20 \text{ \AA}$, more molecules experience the field and their collective interaction leads to stronger polarization, and ice nucleates at a lower field strength for both models. We note that increasing c further will not enhance ice nucleation. This is because the minimum field strength for which we observe bulk electrofreezing (all molecules experience the field) is essentially the value we obtain for $c = 20 \text{ \AA}$. Also, it is worth remarking that a properly polarizable water model (and perhaps real water) would likely nucleate ice at

3.4. Summary and Conclusions

still lower field strengths for $c = 10 \text{ \AA}$. The mean liquid-state dipole moment of polarizable water models (2.6-3.0 D) is larger than that of TIP4P/Ice, and hence we would expect stronger polarization near the surface, and ice nucleation at a lower field strength.

Finally, we note that in our model system the ice formed is cubic, just as it is in electrofrozen bulk systems. The only difference is that the bulk samples are globally ferroelectric, whereas in the present case only the surface layer that directly experiences the field is ferroelectric, the ice that grows beyond this region is dipole disordered. This raises questions as to why cubic ice rather than the more stable hexagonal form grows in our simulations. One obvious factor is that the field-induced, ferroelectric ice layer formed near the surface has a cubic structure, and we might expect this to give a kinetic bias to the structure of the dipole disordered ice that grows beyond the surface layer. However, recently reported experimental and simulations studies suggest that the explanation might be more complex. Cubic ice that slowly converts to hexagonal ice has been reported in nucleation experiments [103], and it has since been convincingly argued [106] that ice nucleated in supercooled water actually consists of both cubic and hexagonal forms in randomly stacked layers. Similar mixed cubic/hexagonal structures have been observed in MD simulations employing the mW model [107–109]. However, only cubic ice was found [110] in metadynamics simulations using TIP4P water, so the simulation results may have some dependence on the model and/or the conditions employed. We note that it has long been suggested that cubic ice might have a special role in ice nucleation [111], and it has been argued that cubic ice may be more stable than hexagonal

3.4. *Summary and Conclusions*

ice in finite systems such as thin films [104]. In any case, both water models we consider form cubic ice in the field nucleation geometry employed. We speculate that as the cubic ice layers extend further and further from the surface into the bulk, the structure would eventually convert to the hexagonal form. However, it is possible that both the sample size and the time required to observe such behaviour lie well outside what is presently possible with computer simulations. The issue of cubic versus hexagonal ice is further discussed in the following chapter.

Chapter 4

Ice Nucleation by Electric Surface Fields of Varying Range and Geometry

4.1 Introduction

As discussed in previous chapters, heterogeneous ice nucleation is an important process in many natural settings [3, 11, 24, 100]. An important example from atmospheric science is ice clouds formation, facilitated by aerosol particles, which significantly influence climate [4, 5, 7]. There are many other examples of atmospheric [112] and biological [24, 100] systems, where heterogeneous ice nucleation is an important factor. Despite the importance of heterogeneous ice nucleation, it is fair to say that the microscopic mechanism(s) of nucleation, and the particular features required of good ice nuclei remain poorly understood. It is often argued [7] that a good crystallographic match with the ice lattice, as is the case for some ice nucleating materials, is an important feature, but recent computer simulation studies of model systems have been unable to provide any evidence in favour of

this explanation [21, 64–67]. Moreover, since very varied substances ranging from mineral particles to proteins and bacteria can nucleate ice, a general explanation based on matching crystal structures seems unlikely.

It is difficult to obtain direct experimental information about early stage ice nucleation, due at least in part to the small length scales and short times involved. An additional complication is that the particles which are important ice nuclei in realistic situations, such as the mineral particles relevant to atmospheric science, nearly always have very rough surfaces with a variety of structural features that could possibly serve as “active sites” for ice nucleation [68]. From this perspective, controlled experiments with particles that are microscopically well characterized would likely provide valuable insight, but at present there are few if any such studies. Given this situation, computer simulations of model systems offer another route to information and understanding at the molecular level, which is rapidly becoming more viable as computational power increases.

On the simulation side, there have been a number of interesting studies of homogeneous ice nucleation employing both direct molecular dynamics (MD) methods [107, 113], and other indirect “biased sampling” techniques [99, 110, 114]. For some questions biased sampling methods are preferred, providing an efficient means of sampling rare events that may not be accessible by any other simulation approach. Biased sampling methods are excellent for obtaining thermodynamic properties such as free energy differences that are independent of path, but because they require the *a priori* selection of a “reaction coordinate”, such methods may reveal little about the actual nucleation process. Direct MD simulation has the advantage

that ice nucleation and growth can follow the physically relevant pathway, but the disadvantage that for realistic atomistic water models homogeneous ice nucleation events are too rare for reliable study on currently feasible simulation timescales. Direct MD simulations have proven extremely useful for the more coarse grained monatomic water (mW) model, developed and extensively studied by Molinero and coworkers [75]. A great deal of insight into the nature of homogeneous ice nucleation has been obtained from this work [107, 113].

A different situation might be expected for heterogeneous ice nucleation, where a good ice nucleation catalyst could dramatically speed up the process such that direct MD studies of ice nucleation and growth become possible for realistic water models. Perhaps the most favourable example currently known is ice nucleation by external electric fields that can apply over the entire sample [47, 61, 62], or merely over a thin region near a surface [115, 116]. The case where the field applies throughout the sample is more properly termed electrofreezing because in that case the field influences the freezing point itself, whereas a local surface field acts only as a catalyst that facilitates the nucleation process. In such simulations, ice nucleation induced by an applied field is a robust phenomenon not strongly dependent on simulation variables, such as sample size. We note that while there have been experimental reports of field influenced ice nucleation [55–57], a definitive demonstration with well defined and measured fields is still lacking. One inhibiting problem is that the fields required (at least on simulation timescales) are orders of magnitude larger than those that cause dielectric breakdown in macroscopic water samples, and it is difficult to create con-

trolled fields on the small length scales required to avoid breakdown [44].

Direct MD simulations employing atomistic water models have also been used by Jungwirth and coworkers to investigate ice nucleation at free water surfaces [70, 117], as well as at water-pentanol and water-pentanoic acid interfaces [118]. For rather narrow simulation cells (~ 1.35 nm) repeated periodically in directions perpendicular to the interface, ice nucleation is observed in these systems, but apparently freezing is not observed for wider periodically repeated simulation cells [118]. Recently, somewhat similar studies of water-kaolinite interfaces were reported by Cox *et al.* [21], where they observe an interesting influence of kaolinite on ice nucleation. However, as clearly noted by the authors, the observations again strongly depend on sample size, so the status and significance of the results remains somewhat unclear.

In this chapter we further explore ice nucleation by surface fields. In earlier work [115, 116] discussed in Chapter 3, we considered ice nucleation by fields that were finite perpendicular to the surface, but acted over the entire surface area. Here we examine fields that act only over surface “bands” of different size and geometry. We show that field bands of varied shape can function as very effective ice nuclei, provided that a certain size threshold is exceeded. By varying the field bands, we also learn more about the mechanism of ice nucleation and growth. One important observation consistent for all systems considered is that essentially all ice growth occurs at (111) planes of cubic ice. By varying the field geometry and proportion of the surface it covers, we gain insight into how field nucleation influences the mix of hexagonal and cubic ice observed under different simulation

conditions.

The remainder of this chapter is divided into three parts. The models and simulation method are described in Section 4.2, results are given and discussed in Section 4.3, and our conclusions are summarized in Section 4.4.

4.2 Models and Methods

The so-called six-site [72] and TIP4P/Ice [71] water models are both convenient for simulation studies of ice and freezing. In earlier investigations [115, 116] of field-induced ice nucleation discussed in Chapter 3, we have shown that the physical behaviour of both models is qualitatively similar. Therefore, in the present chapter we report results only for the six-site model, but we have verified that no significant differences occur in the behaviour of TIP4P/Ice. The details of the six-site water model is described in Section 2.1, and the normal freezing point of the six-site model is estimated [101] to be ~ 289 K.

As in our previous work [115, 116], the water molecules are confined between two parallel surfaces as sketched in Fig. 2.2 in Chapter 2. The surfaces are separated by the distance L_z , which together with L_x and L_y defines the dimensions of the rectangular simulation cell. The system is periodically infinite in the x and y directions. The surface-water interactions are given in Equation (2.1) by Chapter 2. These parameters correspond to a “neutral” surface, which imposes little order in the neighbouring water molecules.

In our slab geometry (Fig. 2.3 in Chapter 2), water molecules near the

left-hand surface experience an electric field directed along the x -axis that is of finite range in z , and possibly in y . The spatially varying field is given by

$$\mathbf{E}(y, z) = E_{\max} \left(\frac{1}{1 + f(y, z)} \right) \hat{\mathbf{x}}, \quad (4.1)$$

where $f(y, z)$ is very small in the region of the field, but grows exponentially fast beyond the designated boundary. Note that in this chapter the field is taken to be in the x direction, and in Chapter 2 (Fig. 2.3) the field is illustrated in y direction. Equation (4.1) gives a field which is nearly constant at E_{\max} within a defined volume, but decays rapidly to zero outside this volume. We consider field bands (finite range in z and y) with cross sectional areas that are rectangular, triangular, and semicircular in shape, as shown in Fig. 2.3. Appropriate choices of $f(y, z)$ control the shape and extent of the field bands.

In previous simulations [115, 116] (Chapter 3), we employed our own MD program, but in the present calculations we use the LAMMPS MD package [88], which is a more efficient parallel code, allowing us to simulate larger systems for longer times. Periodic boundary conditions (PBC) are formally employed in all three directions, but to accommodate the slab geometry empty regions are placed outside the confining surfaces located on the z axis [76]. The Particle-Particle Particle-Mesh (PPPM) method [90] is used to take account of the long-range Coulombic interactions. The short-range, water-water and water-wall interactions are truncated at 0.8 nm. All simulations are performed in the NVT ensemble. The equations of motion

are integrated applying the velocity Verlet algorithm [77] (with a 0.75 fs timestep) for the rigid six-site water model. The Nosé-Hoover thermostat [93, 94] with a relaxation time of 0.037 ps is used to control the temperature.

In all simulations, liquid water is first equilibrated at 350 K, which is well above the freezing point (~ 289 K) of the six-site water model. The samples are then cooled to 270 K, and relaxed at that temperature for 300 ps before the field is switched on. This ensures that all samples are initially in the same relaxed liquid state before being exposed to the field. The simulations were then continued until ice nucleation and growth was sufficiently well established for our analysis. The run times (after application of the field) required for this ranged from 62 to 130 ns, depending on the system, and the particular simulation run.

In the present simulations, the applied field has $E_{\max} = 3.0 \times 10^9$ V/m. This is smaller than the value (5.0×10^9 V/m) used in previous work [47, 115, 116], but is sufficiently large to nucleate ice in all system geometries considered here. We note that in our earlier simulations [115, 116] (Chapter 3), the field experienced by all charges within the same molecule was kept strictly constant. This ensured that the field could impose a rotational torque, but no translational force on a molecule. It is difficult to apply this constraint in the LAMMPS code, so in the present simulations the field can vary a little across a molecule. However, by comparing with strictly constant field results for some test cases, we determine that this has no significant influence on ice nucleation.

We use the CHILL algorithm developed by Moore *et al.* [75] to analyze the ice structure. This algorithm allows one to classify water molecules

as belonging to cubic, hexagonal, and “intermediate” ice structures, or to liquid water. This algorithm is discussed in details in Chapter 2. Here we are interested in identifying regions of cubic and hexagonal ice, and therefore in the analysis given below we classify water molecules as cubic, hexagonal, or liquid, with both liquid and intermediate molecules included in the “liquid” category.

4.3 Results and Discussion

4.3.1 Full Surface Field

Before discussing results for fields acting over different portions of the surface area, it is useful to briefly revisit the full surface field case considered earlier [115, 116] (Chapter 3). In that model, a parallel field acts over the entire surface area (periodic in x and y), but decays rapidly with distance from the surface z . This situation corresponds to Equation (4.1) with $f(y, z) = f(z) = e^{a(z-c)}$, where the parameters a and c control the decay of the field with distance from the surface. Previously, we showed that a thin surface field that decays essentially to zero at 0.1 nm from the surface nucleates ice very effectively. Ferroelectric cubic ice rapidly forms a surface layer, and unpolarized ice grows outward from this nucleus. However, in our earlier work we did not determine the mechanism of ice growth.

Here, we address this question by carefully observing the pattern of ice growth in a number of simulations (20 in all) employing larger systems (≥ 2400 water molecules) with different initial conditions, and in some examples different cell dimensions. The same growth mechanism is observed in all

4.3. Results and Discussion

simulations, and is illustrated by the configurational snapshots given in Fig. 4.1. For the particular case shown, $L_x = L_y = 3.06$ nm, $L_z = 8.5$ nm, and the field parameters are $a = 0.1$ nm⁻¹, $c = 0.1$ nm, and $E_{\max} = 3.0 \times 10^9$ Vm⁻¹. Note that in order to give a clearer picture of the behaviour of the periodic system, Fig. 4.1 includes the central simulation cell (outlined in black), together with the above and below periodic images. Further note, that the perspective shown is directly into the (110) plane of cubic ice.

Our observations illustrated in Fig. 4.1 are as follows. Initially (~ 10 ns), an ice sheet ~ 0.1 nm thick forms in the field region. However, beyond this sheet the ice does not grow layer by layer parallel to the wall. Rather, the growing ice layers can take different orientations, which in general are not parallel to the surface. Based on careful examination of different simulations, we determine that ice growth occurs at the (111) plane of cubic ice. This is the case in all of our simulations, independent of the particular orientation taken by the ice crystal with respect to the simulation cell. This is especially easy to see in the snapshots shown in Fig. 4.1, where the dashed green lines (stage 1) mark the ice-water interface at the (111) crystal plane. Ice grows layer by layer at this interface. We remark that Takahashi [111] has previously pointed out that the (111) plane of cubic ice gives the most favourable ice-water interfacial energy, which is consistent with our empirical observation. Also, as described below, the (111) plane growth mechanism is observed in all of our simulations including those where nucleation is induced with fields of different geometry covering different surface areas.

Another aspect of our earlier simulations that requires explanation is the fact that we observed only cubic ice in our samples [115, 116], whereas based

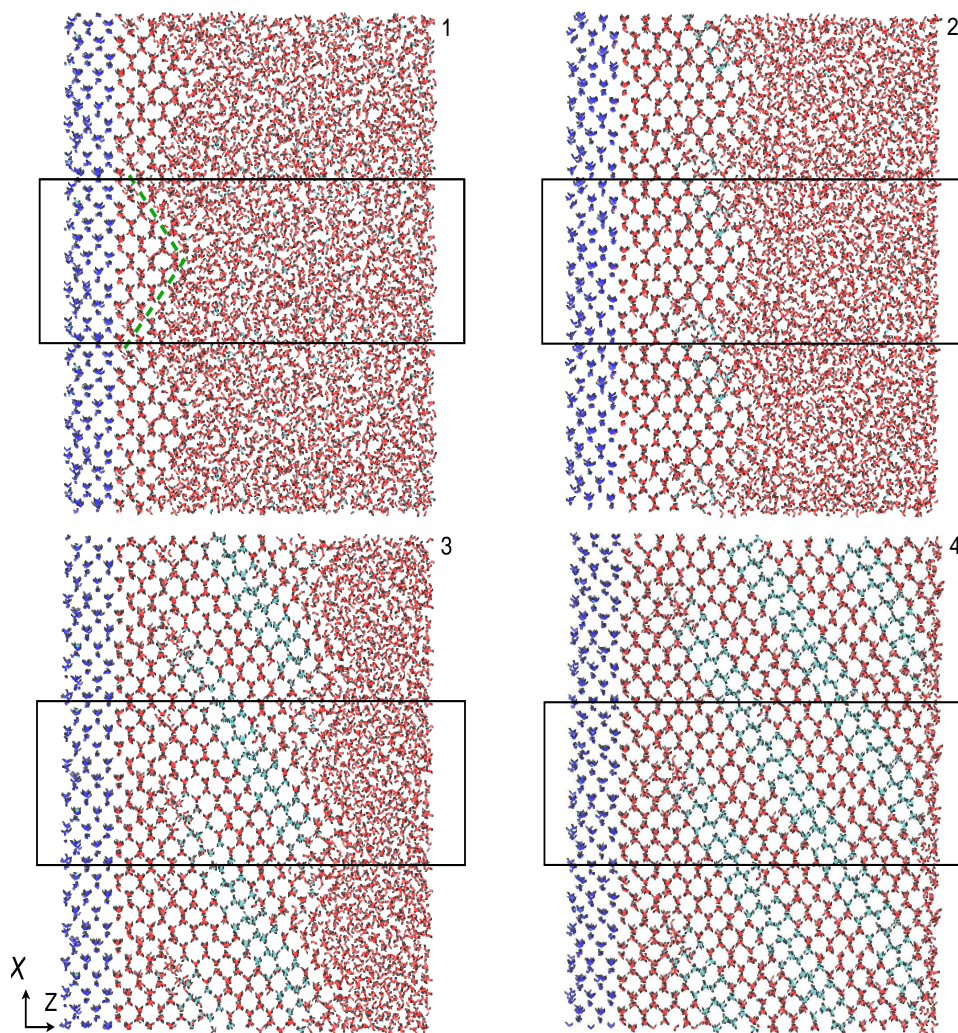


Figure 4.1: Configurational snapshots showing ice nucleation and growth for a 2400 molecule system with a full surface field. The snapshots show the (110) plane of cubic ice at 20 ns (stage 1), 50 ns (stage 2), 60 ns (stage 3), and 70 ns (stage 4). The water oxygen atoms in the field region are dark blue, those associated with cubic ice or liquid are red, and those in hexagonal ice layers are light blue. All hydrogen atoms are black. The rectangles outline the central cell. The dashed green lines shown in stage 1 indicate growth at (111) planes of cubic ice.

on other simulation [73, 75, 99, 119] and experimental [103, 106] studies of ice growth under similar conditions, some mixture of cubic and hexagonal ice layers is expected. As discussed by others, cubic ice (ice Ic) is only marginally less stable than hexagonal ice (ice Ih), and, moreover, the basal plane of hexagonal ice and the (111) plane of cubic ice are identical [73, 74]. Therefore, cubic and hexagonal ice can be “joined” at this surface with only a small unfavourable interfacial energy. Despite this, and in contrast with other simulations of ice growth [73, 99], in over 40 simulations of ice nucleation by full surface fields, we observed a hexagonal ice layer only once. In all other cases only cubic ice was formed. However, in simulations where the field acts only over a portion of the surface area (see discussion below) we routinely observe both cubic and hexagonal ice layers in the growing crystal.

At first sight this discrepancy appears rather surprising, but we now believe that it is an artifact of finite system size and PBC. The single example where we do observe a layer of hexagonal ice under full surface field conditions is shown in Fig. 4.1 (see stages 3 and 4). We note that under PBC all ice layers must terminate in the field region near the surface. This is an unfavourable situation for hexagonal ice because near the surface the field strongly favours cubic ice. We note that in the example shown in Fig. 4.1 the hexagonal ice layer converts to cubic near the surface region giving rise to a structural defect. It seems highly likely that the mismatch of hexagonal ice with the cubic surface layer strongly inhibits the formation of hexagonal layers in our finite periodic samples. In systems with partial surface fields, the field does not extend over the entire surface area, and

hexagonal layers can continue unaltered contacting the surface outside the field region, which is in fact what we observe (see below).

4.3.2 Partial Surface Fields

As noted above, the main purpose of the present chapter is to determine if, and to what extent, ice nucleation is influenced by the shape and size of the surface field. To that end, we have performed a number of simulations where the field acts in rectangular, triangular, and semicircular bands as illustrated in Fig. 2.3. Details of the simulations carried out are summarized in Table 4.1. In simulations 1-10 (Table 4.1), 3900 molecules were used with $L_x = 2.67$ nm, $L_y = 10$ nm, and $L_z = 5$ nm, giving a density of ~ 0.96 g/cm³. Simulation 11 involves a larger system (6000 molecules) and was carried out to investigate any influence of the surface-surface separation. For this case, the L_x and L_y dimensions (2.68 and 10 nm, respectively) are at or near those of the smaller samples, but $L_z = 7$ nm, again giving a density ~ 0.96 g/cm³. Additional tests were carried out for systems with L_y increased to 15 nm (5760 water molecules) to ensure that we are indeed seeing the effect of a single field band, uninfluenced by periodic repetition in the y dimension. The details of these results are not given because they are essentially the same as those obtained with $L_y = 10$ nm, providing evidence that our observations are not significantly influenced by the periodicity in y .

The dimensions (y, z) of the three field geometries considered are given in the table. For rectangles, (y, z) represents (length, width), for triangles (base, height), and for semicircles the radii are given. The functions $f(y, z)$

4.3. Results and Discussion

simulation	time (ns)	cubic	hexagonal	liquid
1, rectangular (0.65, 0.15)	62	2354	609	937
2, rectangular (0.55, 0.15)	90	2236	588	1076
3, rectangular (0.45, 0.15)	140	1222	28	2650
4, rectangular (0.45, 0.15)	90	2941	140	819
5, rectangular (0.35, 0.15)	95	2087	820	993
6, rectangular (0.35, 0.15)	130	2486	488	926
7, triangular (0.75, 0.19)	70	2093	841	966
8, triangular (0.70, 0.18)	75	1905	881	1114
9, semicircular (0.25)	90	2081	943	876
10, semicircular (0.23)	95	2139	783	978
11, rectangular (0.45, 0.15)	85	3656	1072	1272

Table 4.1: Summary of simulations carried out with partial surface fields. For simulations 1-10, L_x , L_y , and L_z are 2.67, 10, and 5 nm, respectively, for simulation 11, 2.68, 10, and 7 nm, respectively. In all simulations the density is $\sim 0.96 \text{ g/cm}^3$. The numbers given in brackets in column one are the (y, z) dimensions (in nm) of the field bands (Fig. 2.3). The times given in this table are the lengths of the simulations. For rectangles these are the length and width, for triangles the base and height, and for semicircles the radius. The numbers of cubic, hexagonal, and liquid water molecules in the configuration at the final timestep are given in the last three columns.

used in Equation (4.1) are selected such that the field strengths become negligible (i.e., much lower than that needed to nucleate ice) outside of the field dimensions given in Table 4.1.

From the results summarized in Table 4.1, we see immediately that field bands of all three shapes can serve as effective ice nuclei. Most trials were performed with the rectangular geometry, and within our simulation times ice nucleation and growth was observed for $(y, z) \equiv (0.35 \text{ nm}, 0.15 \text{ nm})$ (5 out of 12 trials showed ice nucleation within 50 ns), but not for smaller sizes. Simulations for $(y, z) \equiv (0.29 \text{ nm}, 0.15 \text{ nm})$ show fluctuating ice-liquid structure in the field region, but ice growth beyond the field region was

4.3. Results and Discussion

not observed. It appears that surface field bands $\lesssim 0.35$ nm wide are not sufficient to generate ice nuclei that live long enough to grow.

Configurational snapshots showing the pattern of ice nucleation and growth for rectangular field bands are shown in Fig. 4.2 (simulation 2 in Table 4.1) and Fig. 4.3 (simulation 11 in Table 4.1), and for a semicircular field band in Fig. 4.4 (simulation 10 in Table 4.1). For triangular field bands configurational snapshots (not shown) indicate a pattern of ice nucleation and growth much like that of the other geometries. By and large, the ice nucleation and growth process for field bands is similar to that observed for full surface fields, and does not show any strong dependence on the shape and size of the field band, provided that it is over a size “threshold”, as noted above. Specifically, a block of polarized cubic ice nucleates in the region of the field band, and unpolarized ice then grows into the bulk. Ice growth at the (111) plane can be easily seen for the rectangular example shown in Fig. 4.2 (note the growth regions marked with dashed green lines in the 15 ns snapshot).

Despite the similarities, systems with field bands differ in one significant way from the full surface field case. As noted above, with a full surface field it is very unusual to observe any hexagonal ice layers mixed in with the cubic structure. This is surprising because cubic and hexagonal ice layers can be joined with very little interfacial energy penalty, and more importantly mixed ice structures are observed in other simulation and experimental studies of ice nucleation and growth. As discussed above, we suspect that the near absence of hexagonal layers in our full surface field simulations is due to finite system size and PBC. Under PBC ice layers terminate in the

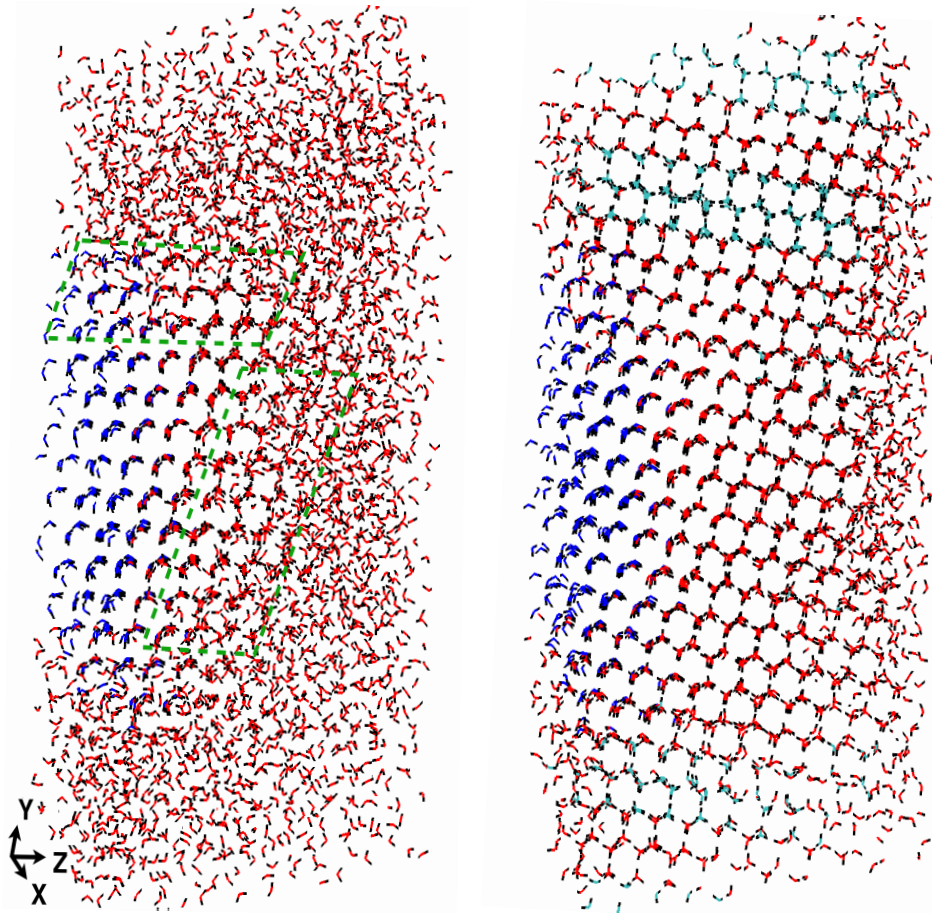


Figure 4.2: Configurational snapshots showing ice nucleation and growth for a rectangular field band (simulation 2 of Table 4.1). From left to right the snapshots correspond to 15, and 90 ns. The atoms are coloured as in Fig. 4.1. The dashed green lines in the snapshot at 15 ns indicate ice growth at (111) faces of cubic ice. Note that the hexagonal ice layers meet the surface outside the field region.

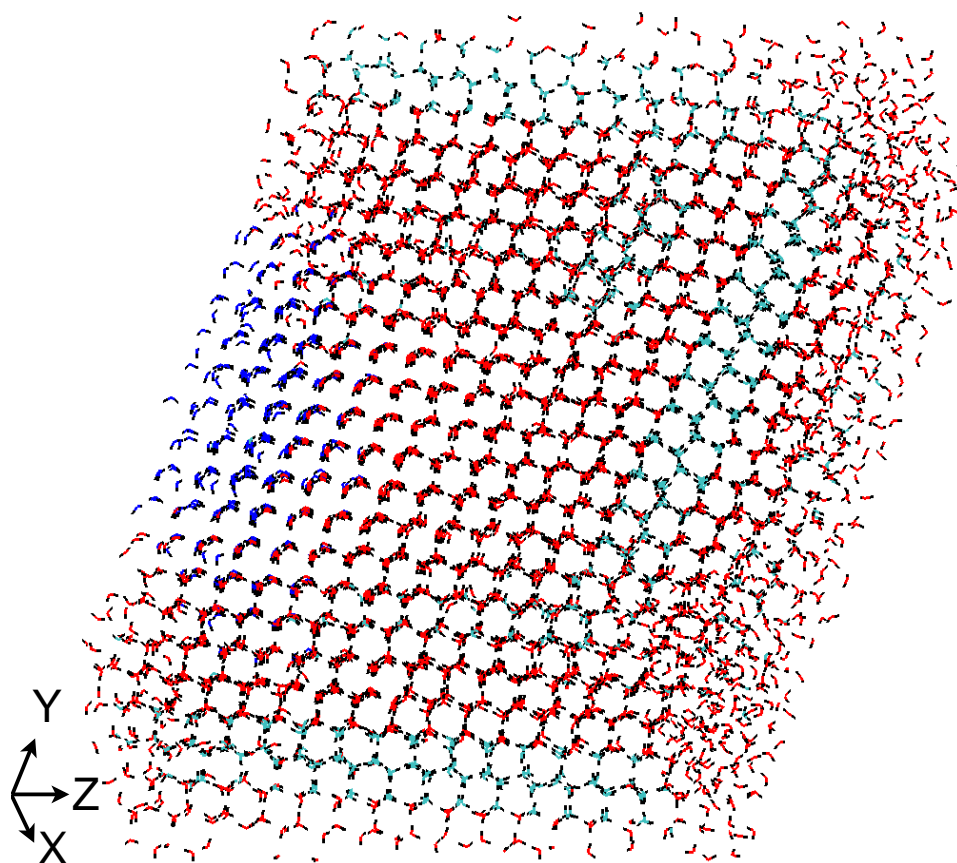


Figure 4.3: Configurational snapshot (at 85 ns) showing ice nucleated by a rectangular field band in a larger system (simulation 11 of Table 4.1). The atoms are coloured as in Fig. 4.1. Note that in the larger system hexagonal ice layers can form parallel to the surface.

polarized surface ice layer, which strongly disfavours the hexagonal form.

The simulations with field bands provide strong evidence that this explanation is correct. In nearly all simulations with field bands (Table 4.1) we find significant numbers of hexagonal ice molecules, and hexagonal ice layers can be easily identified in the configurational snapshots (Figs. 4.2, 4.3, and 4.4). Moreover, we note that the hexagonal ice layers are located in the simulation cell such as to avoid contact with the band of polarized cubic ice. For the smaller systems (Figs. 4.2 and 4.4), the hexagonal layers tend to be oriented across the cell from surface to surface, contacting the left-hand surface outside the field region. For the larger system (Fig. 4.3), the hexagonal ice layers can take other orientations in the simulation cell, as we would expect in a truly infinite sample. These observations confirm our suspicion that it is the polarized surface ice layer which acts against the formation of hexagonal ice in our full surface field simulations. Of course with sufficiently large samples, the surface mismatch and associated defects will become thermodynamically unimportant, and we would expect hexagonal ice structures even with full surface field nucleation.

We note also that in our simulations the ratio of hexagonal to cubic ice is usually less than the 1:2 ratio reported by Moore *et al.* [75] (see numbers given in Table 4.1). This difference is explained by the fact that in our simulations all ice formed in the field band is cubic, and, furthermore, the block of cubic ice at the surface can inhibit hexagonal ice formation in other parts of the simulation cell.

One other point worth mentioning is that the amount of hexagonal ice formed can vary considerably for simulations that differ only in their initial

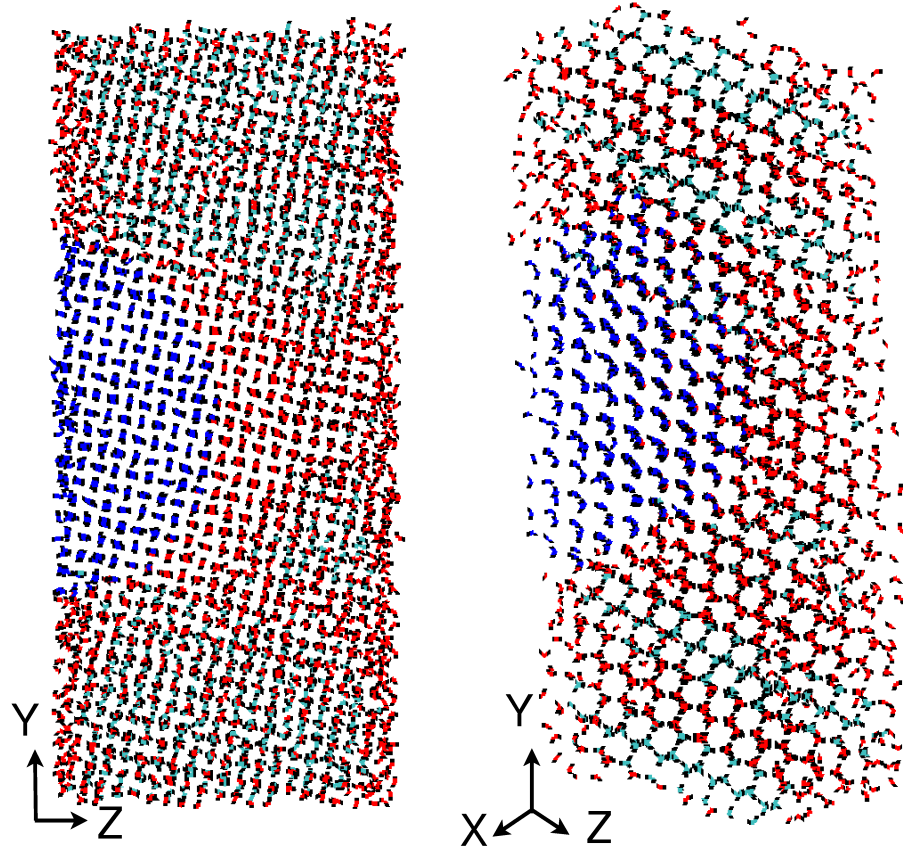


Figure 4.4: Configurational snapshots (at 90 ns) of ice nucleated with a semicircular field band (simulation 10 of Table 4.1). The (001) (left panel) and (110) (right panel) planes of cubic ice are shown. The atoms are coloured as in Fig. 4.1. Note that the hexagonal ice layers meet the surface outside the field region.

conditions. We have noticed that in simulations where the ice grows quickly, rapidly filling the cell, there tends to be less hexagonal ice than for cases where the ice grows more slowly. This might indicate that cubic ice has some kinetic advantage over hexagonal in the growth process. We also note that once the simulation cell has completely frozen, the ratio of hexagonal to cubic ice shows no change on the timescale of our simulations.

4.4 Summary and Conclusions

In this chapter we use MD simulations to examine ice nucleation by partial surface fields. Results are reported for the six-site water model [72] undercooled by ~ 20 K. For comparison some simulations were also carried out with the TIP4P/ice water model [71], and the results obtained were not significantly different. We show that field bands exceeding a minimum size ($\gtrsim 0.15$ nm thick, and $\gtrsim 0.35$ nm wide for the rectangular case) catalyze ice nucleation just as efficiently as full surface fields. Additionally, the shape of the field band does not appear to be particularly significant, with rectangular, triangular, and semicircular cross sectional areas giving qualitatively similar results. These observations further support the suggestion that local electric fields might be a significant factor in some ice nuclei.

Simulations with fields of different geometry and dimension also teach us more about the ice nucleation and growth process. For all systems considered, based on careful observation of the pattern of crystal growth, we determine that nearly all growth occurs at (111) planes of cubic ice. This is despite the fact that the crystal axes of the growing ice can take different

4.4. *Summary and Conclusions*

orientations in the simulation cell, varying with different initial conditions. Our simulations clearly show that growth at the (111) plane of cubic ice is strongly favoured, consistent with a suggestion of Takahashi [111] based on consideration of interfacial energies.

It is also worth remarking that with partial surface fields we nearly always observe hexagonal ice layers mixed into the cubic structure, consistent with other simulations [73, 75, 99, 119], and with experiment [103, 106]. This contrasts with the full surface field case, where hexagonal ice is almost never observed in our simulations [115, 116]. We show that in all likelihood this difference is a simulation artifact related to finite system size and periodic boundary conditions.

Chapter 5

Understanding

Electrofreezing in Water

Simulations

5.1 Introduction

Pure water freezes when an ice cluster grows faster than it melts. Sanz *et al.* [120] estimate that it would take more than 13 billion years to nucleate ice in 10^{18} tonnes of water, at -20°C . Therefore, a nucleating agent must usually be present for water to freeze. Diverse materials nucleate ice [1, 3, 10, 20, 121], but the properties responsible for ice nucleation remain unknown, or at best poorly understood.

As we demonstrated in earlier chapters, partial electric fields can induce ice nucleation efficiently. Model water freezes rapidly (within nanoseconds) when exposed to a uniform electric field on the order of 1 V/nm (i.e., \times V/m are used elsewhere), as demonstrated by molecular dynamics simulations [47, 58, 62]. Experiments also showed that local electric fields are a possible significant feature of many ice-nucleating materials [55–57]. Real

water undergoes dielectric breakdown if exposed to such strong, uniform fields, making it impossible to confirm simulation results experimentally [46]. However, real water can withstand large local fields produced by ions or charge groups, and simulations indicate that local fields can also nucleate ice [115]. Some experimental studies suggest that weaker electric fields promote freezing [55, 57, 122, 123], while others find that particular fields can inhibit freezing [57], or have no effect [44]. Simulations can only probe, at most, microsecond timescales; if weak fields promote freezing, they may require significantly more time to generate ice nuclei.

The factors that enhance freezing in polarized water are unclear. In general, homogeneous freezing occurs when a critical ice nucleus forms in pure bulk water. According to classical nucleation theory, the size of the critical nucleus decreases as either the temperature and/or the solid-liquid surface tension decreases. Assuming classical nucleation theory accurately describes ice nucleation, electric fields may promote freezing by increasing the melting temperature, and/or decreasing the surface tension between ice and water.

In this work, we find that the melting temperature of the six-site water model [101] increases when interacting with a uniform electric field. In presence of a field, polarized cubic ice coexists with polarized liquid water at temperatures well above the normal melting point of the six-site model at zero field. In cubic ice, the water dipoles are essentially perfectly aligned by the electric field, whereas only partial polarization is observed in the coexisting liquid. Thus, favourable interactions with the field help stabilize ice at a higher temperature. Our simulations show that the spatial structure

and tetrahedral order of liquid water change little with partial polarization; however, structural changes do occur as liquid water dipoles approach near perfect alignment with the field. Even when strongly polarized, water can be supercooled to ~ 40 K below the field-dependent melting point, which is comparable with the degree of supercooling commonly observed experimentally at zero field. This indicates that the barrier to homogeneous ice nucleation remains high in the presence of an electric field. Our results suggest that local fields generated by ice-nucleating materials may increase the effective melting temperature of the locally polarized water, thereby reducing the size of the critical nucleus.

The remainder of this chapter is divided into three parts. The methods of simulation and analysis are described in Section 5.2, results are discussed in Section 5.3, and our conclusions are summarized in Section 5.4.

5.2 Simulation and Analysis Method

Molecular dynamics simulations of the six-site water model [72] were performed using the GROMACS 4.5.4 simulation package [87]. As discussed before, the six-site water model has a high melting temperature [101] (~ 289 K) and is designed to study water-ice systems near the melting point. In general, structural and thermodynamic properties of ice and water near the melting point are well reproduced by this water model [72].

As a rigid model, six-site water molecules interact via site-site potentials through both Lennard-Jones (LJ) and Coulombic interactions, as described in Chapter 2. Short-range interactions were truncated at 0.8 or 1.0 nm;

5.2. Simulation and Analysis Method

results were qualitatively insensitive to the truncation length used. The PPPM method was used to calculate long-range electrostatic interactions.

Simulations were performed with $N = 1000, 8000,$ or 32000 water molecules, at constant temperature (T) and under constant pressure (P). Constant temperature was maintained using the Nosé-Hoover thermostat [93, 94] and the Parrinello-Rahman barostat was used to maintain a constant pressure of 1 bar [97, 98]. The equations of motion were integrated using the leap-frog algorithm with a 2 fs time step [96].

Changes in free energy and entropy due to a uniform electric field were calculated using thermodynamic integration. In NPT simulations, the Gibbs free energy difference (ΔG) was obtained through

$$\Delta G = G_{\text{field}} - G_{\text{no field}} = \int_0^1 \left\langle \frac{\partial H(\lambda)}{\partial \lambda} \right\rangle_{\lambda} d\lambda, \quad (5.1)$$

where H is the enthalpy, the angular brackets indicate an ensemble average, and λ controls the strength of the interaction between water molecules and the field. U_{field} is calculated by summing over all charge sites in the system

$$U_{\text{field}}(\lambda) = -\lambda \sum_{i=1}^{5N} q_i(\mathbf{r}_i \cdot \mathbf{E}), \quad (5.2)$$

where \mathbf{E} is the electric field, q_i represents the i -th charge, \mathbf{r}_i is the position vector of charge i , and $5N$ is the total number of charges in the system. In the presence of an electric field, $H=U_{\text{conf}}+U_{\text{field}}+PV$, where U_{conf} is the configurational energy due to water-water interactions, and U_{field} is the energy due to molecular charge sites interacting with the external field.

5.2. Simulation and Analysis Method

Since U_{conf} does not depend on λ , and $\partial(PV)/\partial\lambda$ is two to four orders of magnitude smaller than $\partial U_{\text{field}}/\partial\lambda$, Equation (5.1), can be rephrased as

$$\Delta G \approx \int_0^1 \left\langle \frac{\partial U_{\text{field}}(\lambda)}{\partial \lambda} \right\rangle_{\lambda} d\lambda. \quad (5.3)$$

The entropy change due to interaction with an electric field can then be estimated,

$$S_{\text{field}} - S_{\text{no field}} = \Delta S = (\Delta H - \Delta G)/T, \quad (5.4)$$

where $\Delta H = H_{\text{field}} - H_{\text{no field}}$. This method is valid until water freezes, and the thermodynamic functions decrease discontinuously with ice formation.

The average dipole order parameter, or average polarization, along the direction of the applied field (x) can be calculated through

$$\langle m_x \rangle = \frac{1}{N_{\text{conf}}} \sum_i^{N_{\text{conf}}} \frac{1}{N\mu_w} \sum_{i=1}^N \mu_{x,i}, \quad (5.5)$$

where $N_{\text{conf}} \geq 100$ is the number of independent configurations included in the average, μ_w is the dipole moment of the six-site water model, and $\mu_{x,i}$ is the x -component of the dipole vector of the i -th water molecule.

Polarization might be expected to profoundly affect water's structural properties, and as a consequence, its thermodynamic properties. To understand structural changes that occur in water due to polarization, we compare radial distribution functions, $g(r)$, structure factors, $S(k)$, and the local tetrahedral order parameter [124], q , in polarized and unpolarized water.

5.2. Simulation and Analysis Method

The local tetrahedral order parameter [124]

$$q = 1 - \frac{3}{8} \sum_{i=1}^3 \sum_{j=i+1}^4 \left(\cos(\phi_{ij}) + \frac{1}{3} \right)^2, \quad (5.6)$$

is calculated for each molecule, and q distributions are obtained by averaging over ~ 1000 configurations. In Equation (5.6), ϕ_{ij} is the angle between lines connecting the oxygen atom of a given molecule to the oxygen atoms of its i -th and j -th nearest neighbours.

In liquid water, there are local density fluctuations associated with fluctuations in tetrahedral order, and these are responsible for water's characteristic anomalies [125]. Here we explore whether or not electric fields influence density and structural fluctuations. Following earlier work [125], we classify every water molecule as either high- q (H) or low- q (L) depending on whether its q -value was larger or smaller than the configurational median q -value. We then calculate partial radial distribution functions, $g_{\alpha\beta}(r) = h_{\alpha\beta}(r) + 1$, and structure factors,

$$S_{\alpha\beta}(k) = \delta_{\alpha\beta} + 4\pi\rho\sqrt{x_\alpha x_\beta} \int_0^\infty dr r \frac{\sin(kr)}{k} h_{\alpha\beta}(r), \quad (5.7)$$

where x_α is the mole fraction of “species” α . At $k = 0$, structure factors measure fluctuations: the density-density structure factor, $S_{NN}(k) = S(k)$, measures density fluctuations, the concentration-concentration structure factor,

$$S_{CC}(k) = x_H x_L [x_H S_{HH}(k) + x_L S_{LL}(k) - 2\sqrt{x_H x_L} S_{HL}(k)], \quad (5.8)$$

measures concentration fluctuations, and, the density-concentration struc-

ture factor,

$$S_{NC}(k) = x_H x_L \left[S_{HH}(k) - S_{LL}(k) + 2 \frac{x_H x_L}{\sqrt{x_H x_L}} S_{HL}(k) \right]. \quad (5.9)$$

measures the coupling between density and concentration fluctuations [126].

The presence of ice-like molecules is determined using the CHILL algorithm [75]. The CHILL algorithm distinguishes between cubic, hexagonal, and interfacial ice-like molecules. An ice-like molecule is defined to belong to an ice cluster if it is within 0.33 nm [approximate location of the first minimum in the oxygen-oxygen $g(r)$] of another ice-like molecule.

5.3 Results

5.3.1 Melting Temperature

Previous simulations have demonstrated that upon supercooling water models freeze quickly when interacting with a uniform electric field on the order of 1 V/nm [47, 58, 62]. Consistent with those results, water interacting with a field of 1 V/nm froze spontaneously within 40 ns in all ten independent simulations we ran at 270 K with 8000 molecules. According to classical nucleation theory, ice is more likely to nucleate in deeply supercooled water because the critical nucleus is smaller. If electric fields increase water's melting temperature (T_M), applying a field would increase the degree of supercooling, $\Delta T_S = T_M - T$, at a given temperature, and explain the rapid freezing observed.

There are several methods commonly used to estimate melting temper-

5.3. Results

atures from molecular dynamics simulations [72, 101, 127]. In the direct coexistence method [72, 101, 127], NPT simulations are performed with liquid and solid phases in contact and the melting temperature is determined by finding the lowest temperature at which the solid phase melts. In most cases, the initial interface is constructed, rather than spontaneously generated in a low-temperature simulation. Using the direct coexistence method, Abascal *et al.* [101] found melting temperatures of 287 and 289 K for the six-site water model, with 865 and 1536 molecules, respectively.

Field magnitude (V/nm)	T_M (K) $N = 8000$	ΔS_{fus} (J/mol K)	$\langle m_x \rangle$ (L) at T_M	$\langle m_x \rangle$ (S) at T_M
0.0	289(Ref. [101])	24(Ref. [72]) 27	0.00	0.00
0.8	307.8 ± 2.4	33	0.65	0.98
1.0	313.5 ± 2.4	33	0.71	0.98
1.5	325.2 ± 3.3	32	0.79	0.98
2.0	333.2 ± 2.9	32	0.83	0.98

Table 5.1: Melting temperature estimates for different fields obtained from simulations with 8000 molecules. Estimates of ΔS_{fus} are obtained from NPT simulations with 1000 molecules. The last two columns are the average polarization for liquid and solid systems. L and S stand for liquid and solid respectively.

We use the direct coexistence method to estimate the melting temperature of water interacting with an electric field. However, instead of placing liquid and constructed solid phases in contact, we simply take “half-frozen” configurations from simulations with a field of 1 V/nm at 270 K, as initial states for the direct coexistence method. In the half-frozen configurations used, between 40 and 50 % of the molecules had ice-like structure, as

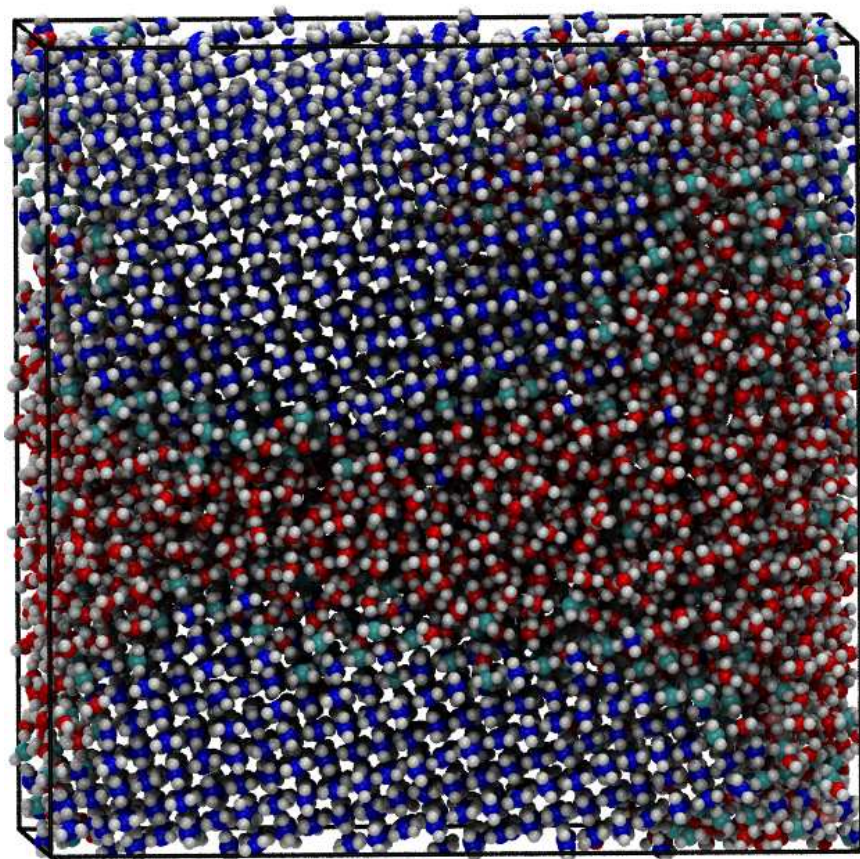


Figure 5.1: Example starting configuration containing ~ 4000 ice-like molecules. The oxygen atoms of cubic ice-like molecules are shown in dark blue, hexagonal ice-like molecules in light blue, and liquid molecules in red. All hydrogen atoms are white.

identified by the CHILL algorithm [75]. In comparison with configurations generated by placing solid and liquid phases in contact, we would expect configurations from freezing trajectories to have lower interfacial energy, and an ice surface (or surfaces) well suited for crystal growth. A sample starting configuration is shown in Fig. 5.1. The melting temperatures, averaged over four independent simulations with $N = 8000$, are reported in Table 5.3.1 for different field magnitudes. The melting temperature increases with field magnitude. For example, the melting temperature increases by ~ 24 K with a field of 1 V/nm, and by ~ 44 K with a field of 2 V/nm, assuming 289 K is the melting temperature in the absence of an electric field [101]. Melting temperatures determined using smaller simulations ($N = 1000$) are consistent with those reported for larger systems and show a similar trend.

We note that to avoid possibly biasing the crystal structure in freezing simulations, it is desirable to allow the box lengths to fluctuate independently, as was done in earlier simulations involving hexagonal ice [128]. However, in the present simulations with an external field, the box geometry fluctuated wildly if the box lengths were allowed to fluctuate independently. Therefore, in our simulations the box length ratios were held fixed. This is not an issue for cubic ice, which is the stable form of fully polarized ice. Moreover, we use a relatively large simulation cell ($N = 8000$), and initial configurations taken from freezing trajectories, which should mitigate any influence of the imposed cell constraints.

With a field of 1 V/nm, the six-site water model freezes readily at 270 K ($\Delta T_S = 44$ K). At the same field, ten independent 50 ns simulations with 8000 molecules showed no sign of freezing at 280 K ($\Delta T_S = 34$ K).

Thus, model water interacting with an electric field does not freeze on the timescales of our simulations until $\Delta T_S \sim 40$ K, similar to the supercooling required to freeze real water on experimental timescales. Our results suggest that electric fields induce freezing in simulations of supercooled water mainly because the true melting point is increased by the field. This means that the true ΔT_S is considerably larger than one would expect based on the melting point of water in the absence of a field. However, the nucleation barrier remains high, and the liquid must be supercooled by ~ 40 K relative to the true field-dependent melting point in order to freeze on simulation timescales.

5.3.2 Ice Clusters and Nucleation

In this section we compare nucleation in polarized water with what is known about nucleation in unpolarized water. In addition, we examine ice cluster formation and ice growth in systems interacting with a field of 1 V/nm, as well as in systems without an external field.

Regardless of field, all supercooled liquid systems studied contained ice-like molecules with both cubic and hexagonal structure. However, nearly all molecules in larger (> 10 molecules) ice clusters had cubic structure in presence of an electric field, with hexagonal structure appearing only near the cluster surface. Both cubic and hexagonal ice consist of repeating hexagonal rings: hexagonal ice contains boat and chair ring configurations, while cubic ice contains only chair configurations. Water dipoles cannot perfectly align (*i.e.*, $\langle m_x \rangle = 1$) in the boat configuration, but can in the chair configuration; thus, only cubic ice grows in strongly polarized water.

5.3. Results

T (K)	ΔT_S (K)	Field (V/nm)	Number of independent simulations	Time (ns)	Average number of ice-like molecules	Largest cluster observed
260	29	0	10	40	33	11
270	19	0	1	40	17	5
270	28	0.8	1	40	24	14
270	44	1.0	10	40	43	45
280	34	1.0	10	50	17	11
290	24	1.0	9	50	11	8

Table 5.2: Summary of ice-like molecules and ice clusters observed in different systems; configurations from each simulation were saved at 10 ps intervals. For some systems, multiple independent simulations were performed as indicated. At 270 K, freezing occurred within 40 ns for each of the ten simulations performed with a field of 1 V/nm; the tabulated data were taken from pre-freezing configurations. For all systems, the largest cluster reported is the largest ice cluster (see text for definition of cluster) observed that subsequently melted.

We report the average numbers of ice-like molecules observed with different field magnitudes and temperatures in Table 5.2, and show ice cluster distributions for polarized (1 V/nm, 270 K and 280 K) and unpolarized (260 K) systems in Fig. 5.2. All results are for simulations with 8000 molecules. The number of ice-like molecules increases with decreasing temperature, as do the number and size of ice clusters. However, less than 1 % of water molecules had ice-like structure in all liquid systems considered, even when supercooled by more than 30 K. For example, 0.2 % of the molecules in a system interacting with a 1 V/nm field have ice-like structure when supercooled by 34 K ($T = 280$ K). In the absence of a field, liquid supercooled by 29 K ($T = 260$ K) contains approximately twice as many ice-like molecules (0.4 %). Fewer ice-like molecules may form when interacting with a field at

5.3. Results

a given ΔT_S because dipole fluctuations are restricted in ice-like structures. Nevertheless, larger ice-like clusters, consisting of eight or more molecules, occurred with the same frequency in polarized and unpolarized systems, as shown in the inset of Fig. 5.2.

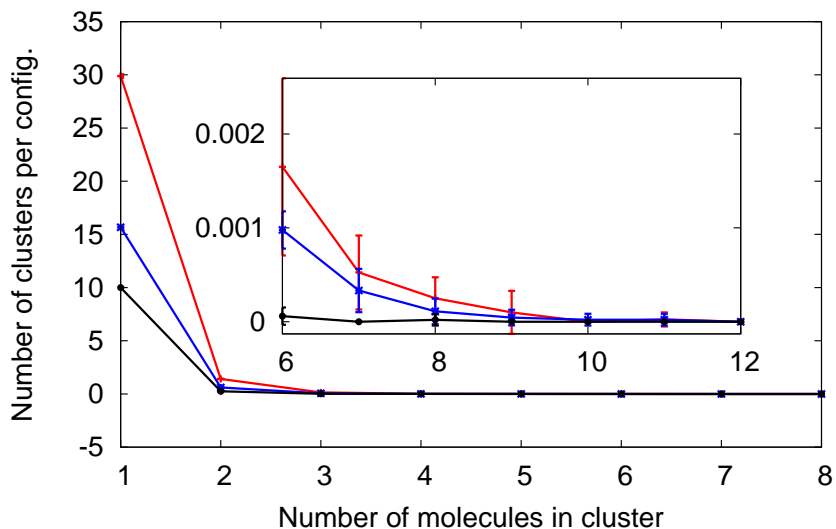


Figure 5.2: Average number of clusters (per configuration) of a given size observed in *NPT* (1 bar) simulations with 8000 molecules. Results are shown for: 0 V/nm, 260 K (red); 1 V/nm, 280 K (blue); 1 V/nm, 290 K (black). Standard errors estimated from ten independent simulations of 40 ns (260 K) or 50 ns (280 and 290 K) are also shown.

Although all systems examined contain very few ice-like molecules, the positions of ice-like molecules are strongly correlated, as shown by the pair distribution functions plotted in Fig. 5.3. Correlations between ice-like molecules grow with decreasing temperature, but are stronger in systems interacting with an electric field, even when they contain fewer ice-like molecules. However, most ice-like molecules form in isolation, and clusters consisting of more than two or three molecules are rare in all systems (Fig.

5.2).

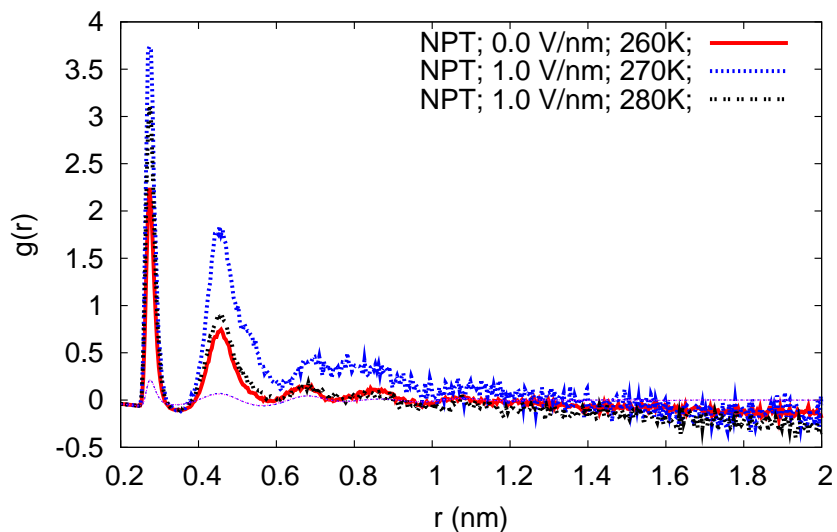


Figure 5.3: Oxygen-oxygen radial distribution functions for ice-like molecules obtained from simulations ($N = 8000$, $P = 1$ bar) for three systems, as indicated in the legend.

Ten independent simulations with 8000 molecules, and four with 32000 molecules, were carried out at 270 K ($\Delta T_S \sim 44$ K) with a field of 1 V/nm. In all cases freezing was observed within 40 ns. Before freezing, the largest ice cluster that formed and then subsequently melted contained ~ 45 molecules. Thus, larger clusters freeze, and we estimate that the critical nucleus at 270 K contains ~ 50 molecules.

With a field of 1 V/nm, spontaneous freezing did not occur for any temperature considered above 270 K. Therefore, to estimate the size of critical nuclei at higher temperatures, we used configurations from the large ($N = 32000$) freezing simulations at 270 K as starting configurations in simulations at higher temperatures. The selected configurations each con-

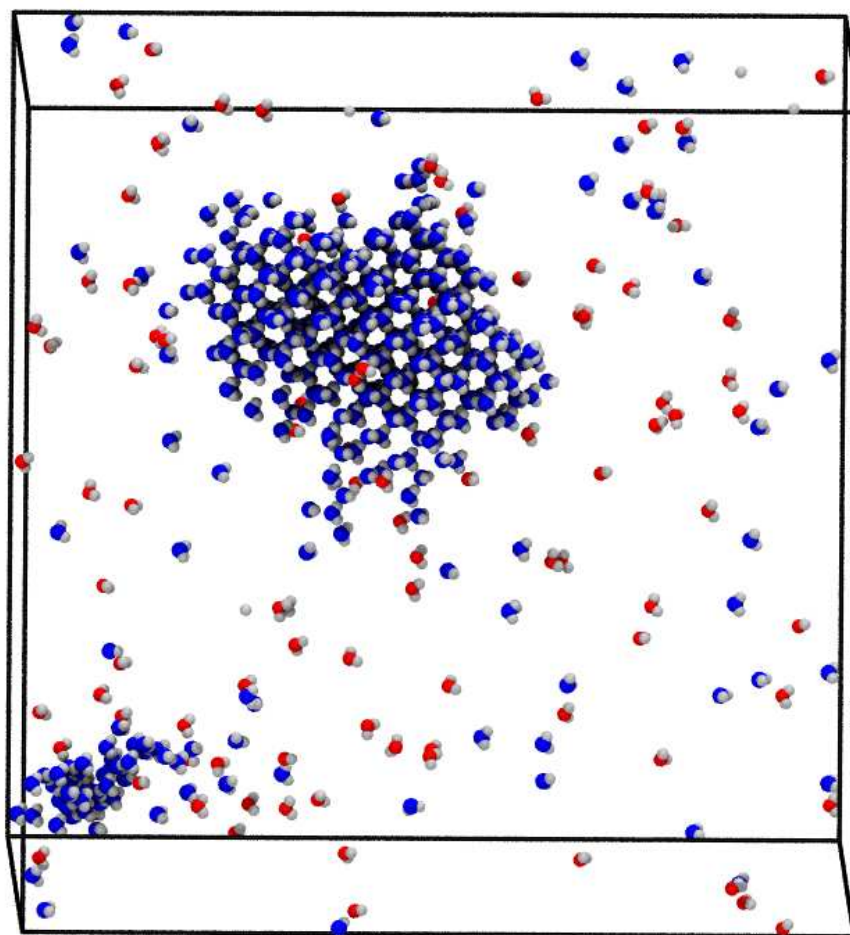


Figure 5.4: Example starting configuration with an ice “nucleus” of ~ 500 molecules. Only cubic (blue) and hexagonal (red) ice-like molecules are shown.

tained one large ice cluster of between 480 and 550 molecules along with other smaller ice clusters and isolated ice-like molecules, as summarized in Table 5.3. An example starting configuration is shown in Fig. 5.4. The ice clusters grew at 290 K ($\Delta T_S \approx 24$ K), but melted at 295 K ($\Delta T_S \approx 19$ K) for all four initial configurations. Thus, the critical nucleus shrinks from ~ 500 molecules when $\Delta T_S \approx 24$ K to ~ 50 molecules when $\Delta T_S \approx 44$ K, in water interacting with a field of 1 V/nm.

The size of the critical nucleus has not been previously reported at any temperature for the six-site model, in the absence of an electric field. To determine whether electric fields affect the size of the critical nucleus for a given ΔT_S , we used the same four starting configurations described above (Table 5.3), each containing an ice cluster of ~ 500 molecules, in simulations without an external electric field. The ice clusters melted within 5 ns at 265 K ($\Delta T_S \approx 24$ K), but unpolarized ice grew on the cluster surfaces at 260 K ($\Delta T_S \approx 29$ K), in all simulations. Growth of unpolarized ice on a polarized nucleus has been observed in previous simulations [115, 116] (Chapter 3 and 4). While we have not precisely determined the lowest temperature at which a 500-molecule ice cluster grows, growth occurred with a 1 V/nm field when $\Delta T_S \approx 24$ K and without a field at $\Delta T_S \approx 29$ K. The two temperatures are reasonably close, suggesting that the size of the critical nucleus for the six-site model depends mostly on the degree of supercooling. This further supports the conclusion noted above, that the effect of the field comes mainly from its influence on the melting point.

A critical nucleus of ~ 500 molecules when $\Delta T_S \approx 29$ K (no field case) is somewhat smaller than estimates for the TIP4P/2005 and TIP4P/Ice

5.3. Results

Simulation	Number of clusters with >10 molecules	Size of largest cluster	Size of 2 nd largest cluster	N_C	N_H	N_I
1	2	485	11	583	110	1183
2	2	515	12	619	102	1171
3	2	507	11	593	127	1173
4	2	545	31	646	111	1232

Table 5.3: Summary of ice-like molecules in starting configurations used to estimate the critical ice nucleus size. The starting configurations were taken from simulations performed with 32000 water molecules interacting with a field of 1 V/nm at 270 K, where freezing eventually occurred. The number of molecules meeting the condition for interfacial ice (N_I), as identified by the CHILL algorithm, are recorded in the table, but only cubic (N_C) and hexagonal (N_H) ice-like molecules were included in determining the size of ice clusters. These four starting configurations were used in simulations to estimate the highest temperature at which the initial ice cluster nucleates ice, both with and without a field.

models (~ 600 molecules when $\Delta T_S = 35$ K) [120]. While the discrepancy might well be due to model differences, our starting configurations were very different from those used by Sanz *et al.* [120], which contained spherical clusters cut from a hexagonal crystal. In our simulations, the starting configurations 1) contained ice clusters that had cubic rather than hexagonal structure, 2) were taken from freezing trajectories, and 3) were polarized, denser, and contained other ice-like molecules, in addition to the ~ 500 molecule ice cluster. With respect to the last point, ice growth was relatively slow at 260 K, taking ~ 5 -10 ns for the cluster to grow to 1000 molecules, allowing sufficient time for system relaxation. For example, in one simulation with 32000 molecules, an initial cluster containing 485 molecules shrank to 448 molecules, and the total number of ice-like molecules decreased by nearly

100 molecules, before irreversible ice growth occurred. The fact that the ice cluster decreased in size suggests that the critical ice nucleus is somewhat smaller than our estimate.

5.3.3 Thermodynamic Functions

Fig. 5.5 shows how the average polarization, configurational energy, field-interaction energy, entropy [Equation (5.4)], and the Gibbs free energy change with field strength. Water becomes more polarized as the field increases; as a result, water molecules interact more favourably with the field, and lose rotational entropy. The average configurational energy also decreases as water molecules align with the field, indicating the presence of more energetically favourable structures. The favourable configurational and field interaction energies compensate for the loss of entropy, and the free energy of liquid water decreases with increasing field (Fig. 5.5).

Usually, liquids are stable with respect to solids because of their greater entropy. Liquid water loses entropy when interacting with a uniform electric field, offering a possible explanation for the increased melting temperature. However, liquid water becomes more stable when interacting with a field ($\Delta G < 0$), and therefore the melting temperature can only increase if ice also becomes more stable. Table 5.3.1 shows that in ice the molecular dipoles align essentially perfectly with the field, whereas significant orientational disorder persists in liquid water at the freezing transition. The entropy of fusion is also larger in the presence of an electric field, indicating that ice loses slightly more entropy than liquid water, likely due to the higher polarization. Although associated with a greater loss of rotational entropy,

5.3. Results

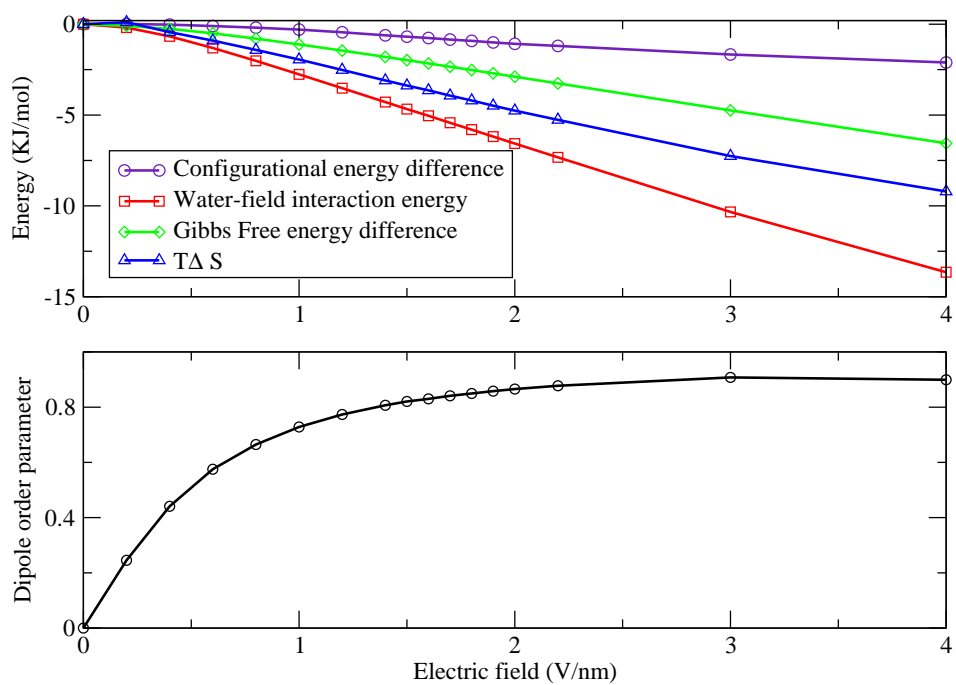


Figure 5.5: Changes in thermodynamic properties (top) and the dipole order parameter (bottom) as functions of field strength.

near perfectly aligned dipoles give ice an energetic advantage through the field-interaction energy. It is in fact this energetic advantage that increases the stability of ice with respect to liquid water, resulting in an increased melting temperature.

To be more explicit, liquid water loses less entropy than ice due to field interactions, and its configurational energy decreases with increasing field (Fig. 5.5), whereas the configurational energy of ice is nearly independent of field. Yet, liquid water loses stability with respect to ice because the partially aligned dipoles in the liquid interact less favourably with the field than the fully aligned dipoles in cubic ice. This suggests that in liquid water the molecular dipoles cannot perfectly align (and take full advantage of the favourable field-interaction energy) without losing entropy due to other structural changes.

It is of interest to compare the observed entropy loss with the expected ideal entropy loss for a non-interacting dipolar fluid polarized by an electric field. The partition function $Q^{ID}(E)$ for ideal, non-interacting, dipolar molecules in the presence of a field is [129]

$$Q^{ID}(E) = Q^{ID}(0) \frac{\sinh y}{y}, \quad (5.10)$$

where $y = \mu_w E/kT$, $E = |\mathbf{E}|$, μ_w is the permanent dipole moment for the six-site water model, k is the Boltzmann constant, and $Q^{ID}(0)$ is the partition function in the absence of a field. The change in the ideal Helmholtz

free energy due to interaction with an applied field is given by

$$\Delta A^{ID}(E) = A_{\text{field}}^{ID} - A_{\text{no field}}^{ID} = -kT \ln[Q^{ID}(E)]. \quad (5.11)$$

The average polarization, \bar{P} , for an ideal system at a specific temperature is calculated through the Langevin function [129]

$$\bar{P} = L(y) = \coth y - \frac{1}{y}. \quad (5.12)$$

The ideal entropy change $\Delta S^{ID}(E)$ can then be obtained

$$\Delta S^{ID}(E) = S_{\text{field}}^{ID} - S_{\text{no field}}^{ID} = \frac{\Delta U^{ID}(E) - \Delta A^{ID}(E)}{T}, \quad (5.13)$$

where $U^{ID}(E) = -\mu_w E \bar{P}$, and $A^{ID}(E) = -kT \ln[Q^{ID}(E)]$. For our simulated *NPT* systems, we determined the change in entropy due to polarization using Equation (5.4).

Fig. 5.6 shows the entropy change as a function of polarization for ideal and simulated systems at 300 K. The simulated system loses slightly less entropy than the ideal dipolar liquid with the same average polarization, likely due to correlations present in the absence of an electric field. However, as the polarization approaches 1, ($\gtrsim 0.87$), liquid water at 300 K loses more entropy than the available ideal rotational entropy, indicating that liquid water adopts a less entropically favoured structure when highly polarized.

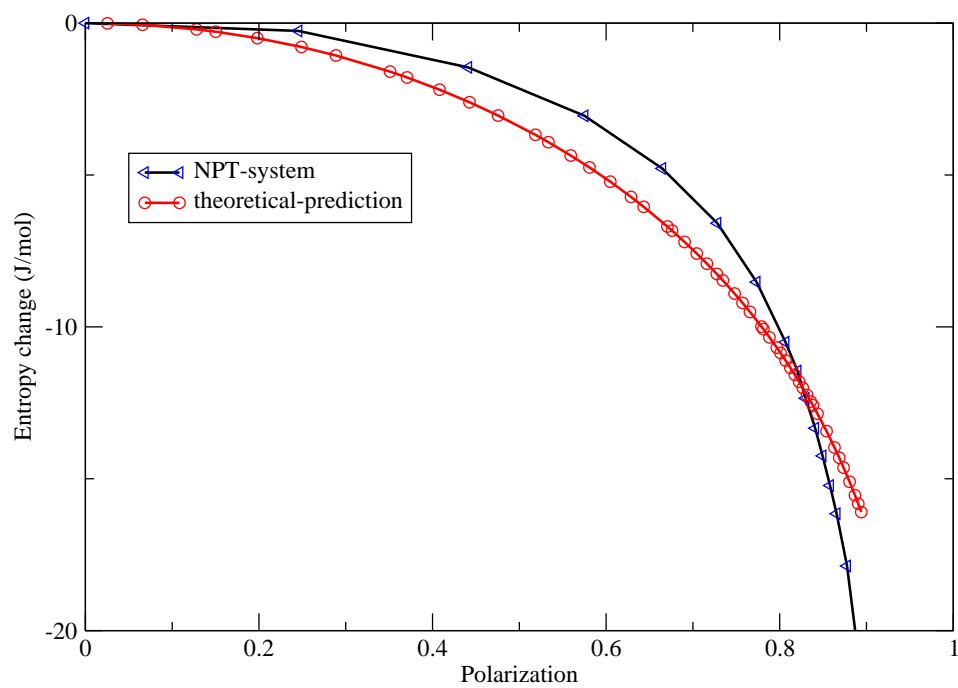


Figure 5.6: Entropy change as a function of polarization ($\langle m_x \rangle$) at 300 K. The red circles are from Equation (5.13), and the blue triangles denote the simulation results. The lines are to guide the eye.

5.3.4 Structural Changes with Field

One might have expected polarization to significantly alter the structure of liquid water. However, consistent with the largely ideal entropy changes discussed above, the structure of liquid water remains qualitatively unchanged by polarization if $\langle m_x \rangle \lesssim 0.87$. This is demonstrated by tetrahedral order parameter distributions (Fig. 5.7) and $r^2h(r)$ plots (Fig. 5.8). We note that water retains its local tetrahedral order (Fig. 5.7), and that $h_{HH}(r)$, $h_{LL}(r)$, and $h_{HL}(r)$ change very little when the liquid is polarized (Fig. 5.8).

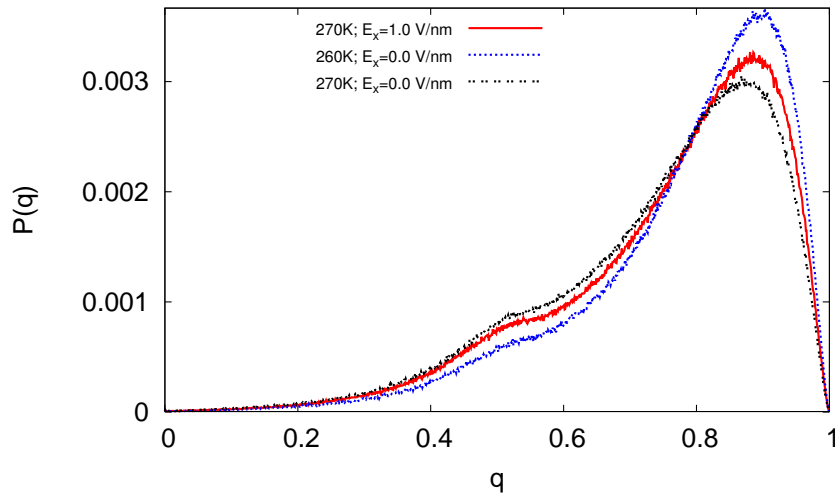


Figure 5.7: Comparison of tetrahedral order parameter distributions at constant pressure for different temperatures and external fields, as indicated in the legend.

Despite these striking similarities, electric fields do induce small quantitative changes in the structure of water. In particular, we note that the local structure becomes more tetrahedral (Fig. 5.7), and the radial correlations increase slightly (Fig. 5.8) in presence of a field. The structure of water interacting with an electric field is similar to that of slightly colder (by ~ 5

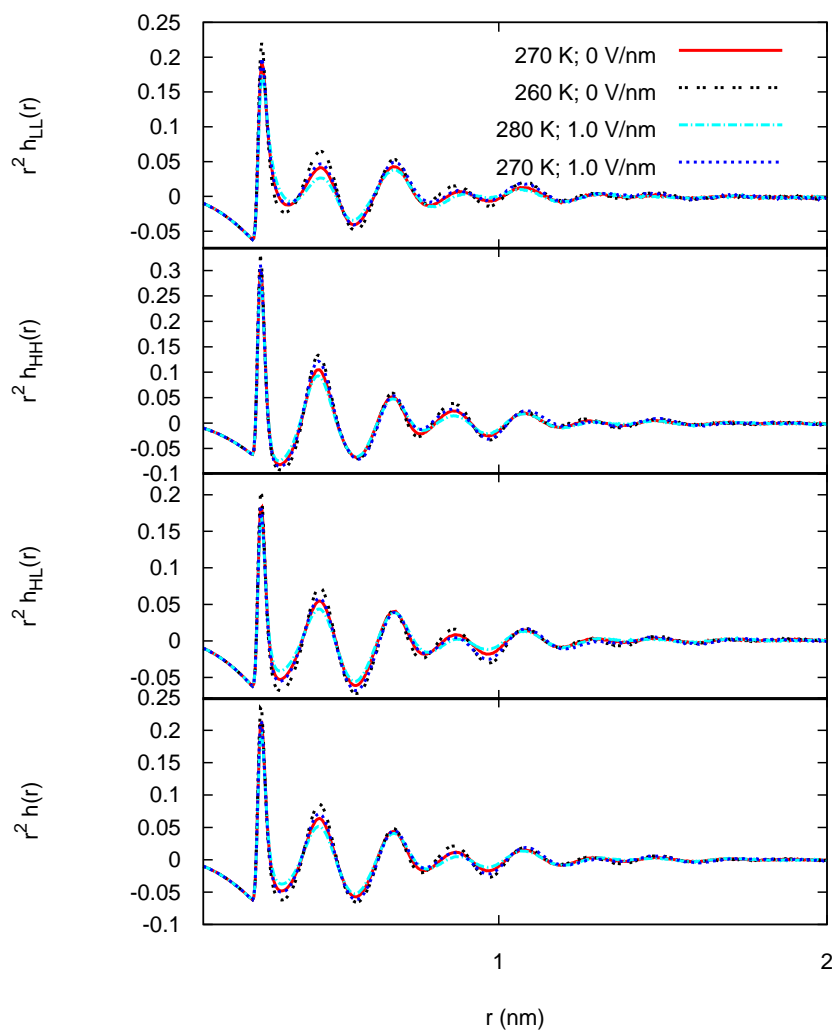


Figure 5.8: Total (bottom) and partial (as labeled) pair correlation functions at the temperatures and fields indicated in the legend. Multiplication by r^2 magnifies the structural features.

K) water in absence of a field, and is consistent with a more negative configurational energy (Fig. 5.5). However, the density of water increases with polarization, for example, from 0.992 to 1.002 g/cm³ at 270 K (Table 5.4). Increased density is usually associated with less tetrahedral structure and warmer water, thus, polarization allows water to accommodate energetically favoured tetrahedral structures in a denser liquid. Nevertheless, the density of polarized water decreases with decreasing temperature, consistent with water’s characteristic density anomaly.

T (K)	Field (V/nm)	Density (g/cm ³)
260	0	0.973
270	0	0.992
270	1.0	1.002
280	1.0	1.019
290	1.0	1.023

Table 5.4: Densities in polarized and unpolarized water from simulations with 8000 molecules at 1 bar.

At higher fields ($\langle m_x \rangle \gtrsim 0.87$ at 300 K) significant structural changes do occur, with water losing some tetrahedral order and gaining long-range correlations. Although loss of tetrahedral structure is usually accompanied by a less favourable configurational energy, highly polarized water has a lower configurational energy. The increased long-range correlations make this structure less entropically favourable, perhaps accounting for the additional loss of entropy, beyond that expected from the loss of rotational entropy that occurs when water is highly polarized. Water froze spontaneously in some *NPT* simulations at 300 K with a field of 5 V/nm; however, a high

density ice, rather than cubic ice, was formed. Nevertheless, cubic ice does not melt at such high fields and has both a lower configurational energy and a lower field-interaction energy than the high density form, suggesting that water freezes to the high density ice structure because it is kinetically accessible, rather than thermodynamically stable.

The concentration-concentration, $S_{CC}(k)$, and number-concentration, $S_{NC}(k)$, structure factors can be calculated from the partial structure factors for H and L molecules, as discussed in Section 5.2. In order to accurately determine the structure factors at low wavenumbers, the relevant radial distribution functions are corrected for finite-size effects following Salacuse *et al.* [130]. The magnitudes of $S(0)$, $S_{CC}(0)$ and $S_{NC}(0)$ increase in the presence of an electric field, indicating that both density and concentration fluctuations increase, as does the coupling between them. The values of $S(0)$, $S_{CC}(0)$ and $S_{NC}(0)$ at 270 K with a field of 1.0 V/nm are comparable to those measured at 260 K in an unpolarized system, as shown in Fig. 5.9. Thus, apart from its higher density, polarized water appears colder, with more tetrahedral local order, stronger structural correlations, and larger coupled density and concentration fluctuations.

5.4 Summary and Conclusions

In this chapter we show that uniform fields on the order of 1-2 V/nm significantly increase the melting point of the six-site water model. The increased stability of polarized cubic ice can be traced to its near perfect polarization, whereas the coexisting liquid achieves only $\sim 80\%$ polarization.

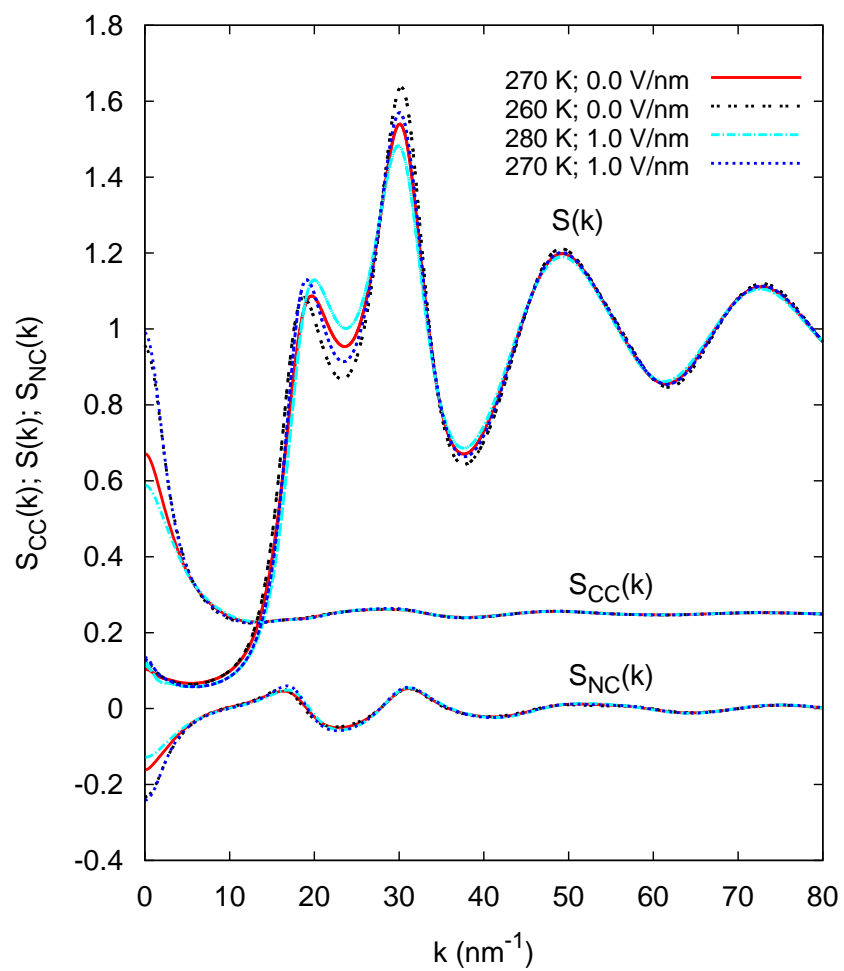


Figure 5.9: Structure factors for the temperatures and electric fields indicated in the legend.

5.4. Summary and Conclusions

Thus, the average field-dipole interaction energy favours the ice. Therefore, compared to the zero field case, at a given temperature polarized water is more deeply supercooled relative to its true field-dependent melting point. This reduces the size of the critical nucleus, and helps explain why polarized water freezes readily on simulation timescales. We find spontaneous freezing at $\Delta T_S = T_M - T \approx 40$ K. We also show that the size of the critical ice nucleus is mostly determined by ΔT_S , regardless of field.

Our observations also offer an explanation for heterogeneous ice nucleation by local electric fields. As noted above, uniform electric fields as large as those considered in this work would cause dielectric breakdown in real water. However, water can remain stable when interacting with large local fields generated by ions or surface charge groups [55–57, 63]. Fields generated by some ice-nucleating materials may cause nearby water dipoles to partially align with the field, thereby effectively increasing ΔT_S locally. Since the size of the critical nucleus decreases with increasing ΔT_S , molecules affected by the local field can freeze, and nucleate bulk ice, as demonstrated in Chapter 3 and 4. Weaker electric fields may also nucleate ice, but at a rate that is too slow to observe in simulations currently feasible.

Although supercooled water contains rather few ice-like molecules ($< 1\%$), ice-like molecules associate strongly with each other, both with and without an interacting electric field. For the same degree of supercooling (ΔT_S), water molecules form ice-like structures less readily in presence of an electric field, but the ice-like molecules that do form associate with each other more strongly.

It is interesting to note that the structure of water in a uniform electric

5.4. *Summary and Conclusions*

field shows little qualitative change until very high polarization ($\gtrsim 87\%$) is achieved. At lower polarizations water maintains its normal tetrahedral, hydrogen-bonded structure and characteristic spatial correlations. Even the density anomaly and the anomalous increase in the structure factor at low wavenumber are left intact by the field. Thus, atomic-level information obtained from simulations with electric fields may provide some insight into homogeneous ice nucleation in absence of a field.

Chapter 6

Conclusions and Perspective

6.1 Simulation Results on Ice Nucleation and Electrofreezing

This thesis systematically investigates the process of ice nucleation induced by electric fields, and why external electric fields promote the freezing of liquid water. The microscopic mechanism and the growth pattern of ice nucleation are focuses of the investigation. Molecular dynamics simulations are employed to simulate the occurrence of ice, and calculate structural and dynamical properties, such as density and dipole order profiles, radial distribution functions, ice-like molecule detections, diffusion coefficients, and so forth.

In Chapter 2, models of water and the confinement geometries are described in detail, as is the model of electric fields used in this thesis. The computational approaches of molecular dynamics simulation are introduced, and methods of data analysis of the simulation results are discussed.

In Chapter 3, ice formation induced by a decaying field, which acts near the entire surface, is described. It is demonstrated that a surface field can create an effective ice nucleus in models of supercooled liquid water.

6.1. Simulation Results on Ice Nucleation and Electrofreezing

The field must polarize only a very thin water layer ($\sim 10 \text{ \AA}$), and the field strength required is realistic on the relevant length scale. Ice with ferroelectric cubic structure nucleates near the surface, and dipole disordered cubic ice grows outward from the surface. Moreover, two different water models (the six-site and TIP4P/Ice models) are compared, and in both cases it is shown that a surface field can serve as a very effective ice nucleation catalyst in supercooled water. We examine the influence of temperature and two important field parameters, the field strength and distance from the surface over which it acts, on the nucleation process. For the six-site model the highest temperature where we observe field-induced ice nucleation is 280 K (normal melting point is 289 K), and for TIP4P/Ice 270 K (normal melting point is 270 K). The minimum electric field strength required to nucleate ice on the timescales of our simulations depends a little on how far the field extends from the surface. If it extends 20 \AA , then a field strength of $1.5 \times 10^9 \text{ V/m}$ is effective for both models. If the field extent is 10 \AA , then stronger fields are required ($2.5 \times 10^9 \text{ V/m}$ for TIP4P/Ice, and $3.5 \times 10^9 \text{ V/m}$ for the six-site model). Our results demonstrate that fields of realistic strength, that act only over a narrow surface region, can effectively nucleate ice at temperatures not far below the freezing point. This supports the possibility that local electric fields can be a significant factor influencing heterogeneous ice nucleation in physical situations.

In Chapter 4, the surface field is modified so that it decays in two directions. Field “bands” of different geometry all nucleate ice, provided that the band is sufficiently large. Rectangular bands are very efficient if the width and thickness are $\gtrsim 0.35 \text{ nm}$, and $\gtrsim 0.15 \text{ nm}$, respectively,

and the necessary dimensions are comparable for other geometries. Careful analysis of different systems reveals that ice strongly prefers to grow at (111) planes of cubic ice. This agrees with an earlier theoretical deduction based on considerations of water-ice interfacial energies [111]. It is found that ice nucleated by field bands usually grows as a mixture of cubic and hexagonal ice, consistent with other simulations of ice growth [73, 75, 99, 119], and with experiment [103, 106]. The mixture of ice Ih and Ic contrasts with simulations carried out with nucleating fields that span the entire surface area, where cubic ice dominates, and hexagonal layers are very rarely observed [115, 116]. This discrepancy is mainly a simulation artifact related to finite sample size and periodic boundary conditions.

We have found that ice nucleates efficiently when induced by an electric field. However, the question of how an electric field enhances ice nucleation is also of interests. In Chapter 5, we investigate the structural and thermodynamic changes that promote freezing when liquid water interacts with a uniform, external field. The melting temperature increases significantly when electric fields are applied. Fields of 1×10^9 V/m and 2×10^9 V/m increase the melting point by 24 K and 44 K, respectively. The increased melting point is mainly due to the favourable interaction of near perfectly polarized cubic ice with the applied field. For a fixed temperature, we demonstrate that the size of the critical ice nucleus decreases with field present in the system mostly because the melting point, and hence the true degree of supercooling, is increasing with field. On simulation timescales, ice nucleation is observed at 40 K below the field-dependent melting point, independent of the particular value of the field applied. We find that even

quite highly polarized liquid water retains its characteristic local structure, and the related anomalous properties of water. These results are relevant to the mechanism of heterogeneous ice nucleation by local surface fields as discussed in earlier chapters. Local fields can effectively increase the degree of supercooling of locally polarized liquid, decreasing the size of the critical nucleus in the region influenced by the field, hence facilitating ice nucleation.

6.2 Future Work

Our simulation results support the idea that local electric fields could play a major role in heterogeneous ice nucleation, particularly for rough particles with many surface structure variations, such as kaolinite. These particles can serve as ice nuclei in environmentally realistic situations. One area of future work would be the investigation of ice nucleation on more realistic surfaces with different arrangements of charge. Replacing the smooth walls with an atomistic surface would be a step in that direction. An atomistic surface could be “decorated” with different charges, which might have a large influence on ice nucleation near the surface. It has been reported that water freezes differently on positively and negatively charged surfaces in experiments [57], and using a more realistic atomistic surface is one way to simulate similar physical environments.

Simulations of ice nucleation on realistic particle models are of great interest. Silver iodide is one of the best IN known [7] and can nucleate ice at temperatures as warm as -3°C . Under atmospherically relevant conditions, two phases of silver iodide exist [131], β -AgI and γ -AgI, with either silver

6.2. Future Work

or iodide ions exposed to the adjacent medium. The AgI faces are both made of chair conformation hexagonal rings of alternating silver and iodide ions forming a bilayer, such that either all silver or all iodide ions occupy the topside layer. The interaction between water and surfaces may be influenced by the Coulombic attraction between water and the positive silver or the negative iodide ions. It is speculated that the “bonding” between water molecules and different AgI faces is important in ice nucleation. Recent progress has been made in this area in our research group [132].

Many other surfaces are of much interest as possible ice nuclei. In biological systems, some proteins have been observed to promote ice nucleation [55]. Simulations with water and proteins at different temperatures is another promising area of research in ice nucleation.

Bibliography

- [1] B. J. Murray, D. OSullivan, J. D. Atkinson and M. E. Webb, Ice nucleation by particles immersed in supercooled cloud droplets. *Chem. Soc. Rev.* **41**, 6519, (2012).
- [2] J. H. Seinfeld and S. N. Pandis, *Atmospheric chemistry and physics - From air pollution to climate change*. 1326 pp., (John Wiley & Sons, Inc., New York, 1998).
- [3] D. A. Hegg and M. B. Baker, Nucleation in the atmosphere. *Rep. Prog. Phys.* **72**, 056801, (2009).
- [4] M. B. Baker, Cloud microphysics and climate. *Science*, **276**, 1072, (1997).
- [5] M. B. Baker and T. Peter, Small-scale cloud processes and climate. *Nature*, **451**, 299, (2008).
- [6] B. Zuberi, A. K. Bertram, C. A. Cassa, L. T. Molina, and M. J. Molina, Heterogeneous nucleation of ice in $(\text{NH}_4)_2\text{SO}_4\text{-H}_2\text{O}$ particles with mineral dust immersions. *Geophys. Res. Lett.* **29**, 142, (2002).
- [7] H. R. Pruppacher and J. D. Klett, *Microphysics of Clouds and Precipitation* (2nd rev. ed.; Kluwer Academic: Dordrecht, 1997).

- [8] S. Hartmann, D. Niedermeier, J. Voigtlander, T. Clauss, R. A. Shaw, H. Wex, A. Kiselev and F. Stratmann, Homogeneous and heterogeneous ice nucleation at LACIS: operating principle and theoretical studies. *Atmos. Chem. Phys.*, **11**, 1753, (2011).
- [9] T. Bartels-Rausch, V. Bergeron, J. H. E. Cartwright, R. Escribano, J. L. Finney, H. Grothe, P. J. Gutiérrez, J. Haapala, W. F. Kuhs, J. B. C. Pettersson, S. D. Price, C. I. Sainz-Díaz, D. J. Stokes, G. Strazzulla, E. S. Thomson, H. Trinks and N. Uras-Aytemiz, Ice structures, patterns, and processes: A view across the icefields. *Rev. Mod. Phys.* **84**, 885, (2012).
- [10] W. Cantrell and A. Heymseld, Production of ice in tropospheric clouds a review. *B. Am. Meteorol. Soc.* **86**, 795, (2005).
- [11] C. Hoose, J. E. Kristjánsson, J-P. Chen and A. Hazra, A classical-theory-based parameterization of heterogeneous ice nucleation by mineral dust, soot, and biological particles in a global climate model. *J. Atmos. Sci.* **67**, 2483, (2010).
- [12] D. J. Cziczo, P. J. DeMott, C. Brock, P. K. Hudson, B. Jesse, S. M. Kreidenweis, A. J. Prenni, J. Schreiner, D. S. Thomson and D. M. Murphy, A method for single particle mass spectrometry of ice nuclei. *Aerosol Sci. Technol.*, **37**, 460, (2003).
- [13] P. J. DeMott, D. J. Cziczo, A. J. Prenni, D. M. Murphy, S. M. Kreidenweis, D. S. Thomson, R. Borys and D. C. Rogers,

- Measurements of the concentration and composition of nuclei for cirrus formation. *Proc. Natl. Acad. Sci. U. S. A.*, **100**, 14655, (2003).
- [14] K. A. Pratt, P. J. DeMott, J. R. French, Z. Wang, D. L. Westphal, A. J. Heymsfield, C. H. Twohy, A. J. Prenni and K. A. Prather, In situ detection of biological particles in cloud ice-crystals. *Nat. Geosci.*, **2**, 397, (2009).
- [15] J. M. Prospero, P. Ginoux, O. Torres, S. E. Nicholson and T. E. Gill, Environmental characterization of global sources of atmospheric soil dust identified with the NIMBUS 7 Total Ozone Mapping Spectrometer (TOMS) absorbing aerosol product. *Rev. Geophys.*, **40**, 1002, (2002).
- [16] R. A. Glaccum and J. M. Prospero, Saharan aerosols over the tropical North Atlantic-Mineralogy. *Marine Geology* **37(3-4)**, 295, (1980).
- [17] D. J. Cziczo, D. M. Murphy, P. K. Hudson and D. S. Thomson, Single particle measurements of the chemical composition of cirrus ice residue during CRYSTAL-FACE. *J. Geophys. Res.-Atm.* **109**, 4517, (2004).
- [18] M. Dymarska, B. J. Murray, L. Sun, M. L. Eastwood, D. A. Knopf and A. J. Bertram, Deposition ice nucleation on soot at temperatures relevant for the lower troposphere. *J. Geophys. Res.-Atm.* **111**, D4, (2006).
- [19] M. L. Eastwood, S. Cremel, C. Gehrke, E. Girard and A. K. Bertram, Ice nucleation on mineral dust particles: Onset conditions, nucleation rates and contact angles. *J. Geophys. Res.-Atm.* **113**, D22203, (2008).

- [20] F. Zimmermann, M. Ebert, A. Worringer, L. Schtz and S. Weinbruch, Environmental scanning electron microscopy (ESEM) as a new technique to determine the ice nucleation capability of individual atmospheric aerosol particles. *Atmos. Environ.* **41**, 8219, (2007).
- [21] S. J. Cox, Z. Raza, S. M. Kathmann, B. Slater and A. Michaelides, The Microscopic Features of Heterogeneous Ice Nucleation May Affect The Macroscopic Morphology of Atmospheric Ice Crystals. *Faraday Discuss.*, **167**, 389, (2013).
- [22] J.F. Bell, III, Water on Planets. *Proc. Int. Astron. Union*, **15**, 29, (2009).
- [23] J. H. E. Cartwright, B. Escribano, and C.I. Sainz-Díaz, The mesoscale morphologies of ice films: Porous and biomorphic forms of ice under astrophysical conditions. *Astrophys. J.*, **687**, 1406, (2008).
- [24] F. Franks, Nucleation of ice and its management in ecosystems. *Phil. Trans. R. Soc. Lond. A*, **361**, 557, (2003).
- [25] R. E. Lee, G. J. Warren and L. V. Gusta, *Biological Ice Nucleation and its Applications* (American Phytopathological Society, St. Paul, 1995).
- [26] K. E. Zachariassen and E. Kristiansen, Ice nucleation and antinucleation in nature. *Cryobiology*, **41(4)**, 257, (2000).
- [27] Y. Ma, L. Zhong, H. Zhang and C. Xu, Effect of applied electric field

on the formation and structure of ice in biomaterials during freezing. Proc.of the 10rd ICSD, 789, (2010).

- [28] D. Gurian-Sherman and S. E. Lindow, Bacterial ice nucleation: significance and molecular basis. FASEB J., **7(14)**, 1338, (1993).
- [29] S. E. Lindow, The role of bacterial ice nucleation in frost injury to plants. Annu. Rev. Phytopathol. **21**, 363,(1983).
- [30] L. Mishchenko, B. Hatton, V. Bahadur, J. A. Taylor, T. Krupenkin and J. Aizenberg, Design of Ice-free Nanostructured Surfaces Based on Repulsion of Impacting Water Droplets. ACS Nano, **4(12)**, 7699, (2010).
- [31] A. Alizadeh, M. Yamada, R. Li, W. Shang, S. Otta, S. Zhong, L. Ge, A. Dhinojwala, K. R. Conway, V. Bahadur, A. J. Vinciguerra, B. Stephens and M. L. Blohm, Dynamics of Ice Nucleation on Water Repellent Surfaces. Langmuir, **28(6)**, 3180, (2012).
- [32] J. M. Strong-Gunderson, R. E. Lee, Jr., and M. R. Lee, Topical Application of Ice-Nucleating-Active Bacteria Decreases Insect Cold Tolerance. Appl Environ Microbiol., **58(9)**, 2711, (1992).
- [33] R. E. Feeney, T. S. Burcham and Y. Yeh, Antifreeze glycoproteins from polar fish blood. Ann. Rev. Biophys. Biophys. Chem., **15**, 59, (1986).
- [34] Z. Gezgin, T. C. Lee and Q. Huang, Engineering functional nanothin

- multilayers on food packaging: ice-nucleating polyethylene films. *J Agric Food Chem.*, **61(21)**, 5130, (2013).
- [35] J. Li, M. P. Izquierdo and T. C. Lee, Effects of ice-nucleation active bacteria on the freezing of some model food systems. *Int. J. Food Sci. Technol.*, **32**, 41, (2003).
- [36] J. C. Liao and K. C. Ng, Effect of ice nucleators on snow making and spray freezing. *Ind. Eng. Chem. Res.*, **29(3)**, 361, (1990).
- [37] A. Michaelides and K. Morgenstern, Ice nanoclusters at hydrophobic metal surfaces. *Nature Mater.*, **6**, 597, (2007).
- [38] M. Volmer and A. Weber, A. Keimbildung in übersättigten Gebilden. *Z. Phys. Chem. (Leipzig)*, **119**, 227 (1926).
- [39] L. Farkas, Velocity of nucleation in supersaturated vapours. *Z. Phys. Chem. (Leipzig)*, **125**, 236, (1927).
- [40] R. Becker and W. Döring, Kinetische Behandlung der Keimbildung in übersättigten Dämpfen. *Ann. Phys.*, **24**, 719, (1935).
- [41] J. Frenkel, Statistical theory of condensation phenomena. *J. Chem. Phys.*, **7**, 200, (1939).
- [42] J. Curtius, Nucleation of atmospheric aerosol particles. *C. R. Physique*, **7**, 1027, (2006).
- [43] C. Hoose and O. Mühler, Heterogeneous ice nucleation on atmospheric aerosols: a review of results from laboratory experiments. *Atmos. Chem. Phys.*, **12**, 9817, (2012).

- [44] C. A. Stan, S. K. Y. Tang, K. J. M. Bishop and G. M. Whitesides, Externally applied electric fields up to 1.6×10^5 V/m do not affect homogeneous nucleation of ice in supercooled water. *J. Phys. Chem. B*, **115**, 1089, (2011).
- [45] P. W. Wilson; K. Osterday and A. D. J. Haymet, The effects of electric field on ice nucleation may be masked by the inherent stochastic nature of nucleation. *CryoLetters*, **30**, 96, (2009).
- [46] H. M. Jones and E. E. Kunhardt, The influence of pressure and conductivity on the pulsed breakdown of water. *IEEETrans. DEI-1*, 1016, (1994).
- [47] I. M. Svishchev and P. G. Kusalik, Crystallization of liquid water in a molecular dynamics simulation. *Phys. Rev. Lett.* **73**, 975, (1994).
- [48] G. R. Edwards and L. F. Evans, Effect of Surface Charge on Ice Nucleation by Silver Iodide. *Trans. Faraday Soc.* **58**, 1649, (1962).
- [49] G. A. Dawson and G. R. Cardell, Electrofreezing of supercooled waterdrops. *J. Geophys. Res.* **78**, 8864, (1973).
- [50] J. B. Doolittle and G. Vali, Heterogeneous freezing nucleation in electric fields. *J. Atmos. Sci.* **32**, 375, (1975).
- [51] T. G. Gabarashvili and N. V. Gliko, Origination of the ice phase in supercooled water under the influence of electrically charged crystals. *Atmos. Oceanic Phys.* **3**, 324, (1967).

- [52] M. A. Abbas and J. Latham, The electrofreezing of supercooled water drops. *J. Meteor. Soc. Japan* **47**, 65, (1969).
- [53] H. R. Pruppacher, Electrofreezing of supercooled water. *Pure Appl. Geophys.* **104**, 623, (1973).
- [54] B. A. Tinsley and G. W. Deen, Apparent tropospheric response to MeV-GeV particle flux variations: A connection via electrofreezing of supercooled water in high-level clouds? *J. Geophys. Res.* **96**, 22283, (1991).
- [55] M. Gavish, J. L. Wang, M. Eisenstein, M. Lahav and L. Leiserowitz, The role of crystal polarity in alpha-amino acid crystals for induced nucleation of ice. *Science.* **256**, 815, (1992).
- [56] I. Braslavsky and S. G. Lipson, Electrofreezing effect and nucleation of ice crystals in free growth experiments. *Appl. Phys. Lett* **72**, 264, (1998).
- [57] D. Ehre, E. Lavert, M. Lahav and I. Lubomirsky, Water freezes differently on positively and negatively charged surfaces of pyroelectric materials. *Science.* **327**, 672, (2010).
- [58] I. M. Svishchev and P. G. Kusalik, Electrofreezing of liquid water: a microscopic perspective. *J. Am. Chem. Soc.* **118**, 649, (1996).
- [59] W. L. Jorgensen, J. Chandrasekhar, J. D. Madura, R. W. Impey and M. L. Klein, Comparison of simple potential functions for simulating liquid water. *J. Chem. Phys.* **79**, 926, (1983).

- [60] H. J. C. Berendsen, J. R. Grigera and T. P. Straatsma, The missing term in effective pair potentials. *J. Phys. Chem.* **91**, 6269, (1987).
- [61] X. Xia and M. L. Berkowitz, The electric field induced restructuring of water at platinum/water interface: molecular dynamics computer simulation. *Phys. Rev. Lett.* **74**, 3193, (1995).
- [62] R. Zangi and A. E. Mark, Electrofreezing of confined water. *J. Chem. Phys.* **120**, 7123, (2004).
- [63] T. Croteau, A. K. Bertram and G. N. Patey, Observations of high-density ferroelectric ordered water in kaolinite trenches using Monte Carlo simulations. *J. Phys. Chem. A*, **114**, 8396, (2010).
- [64] T. Croteau, A. K. Bertram and G. N. Patey, Adsorption and Structure of Water on Kaolinite Surfaces: Possible Insight into Ice Nucleation from Grand Canonical Monte Carlo Calculations. *J. Phys. Chem. A*. **112**, 10708, (2008).
- [65] D. R. Nutt and A. J. Stone, Ice nucleation on a model hexagonal surface. *Langmuir*. **20**, 8715, (2004).
- [66] X. L. Hu and A. Michaelides, Ice formation on kaolinite: lattice match or amphoterism? *Surf. Sci.* **601**, 5378, (2007).
- [67] X. L. Hu and A. Michaelides, Water on the hydroxylated (011) surface of kaolinite: from monomer adsorption to a flat 2D wetting layer. *Surf. Sci.* **602**, 960, (2008).

- [68] F. Lüönd, O. Stetzer, A. Welti and U. Lohmann, Experimental study on the ice nucleation ability of size-selected kaolinite particles in immersion mode. *L. Geophys. Res.* **115**, D14201-1-14, (2010).
- [69] X. L. Hu and A. Michaelides, The kaolinite (001) polar basal plane. *Surf. Sci.* **604**, 111, (2010).
- [70] L. Vrbka and P. Jungwirth, Homogeneous Freezing of Water Starts in the Subsurface. *J. Phys. Chem. B.* **110**, 18126, (2006).
- [71] J. L. F. Abascal, E. Sanz, R. Garcia Fernander, and C. Vega, A potential model for the study of ices and amorphous water: TIP4P/Ice. *J. Chem. Phys.* **122**, 234511, (2005).
- [72] H. Nada and J. P. J. M. van der Eerden, An intermolecular potential model for the simulation of ice and water near the melting point: A six-site model of H₂O. *J. Chem. Phys.* **118**, 7401, (2003).
- [73] M. A. Carignano, Formation of stacking faults during ice growth on hexagonal and cubic substrates. *J. Phys. Chem. C* **111**, 501 (2007).
- [74] G. P. Johari, On the coexistence of cubic and hexagonal ice between 160 and 240 K. *Phil. Mag. B* **78**, 375, (1998).
- [75] E. B. Moore, E. de la Llave, K. Welke, D. A. Scherlis and V. Molinero, Freezing, melting and structure of ice in a hydrophilic nanopore. *Phys. Chem. Chem. Phys.* **12**, 4124, (2010).
- [76] J. C. Shelley and G. N. Patey, Boundary condition effects in

- simulations of water confined between planar walls. *Mol. Phys.* **88**, 385, (1996).
- [77] M. P. Allen and D. J. Tildesley, *Computer Simulations of Liquids* (Clarendon: Oxford, U.K., 1987).
- [78] H. A. Lorentz, Ueber die Anwendung des Satzes vom Virial in der kinetischen Theorie der Gase. *Ann. Phys.* **248**, 127, (1881).
- [79] D. Berthelot, Sur le Mélange des Gaz. *C. R. Hebd. Séanc. Acad. Sci.* **126**, 1703, (1898).
- [80] A. Y. Toukmaji and J. A. Board, Ewald summation techniques in perspective: A survey. *Computer Phys. Communication.* **95**, 73, (1995).
- [81] M. Deserno and C. Holm, How to mesh up Ewald sums. I. A theoretical and numerical comparison of various particle mesh routines. *J. Chem. Phys.* **109**(18), 7678, (1998).
- [82] D. J. Evans, On the representation of orientation space. *Mol. Phys.* **34**, 317, (1977).
- [83] D. J. Evans and S. Murad, Singularity free algorithm for molecular dynamics simulation of rigid polyatomics. *Mol. Phys.* **34**, 327, (1977).
- [84] R. J. Sadus, *Molecular Simulation of Fluids: theory, algorithms, and object-orientation.* (Elsevier, New York, 1999).

- [85] I. P. Omelyan, On the numerical integration of motion for rigid polyatomics: The modified quaternion approach. *Comput. in Phys.* **12**, 97, (1998).
- [86] D. J. Evans and G. P. Morriss, *Statistical Mechanics of Nonequilibrium Liquids*, 2nd ed.; ANU E Press: Canberra, 2007; Chap. 5.2.
- [87] B. Hess, C. Kutzner, D. van Der Spoel and E. Lindahl, GROMACS 4: algorithms for highly efficient, load-balanced, and scalable molecular simulation. *J. Chem. Theory Comput.* **4**, 435, (2008).
- [88] S. J. Plimpton, Fast parallel algorithms for short-range molecular dynamics. *J. Comput. Phys.* **117**, 1, (1995).
- [89] U. Essmann, L. Perera, M. L. Berkowitz, T. Darden, H. Lee, and L. G. Pedersen, A smooth particle mesh Ewald method. *J. Chem. Phys.* **103**, 8577, (1995).
- [90] R. W. Hockney and J. W. Eastwood, *Computer Simulation Using Particles*. (CRC Press, 2010).
- [91] H. Kamberaj, R. J. Low, and M. P. Neal, Time reversible and symplectic integrators for molecular dynamics simulations of rigid molecules. *J. Chem. Phys.* **122**, 224114, (2005).
- [92] W. C. Swope, H. C. Andersen, P. H. Berens, and K. R. Wilson, A computer-simulation method for the calculation of equilibrium-constants for the formation of physical clusters of molecules: Application to small water clusters. *J. Chem. Phys.* **76**, 637, (1982).

- [93] S. Nosé, A molecular dynamics method for simulations in the canonical ensemble. *Mol. Phys.* **52**, 255, (1984).
- [94] W. G. Hoover, Canonical dynamics: equilibrium phase-space distribution. *Phys. Rev. A*, **31**, 1695, (1985).
- [95] B. Hess, H. Bekker, H. J. C. Berendsen, and J. G. E. M. Fraaije, LINCS: A linear constraint solver for molecular simulations. *J. Comp. Chem.* **18**, 1463, (1997).
- [96] R. W. Hockney, S. P. Goel and J. Eastwood, Quiet high resolution computer models of a plasma. *J. Comp. Phys.* **14**, 148, (1974).
- [97] M. Parrinello and A. Rahman, Polymorphic transitions in single crystals: A new molecular dynamics method. *J. Appl. Phys.* **52**, 7182, (1981).
- [98] S. Nosé and M. L. Klein, Constant pressure molecular dynamics for molecular systems. *Mol. Phys.* **50**, 1055, (1983).
- [99] A. V. Brukhno, J. Anwar, R. Davidchack and R. Handel, Challenges in molecular simulation of homogeneous ice nucleation. *J. Phys.: Condense. Matter.* **20**, 494243, (2008).
- [100] T. Koop and B. Zobrist, Parameterizations for ice nucleation in biological and atmospheric systems. *Phys. Chem. Chem. Phys.* **11**, 10839, (2009).
- [101] J. L. F. Abascal, R. G. Fernández, C. Vega and M. A. Carignano, The

- melting temperature of the six site potential model of water. *J. Chem. Phys.* **125**, 166101-1-2, (2006).
- [102] R. G. Fernández, J. L. F. Abascal and C. Vega, The melting point of ice I_h for common water models calculated from direct coexistence of the solid-liquid interface. *J Chem. Phys.* **124**, 144506-1-11, (2006).
- [103] B. J. Murray, D. A. Knopf and A. K. Bertram, The formation of cubic ice under conditions relevant to Earth's atmosphere. *Nature*, **434**, 202, (2005).
- [104] G. P. Johari, Water's size-dependent freezing to cubic ice. *J. Chem. Phys.* **122**, 194504-1-5, (2005).
- [105] A. V. Gubskaya and P. G. Kusalik, The total molecular dipole moment for liquid water. *J. Chem. Phys.* **117**, 5290, (2002).
- [106] T. L. Malkin, B. J. Murray, A. V. Brukhno, J. Anwar and C. G. Salzmann, Structure of ice crystallized from supercooled water. *Proc. Natl. Acad. Sci.* **109**, 1041, (2012).
- [107] E. B. Moore and V. Molinero, Is it cubic? Ice crystallization from deeply supercooled water. *Phys. Chem. Chem. Phys.* **13**, 20008, (2011).
- [108] J. C. Johnston and V. Molinero, Crystallization, melting, and structure of water nanoparticles at atmospherically relevant temperatures. *J. Am. Chem. Soc.* **134**, 6650, (2012).

- [109] L. Tianshu, D. Donadio, G. Russo and G. Galli, Homogeneous ice nucleation from supercooled water. *Phys. Chem. Chem. Phys.* **13**, 19807, (2011).
- [110] D. Quigley and P. M. Rodger, Metadynamics simulations of ice nucleation and growth. *J. Chem. Phys.* **128**, 154518-1-7, (2008).
- [111] T. Takahashi, On the role of cubic structure in ice nucleation. *J. Crystal Growth*, **59**, 441, (1982).
- [112] J. P. D. Abbatt, Interactions of atmospheric trace gases with ice surfaces: adsorption and reaction. *Chem. Rev.* **103**, 4783 (2003).
- [113] E. B. Moore and V. Molinero, Structural transformation in supercooled water controls the crystallization rate of ice. *Nature* **479**, 506 (2011).
- [114] A. Reinhardt, J. P. K. Doye, E. G. Noya, and C. Vega, Local order parameters for use in driving homogeneous ice nucleation with all-atom models of water. *J. Chem. Phys.* **137**, 194504 (2012).
- [115] J. Y. Yan and G. N. Patey, Heterogeneous ice nucleation induced by electric fields. *J. Phys. Chem. Lett.* **2**, 2555 (2011).
- [116] J. Y. Yan and G. N. Patey, Molecular Dynamics Simulations of Ice Nucleation by Electric Fields, *J. Phys. Chem. A.* **116(26)**, 7057, (2012).
- [117] S. Bauerecker, P. Ulbig, V. Buch, L. Vrbka, and P. Jungwirth, Monitoring ice nucleation in pure and salty water via high speed

- imaging and computer simulations. *J. Phys. Chem. C* **112**, 7631 (2008).
- [118] E. Pluhařová, L. Vrbka, and P. Jungwirth, The effect of surface pollution on homogeneous ice nucleation: A molecular dynamics study. *J. Phys. Chem. C* **114**, 7831 (2010).
- [119] P. Pirzadeh and P. G. Kusalik, On understanding stacking fault formation in ice. *J. Am. Chem. Soc.* **133**, 704 (2010).
- [120] E. Sanz, C. Vega, J. R. Espinosa, R. Caballero-Bernal, J. L. F. Abascal and C. Valeriani, Homogeneous ice nucleation at moderate supercooling from molecular simulations. *J. Am. Chem. Soc.* **135**, 15008, (2013).
- [121] L. R. Maki, E. L. Galyan, M. M. Chang-Chien and D. R. Caldwell, Ice Nucleation Induced by *Pseudomonas syringae*. *Appl Microbiol.* **28**, 456, (1974).
- [122] H. A. Kolodziej, B. P. Jones and M. Davies, High field dielectric measurements in water. *J. Chem. Soc. Faraday Trans. II.* **71**, 269, (1975).
- [123] M. Orłowska, M. Havet, and A. Le-Bail, Controlled ice nucleation under high voltage DC electrostatic field conditions. *Food Res. Int.* **42**, 879, (2009).
- [124] J. R. Errington and P. G. Debenedetti, Relationship between

- structural order and the anomalies of liquid water. *Nature*, **409**, 318, (2001).
- [125] S. D. Overduin and G. N. Patey, Understanding the structure factor and isothermal compressibility of ambient water in terms of local structure environments. *J. Phys. Chem. B.* **116**, 12014, (2012).
- [126] D. T. Bowron, J. L. Finney, A. Hallbrucker, I. Kohl, T. Loerting, E. Mayer and A. K. Soper, The local and intermediate range structures of the five amorphous ices at 80 K and ambient pressure: a Faber-Ziman and Bhatia-Thornton analysis. *J. Chem. Phys.* **125**, 194502, (2006).
- [127] A. J. C. Ladd and L. V. Woodcock, Interfacial and co-existence properties of the Lennard-Jones system at the triple point. *Mol. Phys.* **36**, 611, (1978).
- [128] C. Vega, M. Martin-Conde, and A. Patrykiewicz, Absence of superheating for ice Ih with a free surface: A new method of determining the melting point of different water models. *Mol. Phys.* **104**, 3583 (2006).
- [129] T. L. Hill, *An Introduction to Statistical Thermodynamics*. (Addison-Wesley, London, 1962).
- [130] J. J. Salacuse, A. R. Denton, and P. A. Egelstaff, Finite-size effects in molecular dynamics simulations: Static structure factor and compressibility. I. Theoretical method. *Phys. Rev. E* **53**, 2382 (1996).
- [131] N. Hull and D. A. Keen, Pressure-induced phase transitions in AgCl, AgBr and AgI. *Phys. Rev. B*, **59(2)**, 750, (1999).

Bibliography

- [132] S. Zielke and G. N. Patey, Research of ice nucleation on AgI faces is in progress.